

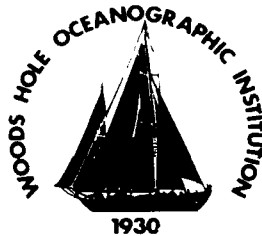
AD-A242 112



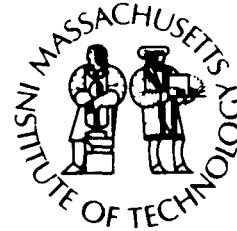
WHOI-87-23

①

# **Woods Hole Oceanographic Institution Massachusetts Institute of Technology**



**Joint Program  
in Oceanography  
and  
Oceanographic Engineering**



---

**DOCTORAL DISSERTATION**

## **Application of Seasat Altimetry to Tectonic Studies of Fracture Zones in the Southern Oceans**

by

**Mavis Lynn Driscoll**

June 1987

Approved for public release;

Distribution Unlimited

WHOI-87-23

**Application of Seasat Altimetry to Tectonic Studies  
of Fracture Zones in the Southern Oceans**

by

Mavis Lynn Driscoll

Woods Hole Oceanographic Institution  
Woods Hole, Massachusetts 02543

and

The Massachusetts Institute of Technology  
Cambridge, Massachusetts 02139

June 1987

**Doctoral Dissertation**

Funding was provided by the Office of Naval Research under contract Numbers N00014-80-C-0273, and N00014-86-K-0325, and by the National Science Foundation under grant Number DPP-8405968.

Reproduction in whole or in part is permitted for any purpose of the United States Government. This thesis should be cited as:  
Mavis Lynn Driscoll, 1987. Application of Seasat Altimetry to Tectonic Studies of Fracture Zones in the Southern Oceans.  
Ph.D. Thesis. MIT/WHOI, WHOI-87-23.

Approved for publication; distribution unlimited.

**Approved for Distribution:**

*David A. Ross*

David A. Ross, Chairman  
Department of Geology & Geophysics

*Charles D. Hollister*

Charles D. Hollister  
Dean of Graduate Studies

Accession For	
NTIS GRA&I	<input checked="" type="checkbox"/>
DTIC Tab	<input type="checkbox"/>
Document Number	<input type="checkbox"/>
Justification	
By	
Distribution/	
Availability Codes	
Dist	Avail and/or
A-1	Special

91-14714

91 10 31 086

APPLICATION OF SEASAT ALTIMETRY TO TECTONIC STUDIES  
OF FRACTURE ZONES IN THE SOUTHERN OCEANS

by

MAVIS LYNN DRISCOLL  
B.A., University of California at Berkeley, 1981

SUBMITTED IN PARTIAL FULFILLMENT OF THE  
REQUIREMENTS FOR THE DEGREE OF  
DOCTOR OF PHILOSOPHY

at the  
MASSACHUSETTS INSTITUTE OF TECHNOLOGY  
and the  
WOODS HOLE OCEANOGRAPHIC INSTITUTION

June 1987

©Massachusetts Institute of Technology, 1987

Signature of author.....*Mavis Driscoll*.....  
Joint Program in Oceanography, Massachusetts  
Institute of Technology and Woods Hole  
Oceanographic Institution, June 1987

Certified by.....*Bary Parson*.....  
Thesis Supervisor

Accepted by.....*Jim E. Turkoshvili*.....  
Chairman, Joint Committee for Marine Geology  
and Geophysics, Massachusetts Institute of  
Technology and Woods Hole Oceanographic  
Institution

APPLICATION OF SEASAT ALTIMETRY TO TECTONIC STUDIES  
OF FRACTURE ZONES IN THE SOUTHERN OCEANS

by  
MAVIS LYNN DRISCOLL

Submitted to the Joint Program in Marine Geology and Geophysics on  
May 14, 1987 in partial fulfillment of the requirements for  
the degree of Doctor of Philosophy

ABSTRACT

Gravity derived from Seasat altimetry has provided a means of estimating seafloor topography and its compensation, which in turn can be used to understand the evolution of oceanic lithosphere. In the first study, the correlation between the geoid, deflection of the vertical, and seafloor topography is investigated along a section of the Southwest Indian Ridge. Geoid anomalies computed from a simple thermal model fairly accurately predict the intermediate-wavelength anomalies across the fracture zones. The shorter wavelength anomalies are consistent with those calculated from topography using elastic plate compensation. The combined effect of the thermal offset and seafloor topography produces an anomaly which has a small-amplitude, short-wavelength depression directly over the fracture zone valley. Pronounced lineations in the horizontal geoid gradient do not coincide with the valley but have trends parallel to the fracture zones.

In the second study, fracture zones along the Southwest Indian Ridge are identified using altimeter profiles and bathymetry. Finite poles of rotation are determined from the fracture zone locations and magnetic anomaly lineations for anomalies 6 (20 Ma), 13 (37 Ma), and 20 (45 Ma). The new poles are in general agreement with previously published poles and describe a fairly consistent direction of relative motion between Africa and Antarctica for the past 45 Myr. A present-day pole of rotation calculated from transform fault azimuths determined primarily from their geoid anomalies, agrees with published poles based on bathymetric data.

In the third study, the rate of change of the geoid with age has been estimated as a function of age from geoid offsets across the Eltanin and Udintsev fracture zones and used to constrain thermal models of lithospheric cooling. Observed trends in the geoid slope versus age plots are similar on both branches of the Eltanin and the east limb of the Udintsev fracture zone. The similarity in trends argues against the effects of isolated thermal or bathymetric anomalies and appears instead to reflect a general feature of the geoid-slope versus average age relationship across fracture zones. Although the thermal plate cooling model is successful in predicting both seafloor depths and heat flow values out to ages of at least 80 m.y. B.P., it cannot explain the observed geoid slope values for these two fracture zones. It is not clear at this point whether this is due to inadequacies in the cooling model or to peculiarities in fracture zone evolution.

Thesis Supervisor: Barry Parsons  
Title: Professor of Marine Geophysics

## Table of Contents

Abstract.....	2
List of Figures.....	5
List of Tables.....	7
Chapter 1: Introduction.....	8
1.1 Overview.....	9
1.2 Seasat altimetry.....	11
1.3 The geoid.....	14
1.4 Short-wavelength geoid anomalies and fracture zones.....	15
1.5 Fracture zones and plate rotations.....	18
1.6 Cooling of the oceanic lithosphere.....	19
1.7 Co-authored chapters.....	20
1.8 References.....	22
Chapter 2: Fracture zone trends and structure at the Southwest Indian Ridge: An investigation using Seasat altimetry and surface-ship bathymetry.....	24
2.1 Abstract.....	25
2.2 Introduction.....	26
2.3 Seafloor topography.....	33
2.4 Altimetry.....	37
2.5 Bathymetry and along-track geoid.....	38
2.6 Along-track deflection of the vertical.....	41
2.7 Gridded bathymetry, geoid and deflection of the vertical.....	44
2.8 Modeling.....	54
Thermal edge effect.....	54
Plate compensation model.....	62
2.9 Discussion.....	66
2.10 Acknowledgements.....	70
2.11 Appendix.....	72
2.12 References.....	74
Chapter 3: Eocene to present-day plate motions at the Southwest Indian Ridge.....	79
3.1 Introduction.....	80
3.2 African-Antarctic plate boundary — past and present....	83
3.3 Magnetic anomalies.....	85
3.4 Fracture zones.....	85
3.5 Present-day pole of rotation.....	92
3.6 Finite poles — method.....	94
3.7 Anomaly 6.....	94
3.8 Anomaly 13.....	96
3.9 Anomaly 20.....	100
3.10 Flowlines.....	100

3.11	Discussion.....	104
	Mid-Cretaceous to Eocene plate motion.....	104
	Improvements in the parameters of plate rotation....	105
3.12	Conclusions.....	108
3.13	References.....	109
Chapter 4: Cooling of the oceanic lithosphere -- Evidence from geoid anomalies across the Udintsev and Eltanin Fracture Zones.....		
4.1	Abstract.....	117
4.2	Introduction.....	118
4.3	Udintsev and Eltanin Fracture Zones.....	123
4.4	Method.....	125
4.5	Results.....	132
4.6	Discussion.....	146
4.7	Acknowledgements.....	152
4.8	Bibliography.....	153
Chapter 5: Summary and Conclusions.....		
5.1	Correlation between seafloor topography and the geoid...	157
5.2	Plate reconstructions using Seasat altimetry.....	158
5.3	Thermal evolution of oceanic lithosphere.....	160
5.4	References.....	163
Acknowledgements.....		164
Biographical sketch.....		165

## List of Figures

### Chapter 1:

Figure 1.	Seasat altimeter measurement and corrections.....	13
Figure 2.	Geoid anomaly over fracture zones.....	17

### Chapter 2:

Figure 1.	Tectonic elements in the Southwest Indian Ocean.....	29
Figure 2a.	Seafloor topography between 21°E to 50°E, 35°S to 56°S.....	31
Figure 3.	Geoid heights along ascending satellite arcs.....	39
Figure 4.	Geoid gradients along ascending arcs.....	42
Figure 5.	Geoid anomaly map (color).....	47
Figure 6.	Deflection of the vertical map (color).....	48
Figure 7.	Bathymetry (color).....	48
Figure 8.	Profile locations for Figure 9.....	51
Figure 9.	Profiles of coincident bathymetry, geoid height and deflection of the vertical.....	52
Figure 10.	Initial temperature distribution across two fracture zones.....	56
Figure 11a.	Calculated geoid gradients across adjacent fracture zones.....	58
11b.	Plan view of geoid gradients.....	58
Figure 12.	Effects on the geoid of decreasing the distance between two fracture zones.....	60
Figure 13.	Geoid profile across DuToit, Bain and Prince Edward fracture zones calculated from thermal offset.....	61
Figure 14.	same as Figure 13 across different profile.....	63
Figure 15a.	Geoid heights calculated using elastic plate compensation across DuToit, Bain and Prince Edward fracture zones.....	65
15b.	Combined thermal and elastic plate geoid and gradient anomalies.....	65
Figure 16a.	same as for Figure 15a for profile presented in Figure 14.....	67
16b.	same as for Figure 15b for profile in Figure 14.....	67
Figure 17.	Bathymetry and geoid heights calculated using an elastic plate model for profiles across DuToit and Bain fracture zones.....	68

### Chapter 3:

Figure 1.	Locations of published instantaneous poles of rotation for Africa/Antarctica.....	82
Figure 2.	Location map.....	84
Figure 3.	Seasat track chart.....	87
Figure 4.	Ridge crest, fracture zone and magnetic anomalies...	88
Figure 5a.	Contour plot of errors for poles in the neighborhood of the best-fitting pole for anomaly 6.....	95
5b.	for anomaly 13.....	95
5c.	for anomaly 20.....	95

Figure 6.	Reconstructions of magnetic lineations and transform faults for anomalies 6, 13 and 20.....	97
Figure 7.	Intersections of predicted flowlines with altimetry profiles.....	101
Figure 8.	Intersections of predicted flowlines for anomaly 32 to anomaly 28 with altimeter profiles.....	106
Chapter 4		
Figure 1.	Location map and magnetic anomalies.....	124
Figure 2.	Selected geoid profiles across the Eltanin and Udintsev fracture zones.....	127
Figure 3.	Differences between geoid height offsets measured from profiles with and without GEM9 reference field removed.....	130
Figure 4.	Location of Seasat tracks.....	133
Figure 5a.	Geoid slope estimates across western branch of Eltanin Fracture Zone.....	136
5b.	across eastern branch.....	136
Figure 6a.	Estimated regional polynomial and offset at selected geoid profiles along the Eltanin.....	137
6b.	Geoid profiles with regional polynomial removed, and theoretical profiles for plate thicknesses of 120 km and 70 km.....	137
Figure 7a.	same as in Figure 6a using different profiles.....	139
7b.	same as in Figure 6b with plate thicknesses of 60 km and 90 km.....	139
Figure 8a.	same as in Figure 6a using different profiles.....	140
8b.	same as in Figure 6b with plate thicknesses of 55 km and 90 km.....	140
Figure 9a.	Geoid slope estimates across western branch of Udintsev Fracture Zone.....	142
9b.	across eastern branch.....	142
Figure 10a.	Geoid profiles across Udintsev Fracture Zone with GEM9 reference field removed and estimated polynomial and offsets determined using exclusion widths of 100 km and 200 km.....	144
10b.	Geoid profiles with estimated regional polynomials removed compared to theoretical profiles calculated for plate thicknesses of 60 km and 90 km.....	144
Figure 11.	Seafloor depth curves for plate thicknesses of 60 km and 90 km and empirical depth curve for the South Pacific.....	148
Figure 12a.	Geoid heights for plate thicknesses of 100 km and 120 km.....	150
12b.	Geoid slope estimates across a fracture zone assuming a 120 km thick plate on one side of the fracture zone and a 100 km thick plate on the other side.....	150



## List of Tables

Chapter 2	
Table 1.	Model parameters..... 71
Chapter 3	
Table 1.	Instantaneous poles of rotation.....111
Table 2.	Comparison between observed and predicted transform fault azimuths.....112
Table 3.	Fracture zone crossings, magnetic anomaly lineations and their uncertainties.....113
Table 4.	Finite rotation poles and stage poles.....116
Chapter 4	
Table 1.	Model parameters.....155

## Chapter 1. Introduction

## INTRODUCTION

### 1.1 Overview:

Analyses of Seasat altimeter profiles have revealed the shape of the ocean surface in considerably more detail than it was previously known. Because of their gravitational attraction, tectonic features such as fracture zones and spreading ridges distort the shape of the ocean surface and their anomalies can be easily seen in maps of the gravity field derived from the altimeter data. This new source of geophysical information can be used to identify and locate these features and to study their density structures at depth. From this we can derive information on the thermal and mechanical behaviour of oceanic lithosphere. Fracture zones in particular are well-sampled in the altimeter data and are the focus of this thesis.

Fracture zones are long, linear scars in oceanic lithosphere that are the traces of previously active transform faults. They can extend the full width of ocean basins and on slow-spreading ridges such as the Mid-Atlantic and Southwest Indian ridges, are spaced on the order of a hundred kilometers apart. The morphology of fracture zones is often extremely rugged with valleys as deep as 5000-6000 m and linear ridges (parallel to the valleys) extending to within 1000 m or less of the ocean surface. Fracture zones separate oceanic lithosphere of different ages, with the age separation dependent on the transform length and the spreading rate at the time of crustal formation. This age offset gives rise to a difference in the thermal structure of the lithosphere on either side of the fracture zone, and a corresponding difference in the rate of seafloor subsidence. The upper few kilometers of lithosphere loses heat through conduction as it moves away from the spreading ridge,

and becomes more rigid and stronger as it cools. The net effect of the cooling and subsidence is to decrease the gravitational anomaly from what it was originally at the spreading ridge. At fracture zones, the age difference is also reflected in a change in the gravitational attraction of the lithosphere across the fracture zone. This offset is readily seen in maps of the gravity field or geoid, particularly at large offset fracture zones such as those in the North and South Pacific oceans.

Transform faults form in response to motions between two plates, and when the plates are rigid, the faults follow arcs of small circles about the pole of rotation. The directions of motion determined from transform fault azimuths are very reliable and are used in determining locations of instantaneous rotation poles (e.g., Minster and Jordan, 1978). Ideally, the trends of fracture zones should record past plate motions between diverging plates, and when the transform faults are short this is generally true. Large-offset fracture zones are generally less reliable because of the possibility of deformation within the transform fault during changes in the direction of relative motion. From geometric considerations, adjustments at a large-offset transform fault may either cause a new ridge-crest segment to form, or break up an existing segment to accommodate the change in spreading direction (Menard and Atwater, 1969). To date, surveys of fracture zones have not been sufficiently detailed to document styles of deformation, and structural histories of fracture zone deformation during plate reorganizations are sketchy at best. Until more is known, fracture zone trends may not, in general, be reliable indicators of plate motions

during phases of rapid plate reorganizations but should accurately record directions of relative motion between these times.

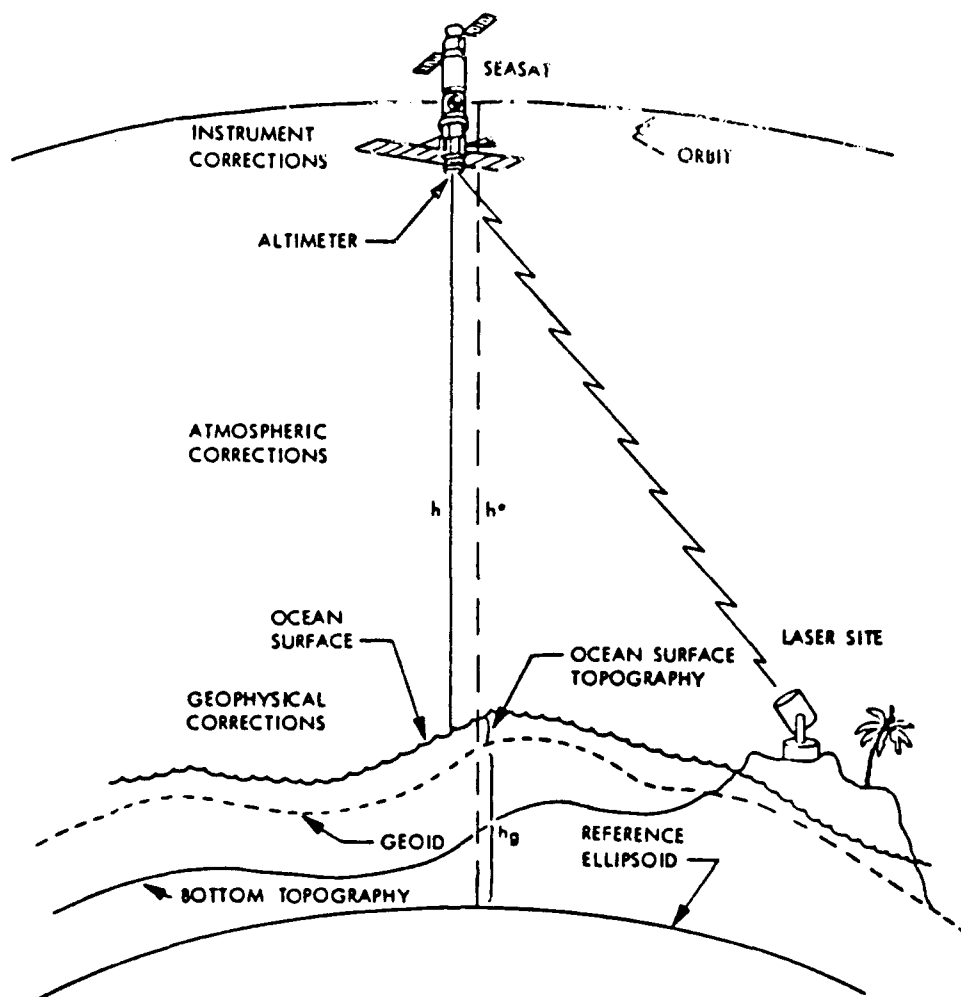
In this thesis, bathymetry and satellite altimetry are used to look at fracture zone structure and evolution in the South Pacific and Southwest Indian Oceans. Correlations between the geoid, deflection of the vertical, and seafloor topography are investigated in the first study. In the second study, fracture zone traces are used in conjunction with magnetic lineations to determine Eocene to recent plate motions at the Southwest Indian Ridge. In the final study, geoid offsets across the Udintsev and Eltanin Fracture Zones are used to constrain models of lithospheric cooling.

The use of satellite altimeter profiles in geophysical studies requires an understanding of the measurements and how they relate to the Earth's gravity field. These topics are introduced in the next two sections and are followed by a description of their use in the three studies contained within this thesis.

## 1.2 Seasat Altimetry

The Seasat satellite was launched on 28 June 1978 and operated for about three months before it failed on 10 October 1978. The radar altimeter onboard the satellite operated intermittently and collected approximately 70 days of data. These data consist of two-way travel times of a short-pulse microwave signal traveling from the satellite sensor to the ocean surface and back to the antenna. Independently, the orbit of the satellite is computed which gives the distance between the satellite and a reference ellipsoid. This distance  $h^*$  is the sum of several effects including the height of the satellite above the ocean

surface  $h$ , the geoid height  $h_g$ , solid earth and ocean tides  $h_t$ , and oceanographic effects (such as currents)  $h_o$  (Figure 1). Additionally, corrections for instrument errors  $h_i$ , and path length disturbances  $h_a$ , caused by the signal passing through changing conditions in the atmosphere are present in the measurements (see Tapley et al., 1982). The sum of the geoidal and oceanographic components can be expressed in terms of the above quantities as:  $h_g + h_o = h^* - h - h_t - h_a - h_i + e(\text{random errors})$ . Although the oceanographic effects are measurable (Zlotnicki, 1983), they have small amplitudes (less than 1 m) compared with the geoidal component of the signal (up to 100 m). The oceanographic signal is also difficult to model and for these reasons is ignored in this and most studies that are primarily concerned with the geoid. Errors in the estimation of the geoid from the altimeter measurements come from three main sources: the satellite orbit determination, estimates of the various environmental corrections, and instrument errors. Although the satellite was tracked at certain stages along its path, the orbit between tracking times has to be calculated. To do this accurately requires a knowledge of the Earth's gravity field, which is not known with enough accuracy to predict the orbit to within several meters. The errors in the orbit computation can be determined by comparing the apparent height of the satellite where two tracks cross. This cross-over error is frequently several meters but can be reduced in particular geographic areas to only several tens of centimeters or less by doing a least-squares adjustment of orbit heights at cross-over points (e.g. Rapp, 1982; Freedman and Parsons, 1986). Instrument errors are less than 10 cm and errors in the various corrections are 3 cm or less (Tapley et al., 1982).



$$h^* = h + h_g + h_t + h_0 + h_i + h_a + e$$

ORBITAL ERROR	1.5 m
AFTER CROSS-OVER CORRECTIONS	10-30 cm
HEIGHT TO SEA SURFACE	<10 cm

Figure 1. Seasat altimeter measurement and corrections.  
(modified from Tapley et al., 1982)

An additional measurement of the accuracy of the altimeter data is its resolution of features at different wavelengths. This can be determined by analyzing the coherence between repeat tracks and has been found to be fairly high for features with wavelengths down to 30 km (Brammer and Sailor, 1980). This is the smallest wavelength which is repeatable although smaller wavelengths in the profiles may, in fact, be real features.

### 1.3 The Geoid

The altimeter profiles provide measurements of the geoid, which is an equipotential surface of the Earth's gravity field. The geoid is defined to be that surface which is closely approximated by the ocean surface in the absence of tides and other phenomena causing departures from equilibrium. Geoid undulations are measured relative to a reference surface, generally a reference ellipsoid of revolution. These undulations are produced by density anomalies in the Earth's crust, mantle or core and can be used to constrain geophysical models of mantle convection, topography on the core-mantle boundary, and the compensation of tectonic features.

The density structure of a tectonic feature cannot be determined uniquely from its geoid anomaly. Additional geophysical information such as seafloor topography, seismic velocity structure, knowledge of the strength of the crust from laboratory studies, or limits on the temperature structure at depth from surface heat-flow studies help to limit the number of possible density models. The strength of a potential field is inversely proportional to the distance from its source and this characteristic of the gravity field often helps to limit possible models. For example, short-wavelength anomalies from a feature



on the core-mantle boundary will be severely attenuated at the surface of the Earth and will be below the precision of our measurements. It can generally be inferred that the shortest wavelengths in the geoid (less than several hundred kilometers) arise from density anomalies in the crust and upper mantle. It is not true, however, that sources for longer-wavelength anomalies must be deep because very shallow, broad features on the seafloor will also create long-wavelength anomalies.

#### 1.4 Short-wavelength geoid anomalies and fracture zones

In the first research study of this thesis (Chapter 2), altimeter profiles are compared to seafloor topography in order to characterize the shape of fracture zone anomalies at the slow-spreading Southwest Indian Ridge. The thermal and mechanical behaviours of the oceanic lithosphere is modeled to examine their relative contributions to the observed gravity anomalies. The Southwest Indian Ridge is chosen as the area of study for several reasons. Along this ridge fracture zones are closely-spaced, and have very high topographic relief. Previous to this study, it was not known whether the thermal offsets that show up so clearly at the Mendocino Fracture Zone in the North Pacific (e.g. Crough, 1979) were identifiable at fracture zones along such a slow-spreading ridge. Additionally, a good knowledge of bathymetry is necessary and the area between 22 and 60° E has sufficiently detailed bathymetric coverage to make this study possible. Also, once the characteristics of the fracture zone anomaly are determined, this information can be used to delineate fracture zones and study the kinematic history of African-Antarctic plate motions.

The geoid anomaly at a fracture zone is the combined effect of the gravitational attraction of seafloor topography and the attraction due to the thermal offset. This has been modeled at the Mendocino Fracture Zone using density models consistent with the age of the seafloor and presumed temperature of the lithosphere (Crough, 1979; Detrick, 1981; Sandwell and Schubert, 1982) and at fracture zones in the Pacific (Cazenave 1984a, 1984b). The geoid anomaly has a step-like shape with the higher side of the step over the younger, hotter and more shallow seafloor (Figure 2). In these studies, the effect of topography other than that due to seafloor subsidence is not considered because the signal of interest (the geoid step) has a wavelength greater than 100 km and the contributions from seafloor topography are expected to have shorter wavelengths. In this study, however, the observed geoid anomalies along fracture zones on the Southwest Indian Ridge deviate substantially from a simple step model, a result which indicates that the gravitational effect of seafloor topography at the fracture zone is an important contribution. Another complication is the closeness of adjacent fracture zones. Because of their proximity, the geoid anomalies from adjacent fracture zones are superimposed. In Chapter 2, we find that the combined contributions from seafloor topography and thermal offsets produce a characteristic anomaly composed of a small-amplitude trough, 20-50 km wide and 0.5 m deep, superimposed on an intermediate-wavelength geoid offset. The trough is produced by the mass deficit at the fracture zone valley and is situated directly above the valley, so that the anomaly can be used to delineate fracture zones along this spreading ridge. The intermediate-wavelength anomaly is antisymmetric about the fracture zone valley and appears to be

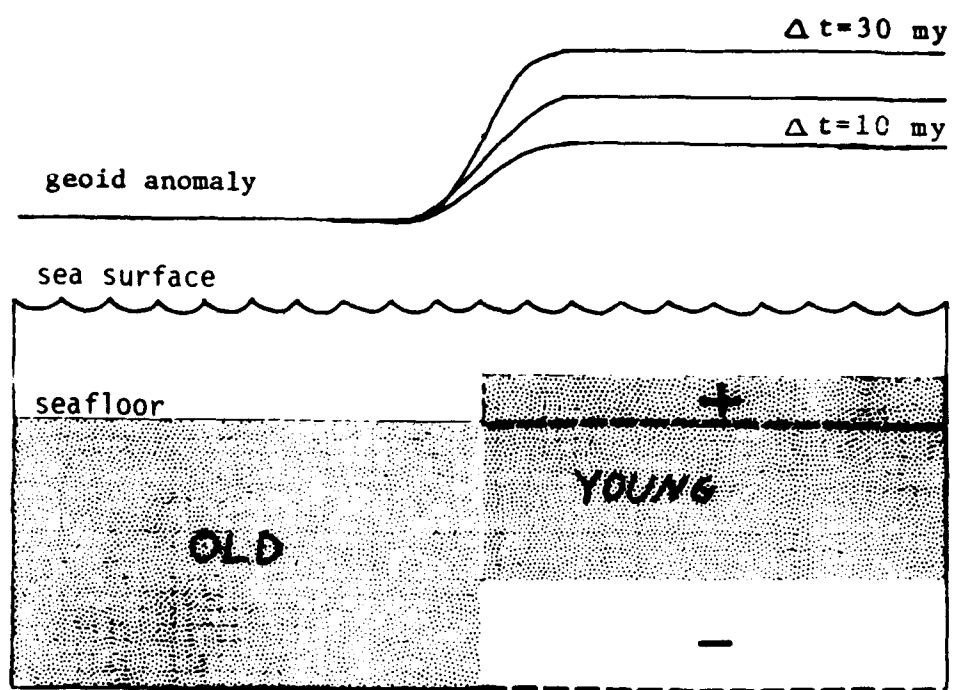


Figure 2. Geoid anomalies over fracture zones.

consistent with geoid height versus age relationships although this cannot be rigorously proved because the age of the seafloor is not known well enough.

#### 1.5 Fracture zones and plate rotations

In Chapter 3, fracture zone lineations determined from altimeter profiles and bathymetry are used along with magnetic anomaly lineations to determine rotation parameters for African-Antarctic plate motions for the present-day and at the times of magnetic anomalies 6, 13 and 20. The addition of a large quantity of fracture zone locations to estimate past plate boundaries introduces two major assumptions into the finite rotation pole determinations. One is that fracture zones reliably record the relative plate motions between diverging plates. The other is that there have not been ridge jumps at any of the fracture zones used to determine the past plate boundary. Although we do not have sufficient information for this ridge on actual fracture zone deformation in order to eliminate those trends which may be unreliable, the lineations used are judged to be reliable for two reasons. The first is that, based on earlier plate motion studies, the pole describing African-Antarctic plate motion has remained fairly stable from at least anomaly 24 to the present (Fisher and Sclater, 1983), and thus, significant deformation has not been necessary to accommodate changes in spreading direction. The second reason is that the poles that we determine using both magnetic anomaly lineations and fracture zones do a good job in reconstructing both types of lineations. This would not be the case if differential amounts of deformation had occurred at the fracture zones.

## 1.6 Cooling of the oceanic lithosphere

The intermediate-wavelength geoid anomaly (100-800 km) is examined at the Udintsev and Eltanin Fracture Zones along the fast-spreading Pacific/Antarctic Ridge (6 cm/yr) in Chapter 4 in order to determine a geoid height versus age relationship. Geoid heights are sensitive to the density structure of the lithosphere, and thus to its temperature through the relationship between temperature and the density of materials. The height of the geoid is more sensitive than the subsidence of the seafloor to deeper temperature variations in the lithosphere. This allows differences between proposed cooling models for oceanic lithosphere to show up at earlier ages in geoid measurements compared with the traditionally used seafloor depths. Although geoid heights relative to ridge crests have been used to derive a geoid height-age relationship analogous to the depth relation (Sandwell and Schubert, 1980), this method is not used here in preference to using geoid offsets at fracture zones. This is done in order to minimize problems caused by geoid variations which are related to mantle structure and that are present in the geoid at the same wavelengths as the geoid variations caused by conductive cooling in the lithosphere.

In Chapter 4, we find that the measurement of the offset is not trivial and is affected by short-wavelength anomalies near the fracture zone and on seafloor between fracture zones (such as small seamounts). The source of the anomalies near the fracture zone have been modeled both as flexural effects due to differential subsidence across the fixed fracture zone boundary (Sandwell, 1984) and as bending of the lithosphere during its passage through the transform domain where free slip can occur across the fault (Parmentier and Haxby, 1986). In our

study the effects of these anomalies are minimized in order to get an accurate measurement of the geoid offset. Earlier studies of geoid heights at these fracture zones (Cazenave 1984a, 1984b) did not use all available altimeter profiles, most likely because of the presence of these anomalies, and presented their results from all fracture zones together. In our study more altimeter profiles can be used because of a modification in the way the geoid offset is measured which allows certain parts of the profiles to be excluded. Also, geoid variations across each branch of the two fracture zones are examined separately in order to identify variations which may be local and not representative of the average geoid height-age relationship. The resulting relationship is found to be more complicated than predicted by either a half-space or plate cooling model for seafloor older than 30 Myr. The relationship approaches a constant value on older seafloor which is predicted by the plate model (and not by the half-space cooling model) but the variation is not smooth and monotonic. Existing models do not match the observations and indicate the need for more accurate models for the cooling of the oceanic lithosphere.

#### 1.7 Co-authored Chapters

Chapter 2 is in review with the Geophysical Journal of the Royal Astronomical Society. I am the principal author, while R.L. Fisher and B. Parsons are second and third authors, respectively. R. L. Fisher compiled and contoured the data for the bathymetric chart in Figure 2-2. He also wrote section 2-3 on seafloor topography and extensively reviewed the remaining parts of the chapter which were written by

myself. B. Parsons suggested the research, provided guidance throughout the project, and reviewed the paper.

Chapter 4 is in review with Earth and Planetary Science Letters. I am principal author, and B. Parsons is co-author. The research was suggested and guided by B. Parsons, who also reviewed the manuscript. All of the research and writing was mine.

## 1.8 References

- Brammer, R.F. and R.V. Sailor, 1980, Preliminary estimates of the resolution capability of the Seasat radar altimeter, *Geophys. Res. Lett.*, 7, 193-196.
- Cazenave, A., 1984a, Two distinct trends for cooling of the oceanic lithosphere, *Nature*, 310, 401-403.
- Cazenave, A., 1984b, Thermal cooling of the oceanic lithosphere: New constraints from geoid height data, *Earth Planet. Sci. Lett.*, 70, 395-406.
- Crough, S.T., 1979, Geoid anomalies across fracture zones and the thickness of the lithosphere, *Earth Planet. Sci. Lett.*, 44, 224-230.
- Detrick, R.S., 1981, An analysis of geoid anomalies across the Mendocino fracture zone: Implications for thermal models of the lithosphere, *J. Geophys. Res.*, 86, 11751-11762.
- Fisher, R.L., and J.G. Sclater, 1983, Tectonic evolution of the Southwest Indian Ridge since the Mid-Cretaceous: Plate motions and stability of the pole of Antarctica/Africa for at least 80 Myr, *Geophys. J. Royal astr. Soc.*, 73, 553-576.
- Freedman, A.P. and B. Parsons, 1986, Seasat-derived gravity over the Musicians Seamounts, *J. Geophys. Res.*, 91, 8325-8340.
- Menard, H.W. and T. Atwater, 1969, Origin of fracture zone topography, *Nature*, 222, 1037-1040.
- Minster, J. B., and T. H. Jordan, 1978, Present-day plate motions, *J. Geophys. Res.*, 83, 5331-5354.
- Parmentier, E.M. and W.F. Haxby, 1986, Thermal stresses in the oceanic lithosphere: Evidence from geoid anomalies at fracture zones, *J. Geophys. Res.*, 91, 7193-7204.
- Rapp, R.H., 1982, A summary of the results from the OSU analysis of Seasat altimeter data, Report #335 of Dept. of Geodetic Science and Surveying, Ohio State University.



- Sandwell, D.T., 1984, Thermomechanical evolution of oceanic fracture zones, J. Geophys. Res., 89, 11401-11413.
- Sandwell, D.T. and G. Schubert, 1980, Geoid height versus age for symmetric spreading ridges, J. Geophys. Res., 85, 7235-7241.
- Sandwell, D.T. and G. Schubert, 1982, Geoid height-age relation from Seasat altimeter profiles across the Mendocino fracture zone, J. Geophys. Res., 3949-3958.
- Tapley, B.D., G.H. Born and M.E. Parke, 1982, The Seasat altimeter data and its accuracy assessment, J. Geophys. Res., 87, 3179-3188.
- Zlotnicki, V., 1983, The oceanographic and geoidal components of sea surface topography, Doctoral dissertation, Massachusetts Institute of Technology.

Chapter 2. Fracture zone trends and structure at the Southwest  
Indian Ridge: An investigation using Seasat altimetry  
and surface-ship bathymetry

## Abstract

Gravity field information derived from Seasat altimetry has provided a means of estimating seafloor topography and with it, the opportunity to narrow gaps in our understanding of the evolution of remote oceanic regions. To test the accuracy of using sea-surface heights to identify and delineate tectonic elements on oceanic crust formed at a slow spreading ridge, we compared sea-surface heights and deflection of the vertical anomalies with recently compiled bathymetry over a section of the Southwest Indian Ridge between 20°E and 50°E and from 35°S to 56°S, a sector where ship-track coverage is better than in many areas of the southern oceans. From west to east the ridge is segmented by five recognized fracture zones or cross-fracture complexes marking left-lateral offsets; DuToit, the poorly-delineated Bain complex, the dual-member Prince Edward and Discovery II complexes, and the Indomed Fracture Zone, which, like DuToit is a single pronounced deep offsetting well-defined ridge crest segments. In the case of simple fractures like DuToit and Indomed, the expected step in the geoid and local maxima or minima in geoid gradients occur close to the deep fracture zone axis but are not centered on the axis. For the Bain/Prince Edward complexes of closely spaced offsets not all the individual faults are clearly defined in the deflection of the vertical, and the lineations that are observed do not generally coincide with the topographic deep marking the fracture zone. Where lineated trends in deflection of the vertical are clearly recognizable their azimuths are nearly identical to those determined from the seafloor topography.

The geoid anomaly calculated from a simple thermal model describing the cooling across fracture zones fairly accurately predicts the intermediate-wavelength geoid anomalies across the fracture zones although

the geoid offset is generally not centered on the deep fracture zone axis but is skewed towards the younger seafloor. Over most of the fracture zones there are shorter-wavelength depressions in the geoid which are not predicted by the thermal model and the observed geoid gradient is much rougher than the gradient calculated from the thermal model. The effect of topography on the shorter-wavelength geoid anomaly is investigated using an elastic-plate model; this procedure shows that the geoid and geoid gradient are significantly affected by fracture zone topography. These models indicate that the lineations seen in the geoid gradient should follow the fracture zone trends although the actual location of the deep fracture zone axis may be difficult to determine from the geoid data alone, particularly where the fracture zones are closely spaced.

#### Introduction

One of the major accomplishments of the Seasat mission (Born et al., 1979) was the collection of a large quantity of high-quality sea-surface height measurements. The sea surface is a close approximation to the marine geoid and contains information on the density distribution in the underlying crust and mantle. The largest density contrast occurs at the seafloor-water interface; deeper contrasts are caused by the decrease in rock density with increasing temperature, and by changes in composition. Recent studies (Dixon et al., 1983; Haxby et al., 1983; Sandwell, 1984c; Vogt et al., 1984; Watts et al., 1985) have shown that short-wavelength ( $\lambda < 400$  km) seafloor topography and geoid heights are highly correlated. In many areas of the oceans the Seasat-derived geoid maps have been used to identify tectonic features (Lambeck and Coleman, 1982; Lazarewicz and Schwank, 1982; Sailor and Okal, 1983; Dixon and Parke, 1983; Sandwell, 1984b). These studies show that a promising application of the altimeter

measurements is the investigation of previously unexplored ocean floor. Because of physical and economic limitations, very little of the Southern Ocean has been traversed by research vessels and the additional coverage provided by the Seasat altimeter in these regions is substantial. However, the data spacing along subsatellite track lines, and the spacing between track lines will determine the usefulness of altimeter data in any particular geophysical problem.

The interpretation of geoid heights depends on the relationship between the gravitational potential and density distributions. This relationship is nonunique, rendering it impossible to conclusively determine seafloor topography or density structure from an analysis of geoid data alone. However, properties of the potential field and our present understanding of the evolution of the seafloor provide constraints on interpretations of geoid anomalies. One such constraint is that short-wavelength variations in the geoid observed at the sea surface must be caused by shallow sources because those due to deep sources will be severely attenuated. Removing the long-wavelength components of the geoid ( $\lambda > 4000$  km) enhances signals arising from shallow mantle structure, in particular those with sources in the crust and thermally-defined plate. It is useful to develop simple models of the density structure that depend on relatively few parameters in order to identify and evaluate factors diagnostic or indicative of the evolution of the ocean floor. These can be tested in well-explored areas of the oceans where the geoid anomaly is best-defined and can then be used as guides to interpreting geoid anomalies in unexplored areas of the oceans.

Vogt et al. (1984) compared geoid heights, geoid gradients and gravity (computed from the geoid) with bathymetry and gravity collected along

9300 km of ship lines that were run coincident with 3 Seasat tracks in the North Atlantic. The geoid data were analyzed with high, low and bandpass filters to isolate particular wavelength bands. At intermediate wavelengths ( $\lambda = 300\text{--}3000$  km) fracture zones were correlated with steps in the geoid, as predicted by theoretical cooling models. At shorter wavelengths ( $\lambda = 40\text{--}300$  km) most fracture zones were associated with lows of 5–10 cm in the geoid. The conclusion drawn from the shorter wavelength signal was that local fracture zone topography significantly affects the shape of the geoid. Using spectral techniques to study topographic and gravity profiles across the Kane Fracture Zone, Louden and Forsyth (1982) also came to the conclusion that the gravitational edge effect was significant only at the longest wavelengths in their profiles ( $\lambda > 100$  km). The shorter wavelength gravity anomalies were best explained by compensation of the fracture zone topography by flexure of a thin elastic plate (6 km average thickness). Employing techniques similar to those of Vogt et al. (1984), Watts et al. (1985) compared an altimetry profile with a corresponding 1500 km-long bathymetric profile across the crest of the Southwest Indian Ridge near  $31^\circ\text{S}$  and confirmed the findings of these two sets of investigators.

In this study we compare bathymetry and geoid heights over a sector of the Southwest Indian Ocean between  $20\text{--}50^\circ\text{E}$  and  $35\text{--}56^\circ\text{S}$  (Figure 1) in order to determine the feasibility of using geoid anomalies to locate fracture zone traces formed at a slow-spreading ridge and to identify possible sources compatible with the observed geoid signal. The Southwest Indian Ridge trends diagonally across the area from the southwest to the northeast, and separates the African and Antarctic plates. The spreading rate is about 0.8 cm/yr and seafloor topography is extremely rough (Fisher

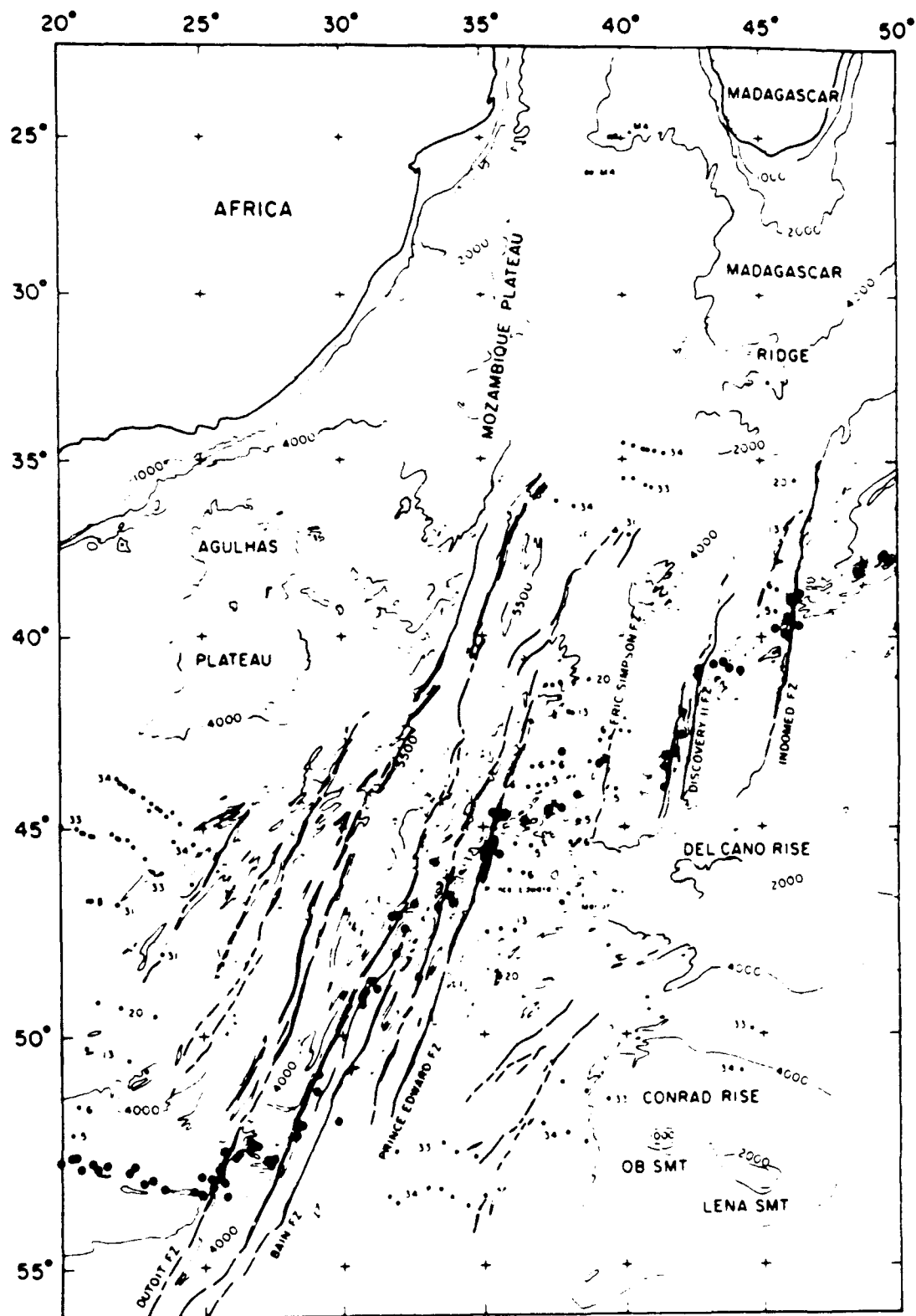


Figure 1. Tectonic elements including major fracture zones. Earthquake epicenters are marked by crossed circles and magnetic anomalies by solid circles.

and Sclater, 1983). The bathymetric chart presented here (Figure 2) includes all available data up to 1984 and new data collected in the vicinity of the westernmost fracture zones. This map is significantly more detailed than previous maps (Hayes and Vogel, 1981).

A study by Fisher and Sclater (1983) and a complementary one by Sclater et al. (1981) have investigated the tectonic development along the Southwest Indian Ridge east of  $35^{\circ}\text{E}$  and for several hundred kilometers to the north and south of the ridge crest. However, the area south of the ridge crest to the west of  $35^{\circ}\text{E}$  has not yet been closely surveyed. This has delayed improvements in the computation of the African-Antarctic pole of rotation and, consequently, the resolution of the positions of the continents within Gondwanaland.

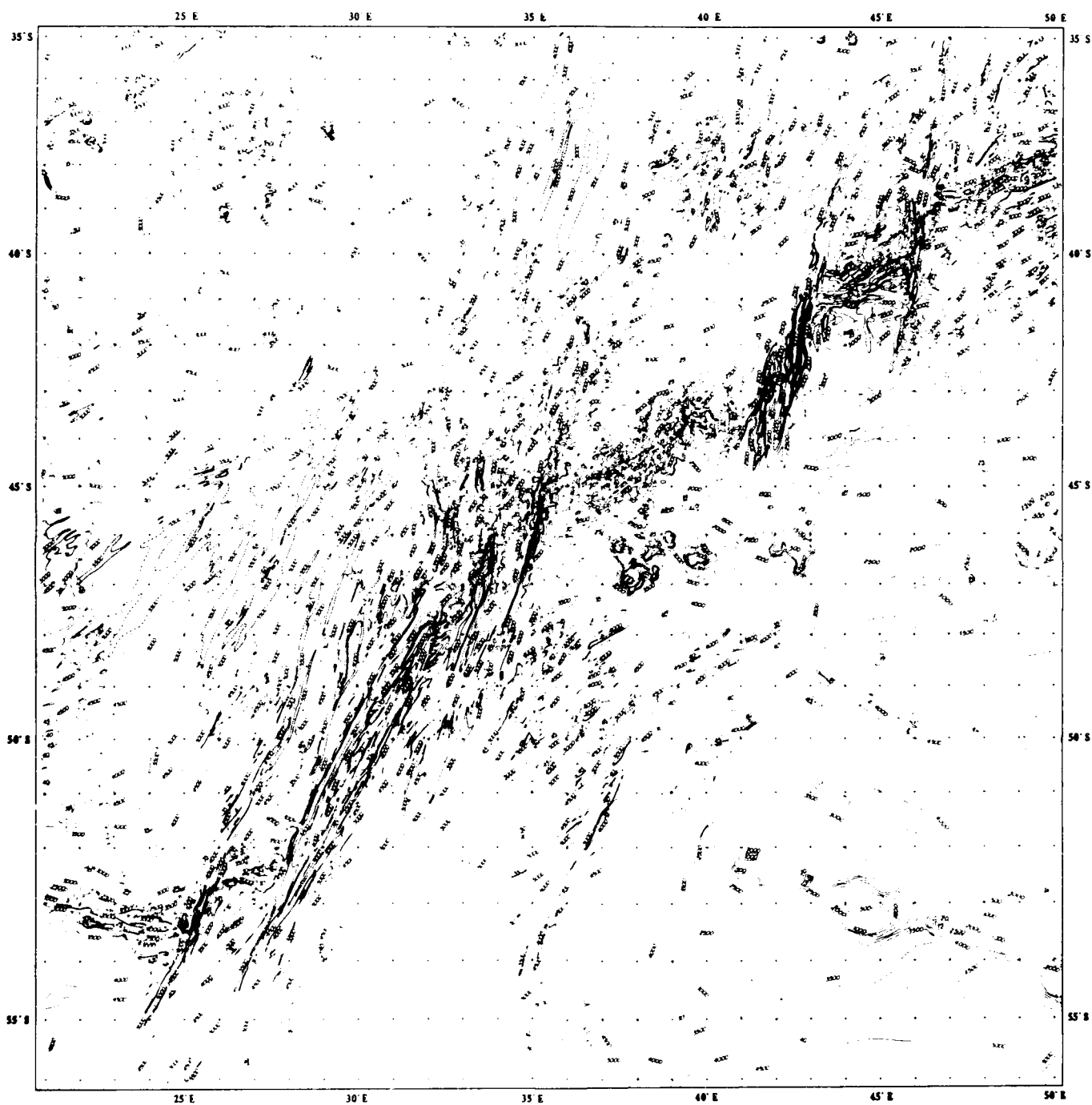
In the first section we compare large scale topographic features in the study area with geoid heights and geoid gradients that have been plotted perpendicular to subsatellite track lines. The data have been processed only minimally in order to ensure that few artifacts are introduced. In order to utilize the entire data set, color images of gridded geoid, bathymetry and deflection of the vertical (geoid gradient) are presented next and profiles calculated from the gridded data are used to support observations drawn from the along-track data.

In the second section, the geoid anomaly arising from the thermal structure associated with two closely-spaced fracture zones is calculated (Dorman, 1975; Loudon and Forsyth, 1976; Detrick, 1981). Additionally, the effect of topography at the fracture zone (the deep valley and ridges) on the geoid is examined using an elastic-plate compensation model.

Results from this study show that: 1) Geoid heights can be used to follow fracture zones a limited distance from the spreading ridge. In this



Figure 2. Seafloor topography of the Southwest Indian Ocean, 21°E to 50°E and 35°S to 56°S. Contour interval: 500 meters. Locally, multiply contour designation by 100.



ocean basin the geoid signal from fracture zones is rarely discernable over crust older than about 60 m.y. The lateral extent to which fracture zones can be traced depends primarily on the magnitude of the fracture zone offset. 2) The geoid anomaly over fracture zones is significantly affected by both the thermal contrast and local topography. The effect of the topography can be seen in the variations in geoid heights and geoid gradients. As a result, although thermal models predict a peak in the geoid gradient directly above the fracture zone, the deep bathymetric axis often lies tens of kilometers from the gradient peak. The bathymetric axis generally lies beneath a slight depression in the geoid and the trend of these anomalies gives a true indication of the fracture zone azimuths.

#### Seafloor Topography

PROTEA Expedition (September 1983 -May 1984) aboard the Scripps Institution of Oceanography R/V Melville spent 31 days exploring and sampling the Southwest Indian Ridge and environs from 54°S, 24°E to slightly east of Indomed Fracture Zone at 37°S, 48°E (Figure 1). It delineated several fracture zones and the intervening ridge crest segments but in part of the region the ridge crest is poorly developed and obscure or ambiguous on magnetic or topographic evidence (Figure 2). In particular the splayed-out complex of linear ridges-and-deeps that mark the displacement of the Southwest Indian Ridge for more than 800 km to the NNE, from near 53°S, 28°E to 47°S, 32°30'E as attested principally by shallow-focus earthquake activity, had not been suitably mapped. The group overall has been given the name Bain Fracture Zone and will be referred to as such here.

The westernmost transform fault, DuToit Fracture Zone, intersects the ridge crest at 53°30'S, 25°E; the crest is displaced about 130 km to the

north-northeast. Both ridge crest segments are well-developed, trending N100°E with median valleys at depths of 3500-4000 m. As noted by Fisher and Sclater (1983), the DuToit Fracture Zone apparently bears an en echelon relation to the poorly-developed "Mozambique Fracture Zone" which is located 120-150 km west of DuToit but does not, on topographic evidence, intersect the Southwest Indian Ridge or disrupt the seismicity pattern.

The westernmost and best developed member of the Bain Fracture Zone complex intersects the discrete southern ridge crest segment at 52°50'S, 27°30'E. The corresponding northern ridge-transform intersection is obscure on bathymetric grounds but appears from seismicity to lie 400 km northeast, near 49°S, 31°E. This member's inactive trace can be followed north-northeast to 36°S, 36°30'E; southwest of the southern intersection exploration is insufficient, and perhaps sedimentation too intense, to follow it beyond 56°S. Two more-or-less parallel members, well-developed and locally deep in the south, lie just to the east; coalescing, they terminate abruptly at 47°45'S, 32°E, south of an expected ridge crest, where from a general depth of 5000-5500 m the fracture zone axis encounters a north-northeast-trending ridge with shoal depths of less than 1500 m.

At about 45°S, 35°30'E (Figure 2) the ridge crest clearly intersects the throughgoing Prince Edward Fracture Zone first recognized by Heezen and Tharp (1965) and delineated by Bergh and Norton (1976). Southwest of this juncture is the dual or paired Prince Edward system with no well-developed magnetic pattern on the intervening spine. Total crestal offset along the paired fracture zones is 200-225 km.

East to east-northeast of the ridge crest-Prince Edward Fracture Zone intersection the magnetically well-defined ridge crest undergoes minor offsets, most markedly at a distinct -- if shallow -- topographically short

cross- fracture near 44°S, 39°15'E that parallels the major cross-cutting features and where the ridge crest is offset left-laterally by about 70-80 km. This segment of the Southwest Indian Ridge has been explored most thoroughly by South African ships; the small but discrete cross-fracture now formally bears the name 'Eric Simpson Fracture Zone' after the late University of Cape Town geologist. Near 43°30'S, 41°E the ridge crest intersects another dual system, Discovery II, that is comparable in relief, linearity, and lip development -- but with greater total crestal offset, if shorter apparent length -- to the Prince Edward pair.

The single and long, very linear Indomed Fracture Zone intersects the well-developed ridge crest near 46°E and marks a left-lateral crestal offset of nearly 200 km. In simplicity, scale and development of very shoal upfaulted local elevations, this easternmost fracture zone examined on PROTEA most resembles the westernmost, DuToit Fracture Zone far to the southwest. East of Indomed Fracture Zone the ridge crest remains fairly distinct, with only minor offsets until encountering the major multi-member Gallieni Fracture Zone Complex at 52°E (Fisher and Sclater, 1983; Figure 2b).

Several plateaus or aseismic ridges, small islands and large seamounts add to the complexity of the Southwest Indian Ocean (Figure 1). The Agulhas Plateau centered near 39°S, 26°E is underlain by oceanic crust in the north, fragments of basalt-intruded continental crust in the south (Barrett, 1977; Tucholke et al., 1981); plate reconstructions place its southern part adjacent to the southern edge of the Falkland Plateau during Neocomian times (Rabinowitz and LaBrecque, 1979). Well south of the seismically-active Southwest Indian Ridge, at latitudes 44°S to 47°S, is a

discontinuous but juxtaposed shoal complex that extends from the small volcanic islands of Marion and Prince Edward east to the broad foundation of the Crozet Archipelago east of 50°E. In the west it is represented by a cluster of seamounts or shoals and the two islands that are young, of Pleistocene to Recent age (Verwoerd, 1971). This group is separated by deep water from an extensive, aseismic, intermediate- depth plateau of oceanic composition, Del Cano Rise. This rise was created at the ridge crest and prior to 35 Ma was joined to the southern part of the Madagascar Ridge (Goslin et al., 1981; Fisher and Sclater, 1983). The similarly-shoal foundation of the Crozet Plateau, also separated from Del Cano Rise by deep water, could be of similar age but the rocks of the small islands atop it, at least, are much younger (Girod and Nougier, 1971).

In the southeast quadrant of the study area (Figure 1) are the huge Ob, Lena and Marion Dufresne seamounts lying between the Crozet and Enderby basins. From geophysical observations -- magnetics and gravity -- and calculations these massive elevations consist of oceanic rocks mantled by sediment. A summary of Institut Physique du Globe work by Goslin, Patriat and Schlich contained in Goslin (1981) suggests that this chain, trending west-northwest, was produced during an interval of abnormal volcanism at a spreading center then separating the Antarctic and Indian plates. About Anomaly 33 time this "proto-Southeast Indian Ridge" spreading center jumped northward and since that time has lain between the Crozet and Central Indian basins. On this model the seamount group marks the boundary between Anomaly 33 (toward Anomaly 1 on the north) and M0 (toward Anomaly 33 on the south).

## Altimetry

The sea surface height measurements used here were collected by the radar altimeter aboard the Seasat satellite (Born et al., 1979). The satellite flew at an altitude of 800 km with an inclination angle of  $108^\circ$  resulting in an orbital coverage densest towards the poles. Subsatellite track spacing is irregular with gaps of up to 100 km between tracks. The edited data set used in this study was provided by R. Rapp from Ohio State University and has been corrected at OSU for tidal variations, atmospheric effects, orbit errors (using a crossover minimization technique: Rapp, 1982), and spurious data points. Crossover errors in the Indian Ocean region were reduced from the original  $\pm 1.61$  m to  $\pm .25$  m. To reduce this further, the crossover errors in our study region were computed and minimized using a least-squares procedure (Freedman and Parsons, 1986). This local correction reduced the crossover error to  $\pm .16$  m. In this study we have given these data as little additional processing as possible in order to reduce the possibility of introducing artifacts into the data. Long-wavelength anomalies were removed by subtracting a GEM9 reference field from the data points along the track lines. The reference field used here was of degree and order 10 which effectively removes wavelengths greater than 4000 km. Geoid gradients along track lines were obtained by calculating the slope between adjacent data points. The long-wavelength variation in geoid heights introduces a slowly varying bias into the deflection of the vertical and causes the anomalies to have a locally non-zero mean value. To facilitate recognition of the gradient anomalies the profiles were filtered with a bandpass filter which suppressed wavelengths less than 10 km and greater than 200 km.

### Bathymetry and Along-Track Geoid:

Geoid heights are plotted perpendicular to track lines with positive values to the east (Figure 3 ) in order to compare them with the bathymetry. Only the ascending tracks are analyzed because they are almost perpendicular to the fracture zones, whereas the descending tracks are more closely parallel to them. On comparison of the geoid (Figure 3) and bathymetry (Figure 2), the largest geoid anomalies (+7 m) are seen to occur over the spreading ridge and over Conrad Rise in the southeast corner of the chart. The geoid anomaly across the spreading ridge is a function of the age of the lithosphere and decreases at a rate of approximately 0.16 m/my from its maximum height over new oceanic crust (Haxby and Turcotte, 1978) out to ages around 40-80 my. At greater ages the rate decreases (Sandwell and Schubert, 1980; Parsons and Richter, 1980). The geoid profiles across the spreading ridge east of Indomed Fracture Zone show clearly a linear decrease and also a depression in the profile above the median valley. The seamounts near Del Cano Rise and Conrad Rise represent excess mass above the surrounding seafloor and produce geoid anomalies whose heights are proportional to their depths of compensation (e.g. Watts, 1979; Freedman and Parsons, 1986). Seafloor of different ages is juxtaposed at a fracture zone and because of the relationship between geoid height and age, the geoid anomaly varies in a step-like fashion across the fracture zone (Louden and Forsyth, 1976). The largest age and geoid offsets in this area occur at the Bain Fracture Zone. South of the southern ridge segment, the geoid anomaly across the westernmost member is higher on the younger, western side with a steep, 4 m offset towards older seafloor on the east. The base of the geoid step which is marked by a slight depression, is located above the deepest part of the fracture zone.



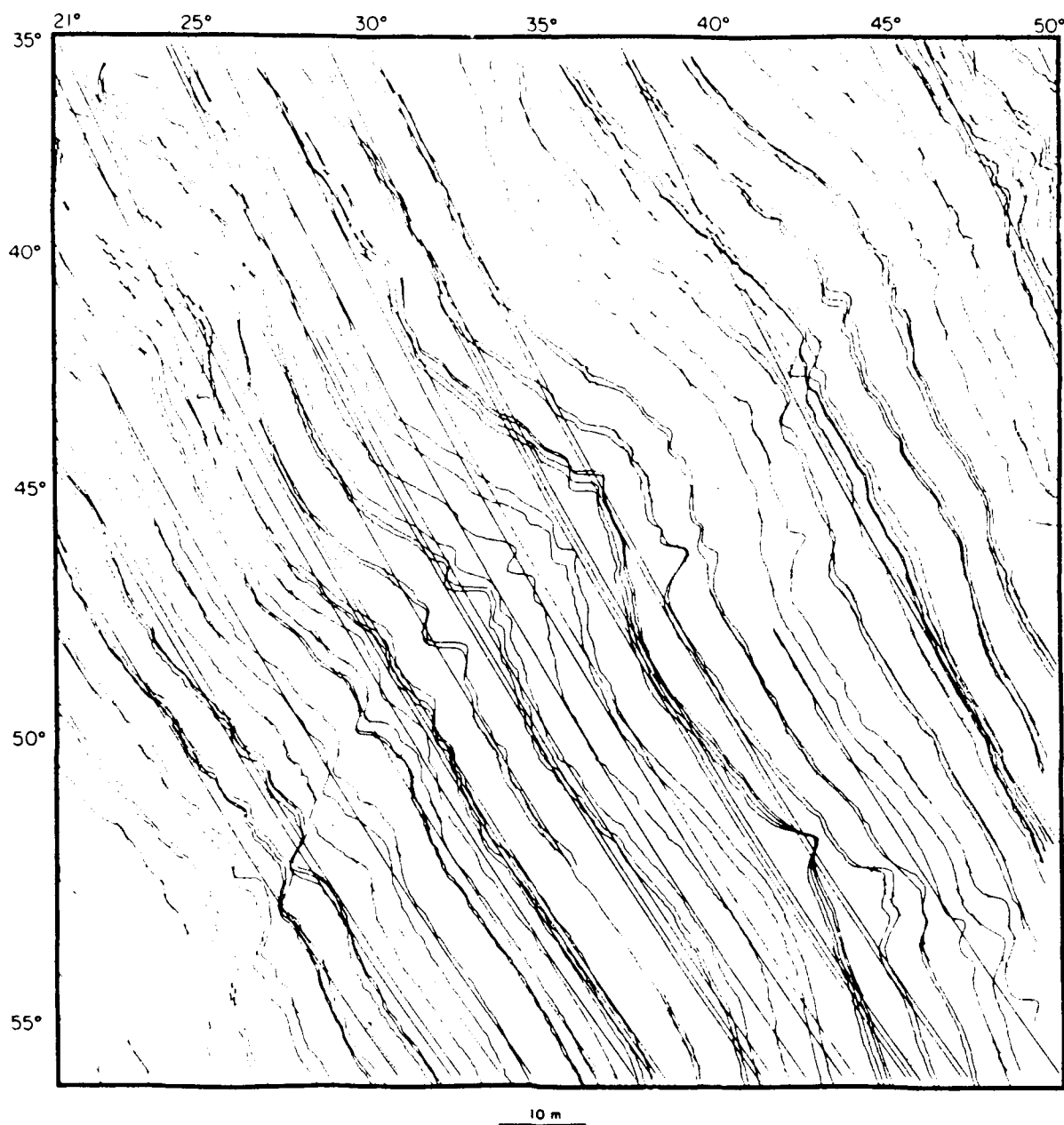


Figure 3. Geoid heights along ascending arcs of the satellite plotted perpendicular to subsatellite track lines. A reference geoid calculated using the GEM9 potential coefficients up to degree and order 10 has been subtracted from the data values. The data values have been smoothed slightly using a Gaussian-shaped filter of the form  $e^{-r^2/\sigma^2}$  where  $\sigma = 5$  km. Dashed lines mark the position of the 0 m level for the plotted anomalies and also mark the satellite path.

To the north, around  $44^{\circ}\text{S}$  on the inactive, African plate section of Bain the geoid offset is difficult to distinguish although the geoid anomaly on the western, older side is lower than on the eastern side and a slight depression marks the position of the fracture zone axis. If we ignore any contortions of the geoid anomaly other than the offsets across the western, main member of Bain and the western member of Prince Edward Fracture Zone, the geoid heights between the southern ridge-transform intersection with Bain near  $52^{\circ}50'\text{S}$ ,  $27^{\circ}30'\text{E}$  and the southern ridge-transform intersection with the western Prince Edward Fracture Zone near  $47^{\circ}\text{S}$ ,  $33^{\circ}\text{E}$ , are roughly consistent with the geoid height-age relationship. From the southern extreme of this section north to  $\sim 50^{\circ}30'\text{S}$ ,  $29^{\circ}\text{E}$  there is a clear step in the geoid across Bain with higher geoid values over the younger seafloor to the west. The depression in the geoid at the base of the step lies directly above the axis of the western member of Bain. Profiles north of this and up to  $48^{\circ}30'\text{S}$ ,  $31^{\circ}\text{E}$  are within the region where the age offset should vanish but instead of becoming flatter, the anomalies show a broad depression over all three Bain fractures. The heights of the geoid on either side of the depression are about equal, however, and may indicate similar seafloor ages. At  $48^{\circ}\text{S}$ ,  $32^{\circ}\text{E}$ , the deepest part of the geoid anomaly is centered on the two eastern fractures of Bain where they coalesce. North of this a depression is again centered on the western member of Bain and the height of the anomaly increases to the east over the younger seafloor. In this discussion of the anomalies we have avoided interpretations of the seafloor between Bain and Prince Edward Fracture Zones which is conceivably the most interesting since it involves the largest amount of offset along the spreading ridge. However, without additional data such as magnetic anomalies or well located earthquakes with known focal mechanisms, such interpretations would be highly speculative.

The geoid offsets across DuToit, the two members of Prince Edward, and Discovery II fracture zones follow the expected inverse relationship between geoid height and age of the seafloor. On the majority of profiles, a small dip in the geoid is centered above the deep fracture zone axis. Because of the oblique, rather than more nearly perpendicular angle between track lines and Indomed Fracture Zone, it is difficult to identify the geoid offset in the profiles that cross the fracture zone.

#### Along-Track Deflection of the Vertical

In contrast to geoid profiles, deflection of the vertical profiles (Figure 4) emphasize the short-wavelength, local anomalies rather than the larger amplitude intermediate and long-wavelength anomalies. The broad, positive anomaly seen across the spreading ridge in the geoid profiles is no longer obvious. In Figure 4 the gradient has been calculated so that a positive anomaly (plotted to the east of the track line) corresponds to a slope in the geoid down towards the southeast. Two distinctive types of anomalies can be seen; isolated dipoles consisting of adjacent positive and negative peaks having approximately equal amplitudes that mark the positions of seamounts, and series of anomaly peaks that are parallel to fracture zone traces and that can be correlated across several track lines. Bain Fracture Zone, which was seen to have the largest age and geoid offsets also has the largest gradient anomalies. They extend from the southern limit of the chart to approximately  $44^{\circ}\text{S}$  and trend  $\text{N}30^{\circ}\text{E}$ , parallel to the fracture zone traces. Directly south of the ridge-transform intersection at  $52^{\circ}50'\text{S}$ ,  $27^{\circ}30'\text{E}$  along the western member of Bain Fracture Zone, the deep fracture zone axis is situated between a  $110 \mu\text{rad}$  positive and a  $-25 \mu\text{rad}$  negative anomaly with the positive peak lying  $\sim 15 \text{ km}$  to the west of the fracture zone trace. The amplitude of the positive anomaly

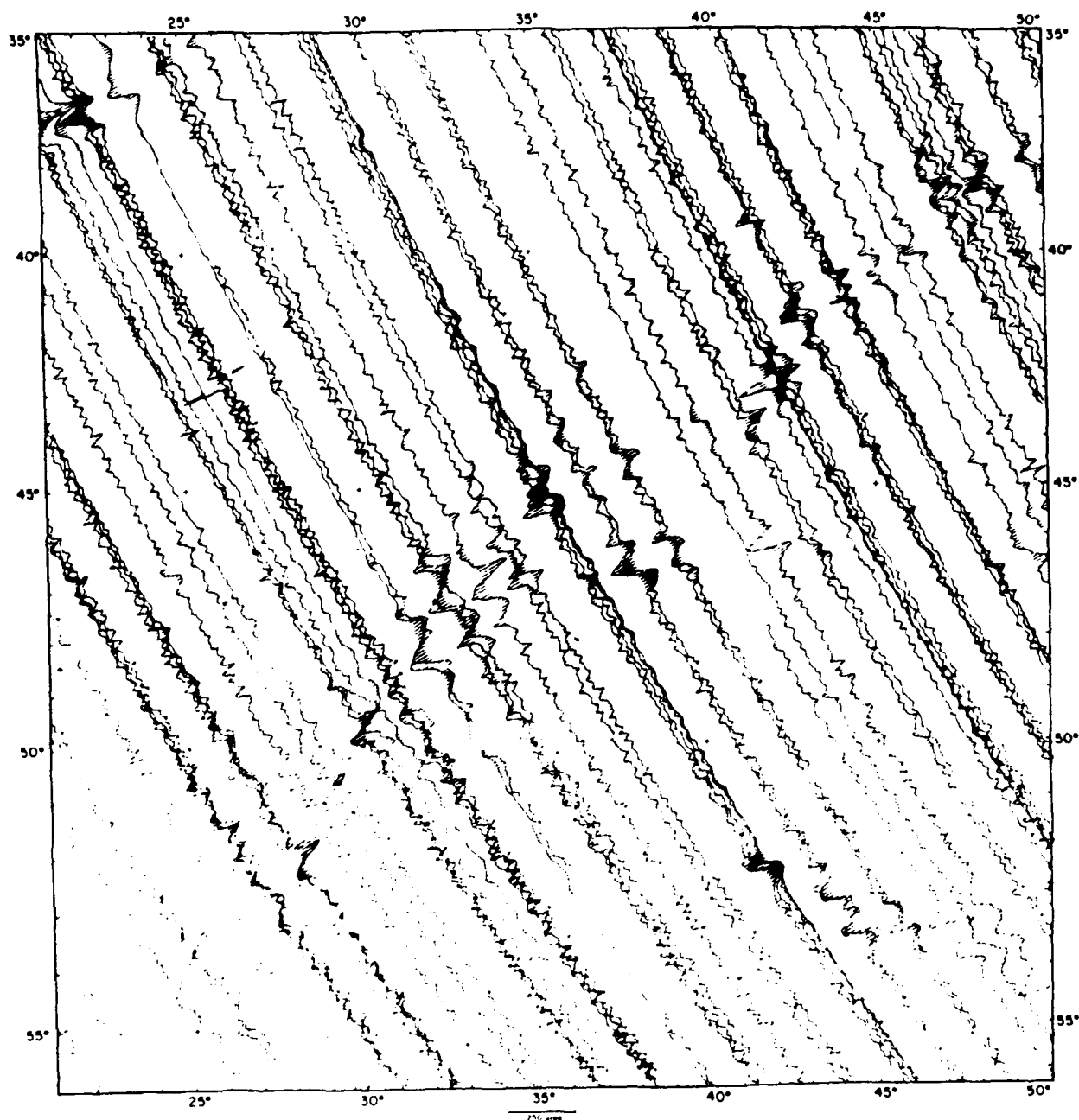


Figure 4. Geoid gradients along ascending arcs of the satellite plotted perpendicular to subsatellite track lines.

decreases south of the intersection in response to the broadening of the geoid step. The next two fractures east of the westernmost Bain fracture zone member are associated along their entire lengths with smaller amplitude gradients, the largest of which is  $-115 \mu\text{rad}$  at  $48^\circ\text{S}$ ,  $32^\circ\text{E}$  where the bathymetric expressions of the fractures end abruptly. The remaining fracture, directly west of Prince Edward Fracture Zone lies between a positive and negative gradient, the larger positive anomaly consistently located 10-15 km to the west of the fracture zone axis and the smaller, negative anomaly either overlying or 5-10 km to the east of the axis.

DuToit and the two members of the Prince Edward Fracture Zone also have gradient anomalies similar to those seen over the western member of the Bain Fracture Zone. The deep fracture zone axes are bordered on the west by positive gradients and on the east by negative anomalies. In response to the change in geoid offset, the positive anomaly peak is larger than the negative peak south of the spreading ridge and smaller than the negative peak north of the ridge crest along the inactive section of the fracture zone.

Discovery II and Indomed Fracture Zones are less apparent than the other fracture zones in the gradient profiles primarily because of the angle at which the track lines cross the fracture zones and the relatively small number of track lines. Large positive anomalies can be seen on the southern, inactive sections of Discovery II and negative anomalies on the northern, inactive sections, but it is difficult to identify these as fracture zone signals because the north-south correlation across track lines is not readily apparent.

From the geoid gradient and bathymetry comparison it is seen that the highest amplitude geoid gradient anomalies (positive or negative) are

consistently located 10-20 km away from the bathymetric axes of the major fracture zones and occur above the younger lithosphere (Figures 2 and 4). This is in contrast to previous thermal and mechanical models of fracture zones that have predicted that the maximum gradient anomaly overlies the boundary between the two sections of the lithosphere (Sandwell, 1984a; Parmentier and Haxby, 1985). The accuracy in location of the gradient anomaly is estimated to be  $\pm 5$  km where the fracture zone is crossed by a satellite track. The accuracy of the topographic portrayal depends on the navigational error and density of ship tracks. A reasonable assumption is that the ship positions are accurate to  $\pm 1$  km in this region of predominantly satellite-navigated tracks. Within observational error, the offset in the fracture zone axes and geoid gradients is significant. The fracture zone valleys are approximately 10-15 km wide and the gradient peaks generally occur outside this region. The trend of the gradient anomalies closely follows the fracture zone traces, however, and are, therefore, assumed to be related to the fracture zone bathymetry and thermal structure. In order to investigate possible effects of the fracture zone valley and surrounding ridges on the geoid anomaly, simple thermal and mechanical models will be used to predict the geoid over observed bathymetric profiles. The construction of the bathymetric profiles and the observed correlations between the bathymetric, geoid, and deflection-of-the-vertical profiles calculated using the gridded data is discussed in the next section.

#### Gridded Bathymetry, Geoid and Deflection of the Vertical

Profiles along ascending track lines enabled us to identify anomalies in the geoid and deflection of the vertical profiles that are characteristic of fracture zone traces. In order to demonstrate clearly

the relationships between geoid, deflection of the vertical and bathymetry anomalies and to utilize simultaneously the data along both ascending and descending track lines, gridded data were used to construct coincident profiles. The gridded data are displayed using an image processing system where each grid point is given a color representing its value (Figures 5, 6, 7). This is an ideal method for presentation because it bypasses the need for contouring algorithms that can produce blocky or excessively smoothed contours, or close up contours within a continuous linear feature, thereby reducing the apparent linearity of the feature. The geoid and deflection-of-the-vertical images (Figures 5,6) were produced by projecting the geoid height values onto a stereographic projection with the pole of the projection in the center of the map. This projection, rather than the Mercator projection of the previous figure was used because it introduces less distortion in distance across the map. This was necessary because the method we used to calculate deflection of the vertical includes a Fourier transform algorithm that assumes a constant distance between grid points in both the x and y-directions. The geoid values were then interpolated onto an 8-km square grid using a minimum curvature fitting technique (Briggs, 1974; Swain, 1976). This technique fits a smooth surface to the data points and preserves maximum and minimum data values, rather than computing a weighted mean value at each grid point.

Deflection of the vertical values were computed from the gridded geoid heights using the Fourier transform. Although they can also be computed by calculating differences between grid points, working in the frequency domain allows simple smoothing algorithms to be used and the calculation of fields dependent on wavenumber such as the gravity field. If  $N(x,y)$  is the geoid height, then

Figure 5. Map of geoid heights from Seasat data interpolated onto an 8-km grid. A stereographic projection is used with the pole of the projection in the center of the map.

Figure 6. Deflection of the vertical calculated at an angle of  $0^\circ$  relative to east. Projection and interpolation as in Figure 5.

Figure 7. Bathymetry digitized from map presented in Figure 2 and interpolated onto an 8-km square grid. Projection as in Figure 5. Contours in the southeast corner,  $43^\circ\text{E}$ - $50^\circ\text{E}$  and  $48^\circ\text{S}$ - $56^\circ\text{S}$  were digitized from GEBCO chart 5.13 (Hayes and Vogel 1981).



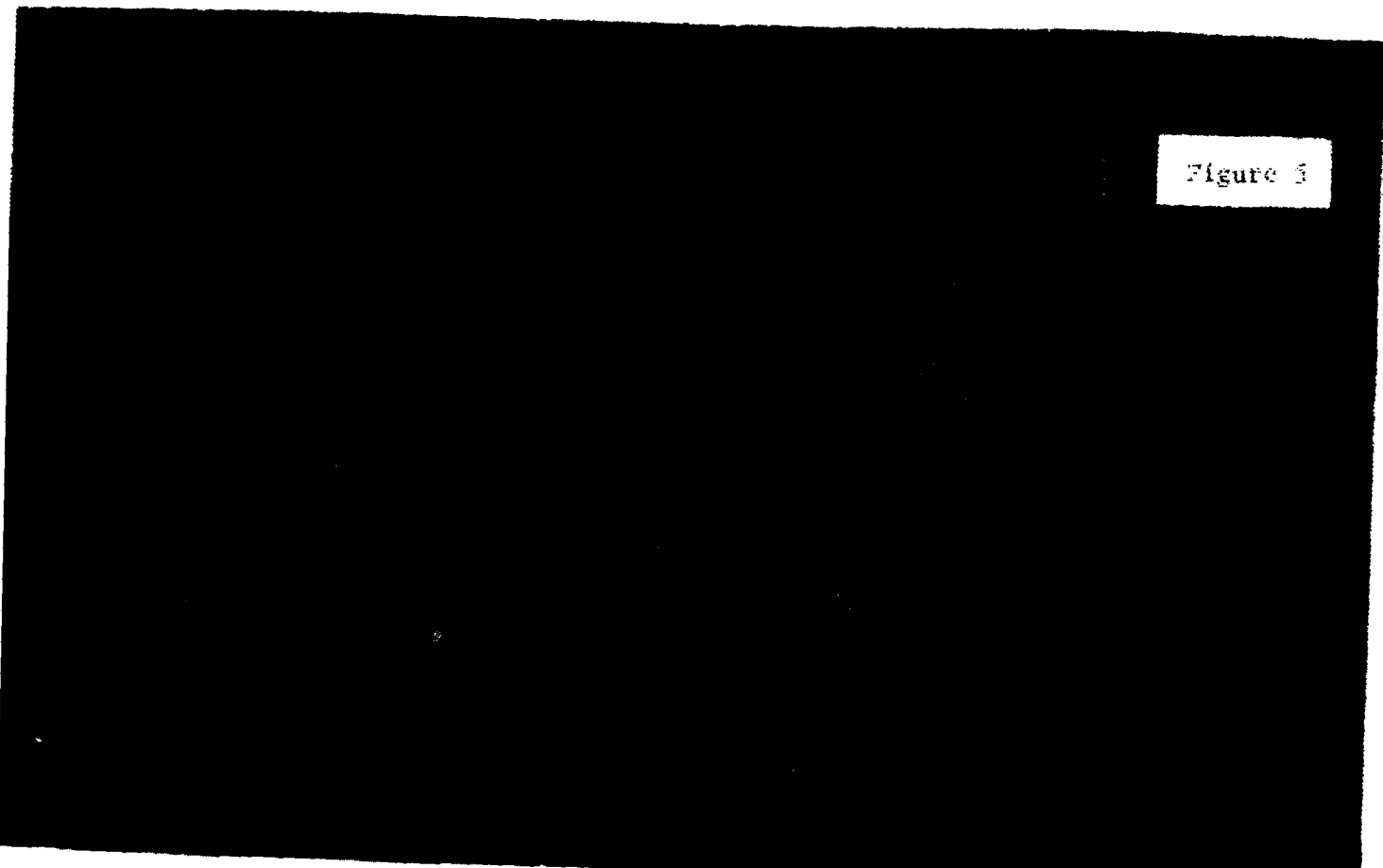


Figure 5



$$\zeta = \frac{-dN}{\partial x}$$

$$\text{and } \eta = \frac{-dN}{\partial y}$$

are the east and north components of the deflection of the vertical, and the Fourier transform is defined by:

$$G(u,v) = \frac{1}{\sqrt{2\pi}} \int_{-\infty}^{\infty} \int_{-\infty}^{\infty} g(x,y) e^{-i(ux+vy)} dx dy = F(g(x,y))$$

$$g(x,y) = \frac{1}{\sqrt{2\pi}} \int_{-\infty}^{\infty} \int_{-\infty}^{\infty} G(u,v) e^{+i(ux+vy)} du dv = F^{-1}(G(u,v))$$

then:

$$\zeta(x,y) = F^{-1}[-iu F(N(x,y))]$$

$$\eta(x,y) = F^{-1}[-iv F(N(x,y))]$$

where  $u$  and  $v$  are the wavenumbers in the  $x$  and  $y$  directions. Similarly, deflection of the vertical at any other angle  $\theta$  (measured counter-clockwise from the east) can be calculated using:

$$\zeta_{\theta}(x,y) = F^{-1}[-i(\cos\theta \cdot u + \sin\theta \cdot v)F(N(x,y))]$$

Because fracture zones are generally associated with geoid steps, deflection of the vertical anomalies computed at an angle perpendicular to the step will have the largest amplitude. In Figure 6 an angle of  $0^{\circ}$  was used, which is close to being orthogonal to the fracture zones.

Bathymetry presented in Figure 2 was interpolated onto the same grid. The bathymetric contours were first digitized and then projected using the same stereographic projection as used for the geoid heights (Figure 7). At this stage of the analysis the additional bathymetric data for the southeast corner,  $43^{\circ}\text{E}$ - $50^{\circ}\text{E}$  and  $48^{\circ}\text{S}$ - $56^{\circ}\text{S}$ , were not yet incorporated into

Figure 2 and contours from GEBCO chart 5.13 (Hayes and Vogel 1981) were digitized instead. The development of geoid and deflection of the vertical anomalies across fracture zones from south of the spreading ridge to north of the ridge is examined using profiles interpolated from the gridded maps. Profile locations are shown in Figure 8. The geoid step at the southern ridge-transform intersection across DuToit Fracture Zone (Fig. 9-AA') is higher over the younger seafloor, as seen in the along-track profiles, and has an amplitude of about 2 m. This corresponds to an age offset of 12-13 my which is the age offset estimated from the transform length and spreading rate. The 45  $\mu$ rad positive deflection of the vertical anomaly lies ~10 km west of the fracture zone axis. Within the active transform (Figure 9-BB') the age offset decreases and the amplitude of the geoid anomaly decreases to 1 m. The 30  $\mu$ rad positive anomaly here lies directly over the clearly defined, 2 km deep transform (5000 m deep with 3000 m high valley walls). At the northern ridge-transform intersection (Figure 9-CC') a 1.8 m-deep depression in the geoid lies directly above the fracture zone instead of the expected geoid step. This may be caused by the gravitational contribution from an isolated 3500 m peak lying just to the west of the ridge-transform intersection (Figure 2) superimposed on the geoid anomaly associated with the thermal offset. Farther north the geoid anomaly never develops into a distinct step across DuToit although a 0.2 to 0.5 m depression in the geoid marks the position of the fracture zone (Figures 9-DD', EE', FF').

The geoid anomaly over the eastern member of Prince Edward Fracture Zone is similar to the that over DuToit. At the southern ridge-transform intersection (Figure 9-II') a 35  $\mu$ rad positive anomaly lies ~20 km to the west of the axis, and is flanked on the east by a 20  $\mu$ rad negative anomaly.

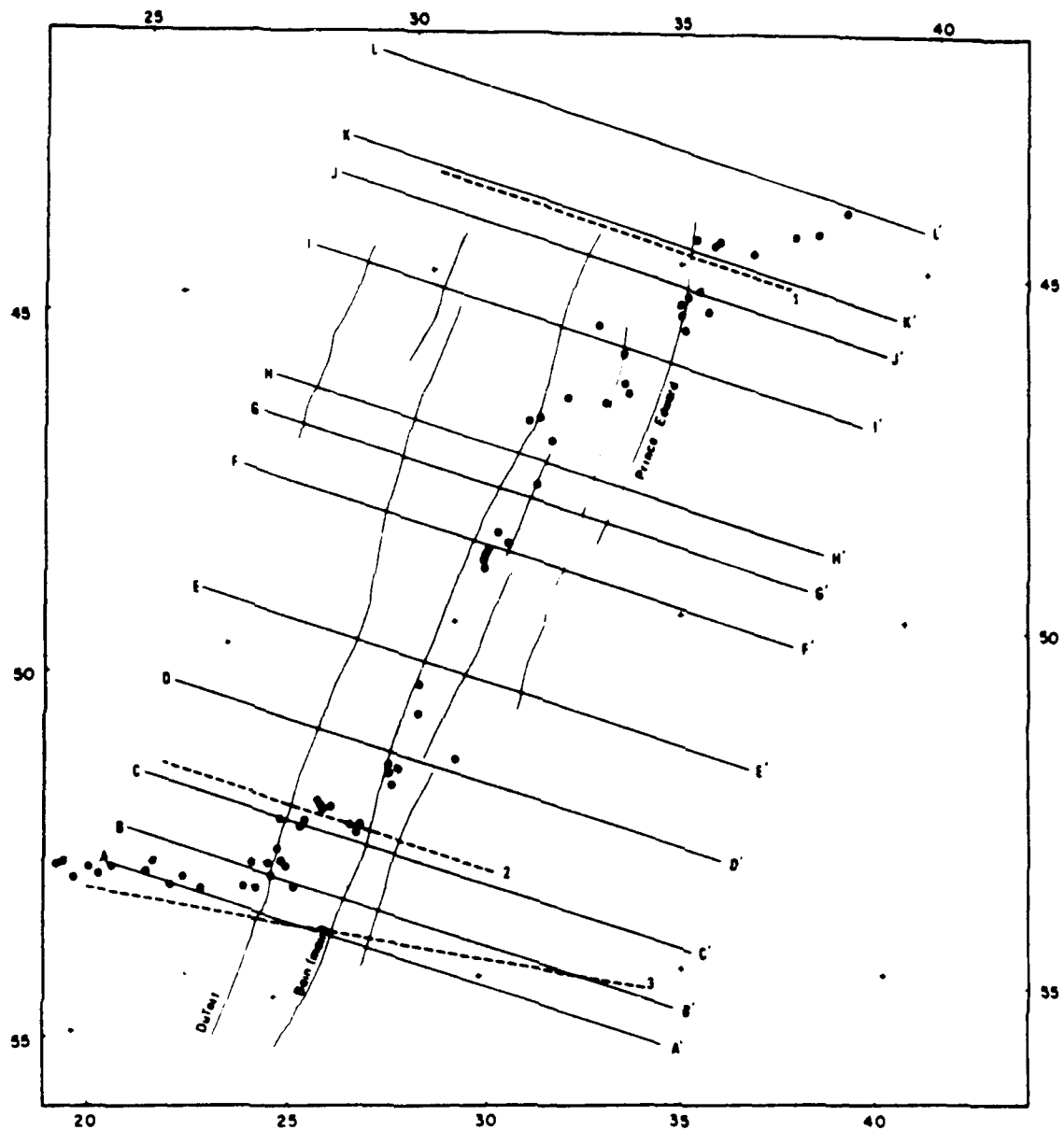


Figure 8. Locations of profiles shown in Figures 9, 13, 14, and 15. Thin lines show fracture zone traces and solid circles indicate earthquake epicenters.

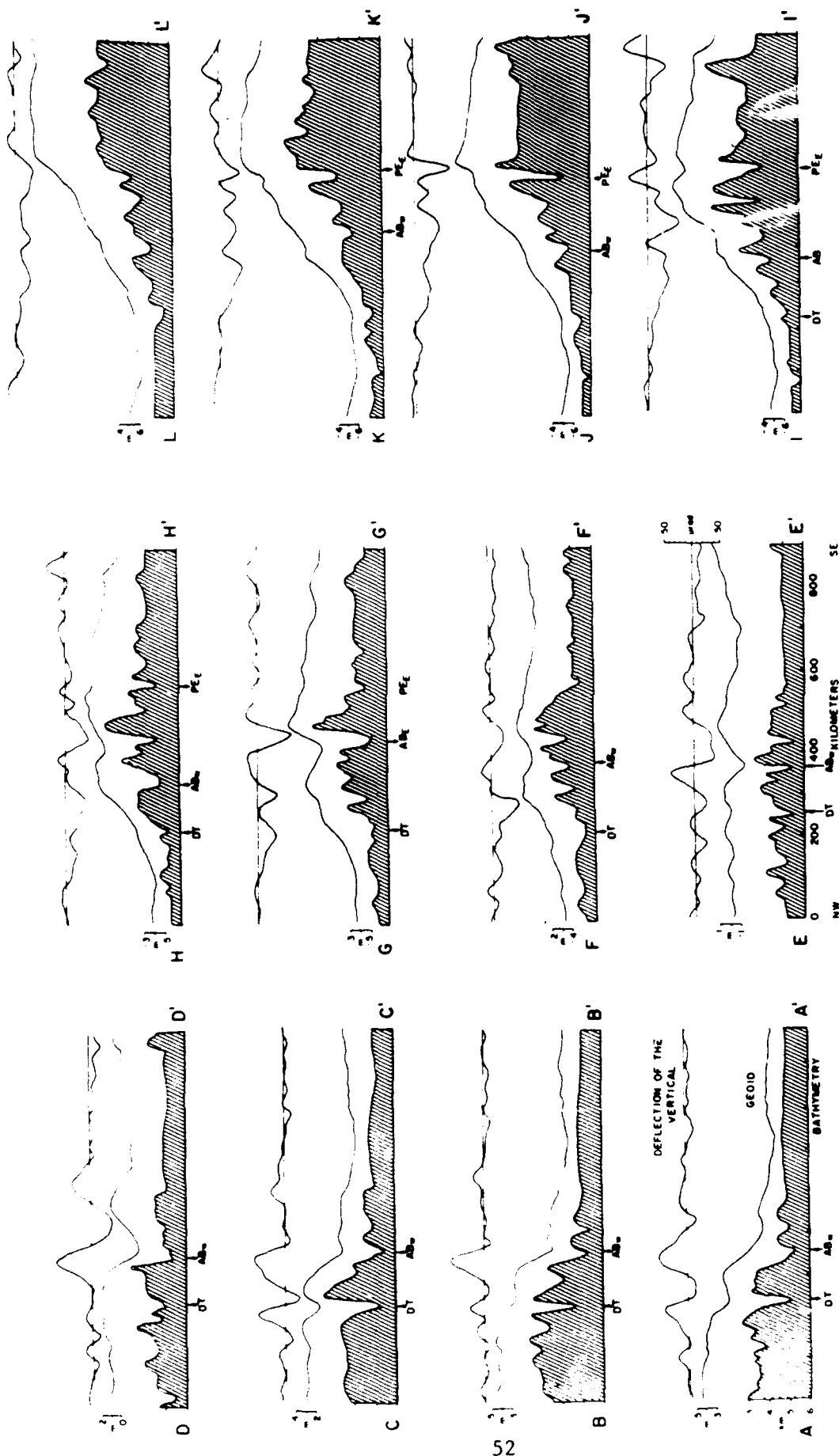


Figure 9. Profiles of bathymetry, geoid height and deflection of the vertical across the Dufault, Bain and Prince Edward Fracture Zones. Profiles are interpolated from maps presented in Figures 5, 6, 7.

Slightly north of the midpoint between the two ridge crests (Figure 9-JJ') the geoid step has changed direction in response to the change in age-offset of the seafloor across the fracture zone. A large,  $-65 \mu\text{rad}$  deflection of the vertical anomaly is centered slightly east of the fracture zone. At the northern ridge-transform intersection (Figure 9-KK') a  $-40 \mu\text{rad}$  anomaly lies slightly east of the fracture zone. This negative anomaly can be followed 300 km north of the northern ridge-transform intersection and the positive anomaly 450 km south of the southern intersection.

The complexities of the Bain Fracture Zone complex were discussed in the previous sections and only two general points are noted here. First, the geoid anomaly south of the active transform (Figures 9-AA', BB', CC') and north of the transform (Figures 9-II'-LL') show the expected, monotonic increase in age away from the spreading ridge. Secondly, although the geoid low east of Bain in Figure 9-DD' appears to be related to a deep section of seafloor, directly north of this (Figure 9-EE'), an elevated section of the seafloor underlies the geoid low. Obviously, this points out a need for additional data in this area in order to understand the nature of highly sheared sections of seafloor.

The comparisons between the geoid, deflection of the vertical, and bathymetry profiles clearly show the characteristics of the anomalies across fracture zones. The geoid step that is predicted from cooling models of the oceanic lithosphere is generally discernable over the larger offset fracture zones but is not centered on the deep bathymetric axis. Instead, a slight depression or break in slope overlies this axis. The maximum gradient anomaly that is predicted by thermal modeling to overlie the boundary between the two sections of oceanic lithosphere is generally

offset 10-15 km away from the deep bathymetric fracture zone axis and occurs over the younger lithosphere. These discrepancies between the cooling model predictions and the observations suggest that additional, unmodeled effects such as the deep fracture zone valley and transverse ridges are significantly influencing the shape of the geoid anomaly. Also, the closeness of the fracture zones will result in a superposition of the geoid anomalies. In the next section, simple models of the density structure across fracture zones and seafloor topography are used to investigate the combined effects of the thermal contrast and of ridges and troughs at a fracture zone.

### Modeling

The geoid and bathymetry profiles analyzed here were interpolated from the gridded data sets. Because we have used interpolated data, no attempt is made to match perfectly the modeled and observed profiles. Instead, our purpose is to determine whether the observed data are consistent with the proposed thermal models, and whether by including the effects of the topography the general characteristics of the anomalies can be explained.

Thermal Edge Effect: The narrow spacing of the large-offset fracture zones along the Southwest Indian Ridge results in a superposition of the gravitational edge effects from each fracture zone. In order to account for this superposition, we have derived the solution for the temperature structure across two fracture zones separating oceanic crust of three different ages. The effects of a finite plate thickness and flexure across the fracture zone have not been included in order to simplify the model. The initial temperature structure across the left fracture zone is the lateral and vertical cooling solution for a semi-infinite half-space (Louden and Forsyth, 1976; Sandwell and Schubert, 1982):



$$T'(x,z,t_1) = \frac{T_m}{2} \left( \operatorname{erfc} \frac{x-x_1}{2\sqrt{\kappa t_1}} \operatorname{erf} \frac{z}{2\sqrt{\kappa t_0}} + \operatorname{erfc} \frac{-(x-x_1)}{2\sqrt{\kappa t_1}} \operatorname{erf} \frac{z}{2\sqrt{\kappa t_1}} \right)$$

where

$x_1, x_2$  are the locations of the fracture zones

$t_0$  = age of oldest lithosphere

$t_1$  = age of youngest lithosphere

At time  $t_1$ , a second fracture zone is placed to the right of the first and the temperature of the lithosphere to the right of the second fracture zone is simply the mantle temperature  $T_m$  (Figure 10). The final temperature distribution as a function of time can be expressed as a Green's function solution and is derived in the Appendix. Using this temperature structure the density can be determined using the equation of state:

$$\rho(x,z,t) = \rho_m(1 - \alpha(T(x,z,t) - T_m))$$

Local compensation of the cooling lithosphere requires that seafloor depth increase with time such that:

$$d(x,t) = d_{\text{ref}} + \frac{\alpha \rho_m}{(\rho_m - \rho_w)} \int_0^{\infty} (T_m - T(x,z,t)) dz$$

Geoid heights were calculated by dividing the model into a surface mass layer equivalent to the topography (all material above the deepest seafloor) overlying a variable density lithosphere. For the surface mass layer,  $\rho(x,z)$  is a constant taken to be the density of oceanic mantle material at  $0^\circ$  C. The gravitational potential can be calculated using the Bouguer Formula:

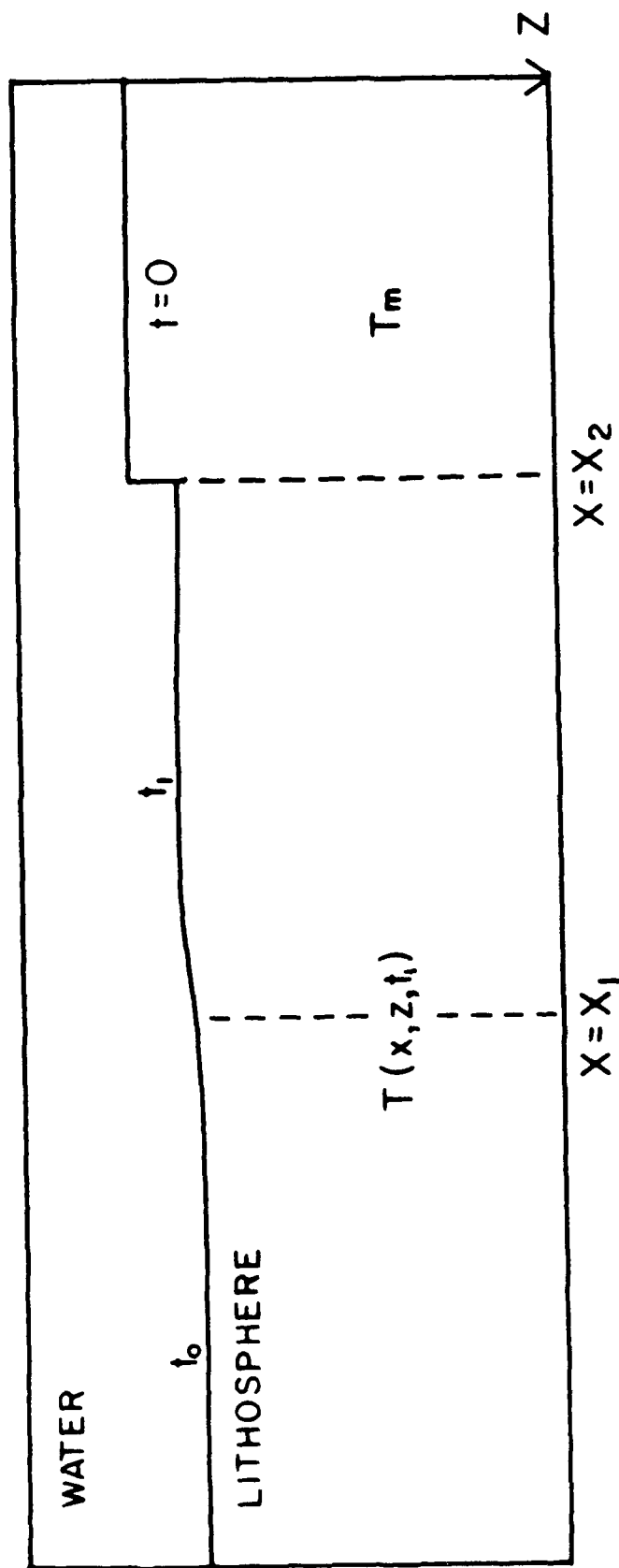


Figure 10. Initial temperature distribution across two fracture zones. The left side has cooled vertically and horizontally across the fracture zone at  $x=x_1$ . The right side is at the ridge crest with a constant temperature  $T_m$  and is bordered on the left by a fracture zone at  $x=x_2$ .

$$F(N(x,z)) = \frac{2\pi G}{|u|g} \exp(-|u|z) F(h(x) \cdot \rho(x,z))$$

where

$z$  = depth to base of the layer

$h(x)$  = topography or layer thickness

The effect of the lithosphere below the topography was computed by dividing the lithosphere horizontally into slabs of equal thickness,  $\Delta z$ , and calculating the density at the midpoint of the slabs for each data point. The gravitational potential for each slab was calculated using the above formula with  $h(x)$  set equal to  $\Delta z$ . The total geoid height was obtained by summing the separate components:

$$F(N(x,z)) = \frac{2\pi G}{|u|g} \left[ \rho_0 F(H(x)) \exp(-|u|z) + \Delta z \sum F(\Delta \rho_i(x,z)) \exp(-|u|z_i) \right]$$

The geoid step seen initially across the fracture zones increases in width with age as a result of diffusion of the sharp density/temperature gradient across the fracture zone and an increase in the depth of compensation (Detrick, 1981). As a result, the gradient of the geoid decreases (Sandwell, 1984a). This effect is shown in Figure 11a for two fracture zones that initially separate seafloor of ages 0/10 and 10/30 Ma. The geoid gradient is shown for successive 5 m.y. intervals as the fracture zone ages. Figure 11b shows the geoid gradient in a contoured plan view of the fracture zones in order to show how these anomalies would appear on a contour chart. The vertical scale is chosen to reflect a spreading rate of  $0.8 \text{ cm yr}^{-1}$ . The amplitude of the gradient decreases rapidly and the initial peak in the gradient anomaly broadens with time (Sandwell, 1984a). The distance between fracture zones significantly affects the shape of the geoid and gradient anomalies. This is demonstrated in Figure 12 where two

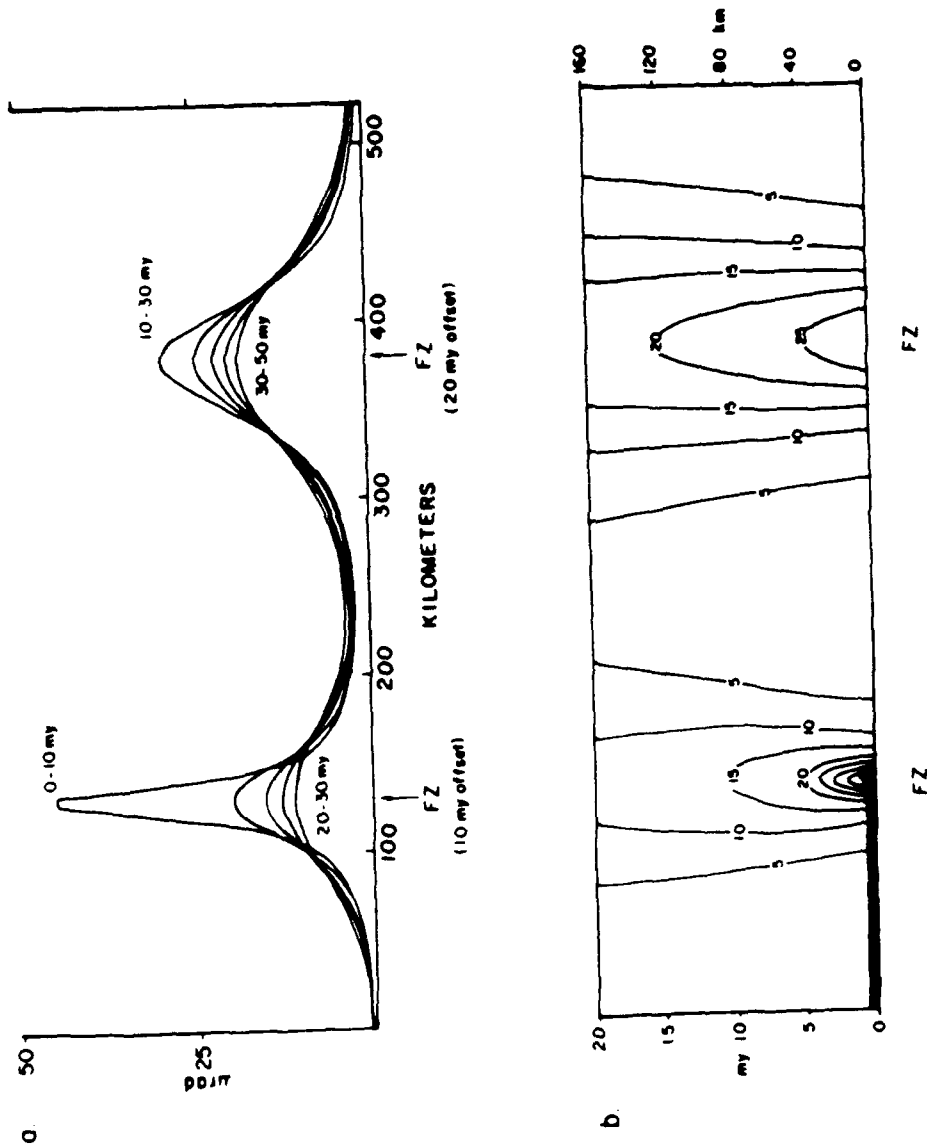


Figure 11. (a) Geoid gradients calculated across two fracture zones, one at 130 km, the other at 380 km. The initial age offsets across these fracture zones are 10 and 20 my, respectively, and gradients are calculated at 5 my intervals across successively older sections of seafloor. (b) Plan view of the geoid gradient across two adjacent fracture zones. The heavy solid line segment marks the position of the ridge crest. Contours are in  $\mu\text{rad}$ .

fracture zones separate seafloor of ages 2/20 and 20/32.5 Ma. Similar age offsets occur across the Prince Edward Fracture Zone. The separation between the fracture zones is decreased from 275 km to 170, 120 and 70 km. At the largest separation the geoid and gradient anomalies are distinct for each fracture zone and the geoid between the fracture zones is fairly flat. At a separation of 170 km ( $X_2-2$  on Figure 12) the peaks in the geoid gradient begin to coalesce. At the shortest separation of 70 km (the actual spacing of these fracture zones) the geoid steps are no longer distinct from one another and the geoid heights over the 20 m.y. seafloor are up to 0.8 m less than expected. The geoid gradients have coalesced into a broad, bimodal anomaly. These results indicate that it would be fairly difficult to determine the locations of closely-spaced fracture zones from their geoid or gradient anomalies unless the age offset were large. This is assuming that only the thermal cooling effects are represented in the geoid anomalies and ignores possible topographic contributions.

Using this model we have calculated the geoid anomaly over the Bain-Prince Edward complex along line 1 of Figure 8. An age of 22 my was used for the seafloor between the two fractures although there is at least one small-offset fracture zone between them. The two fractures were placed at 300 km and 425 km, beneath the deepest part of the fracture zone. The shapes of the theoretical and Seasat geoid are similar (Figure 13) although there are significant differences between them. The calculated gradient cannot account for the short-wavelength features present in the observed field but the larger-wavelength negative gradient peaks in the observed and calculated gradients have similar amplitudes. The calculated geoid gradient is offset by 10-15 km from the observed gradient. This could be

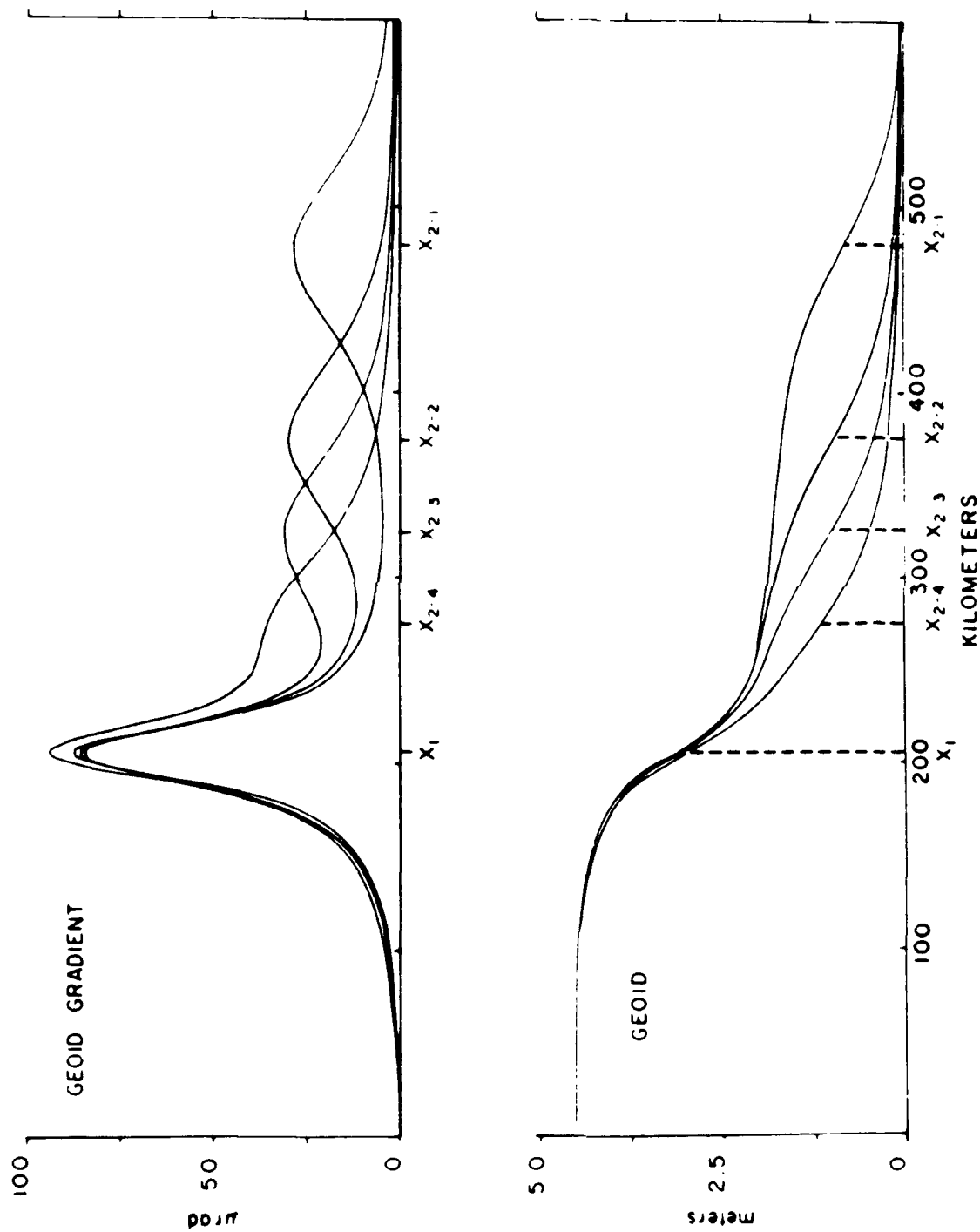


Figure 12. Effects of decreasing the distance between two fracture zones. The fracture zones at  $X_1$  and  $X_2$  separate seafloor with ages 2/20 and 20/32.5 Ma. The position of the fracture zone at  $X_1$  is fixed at 205 km and the geoid and geoid gradients are calculated for positions of the second fracture zone at 275, 325, 375 and 480 km.

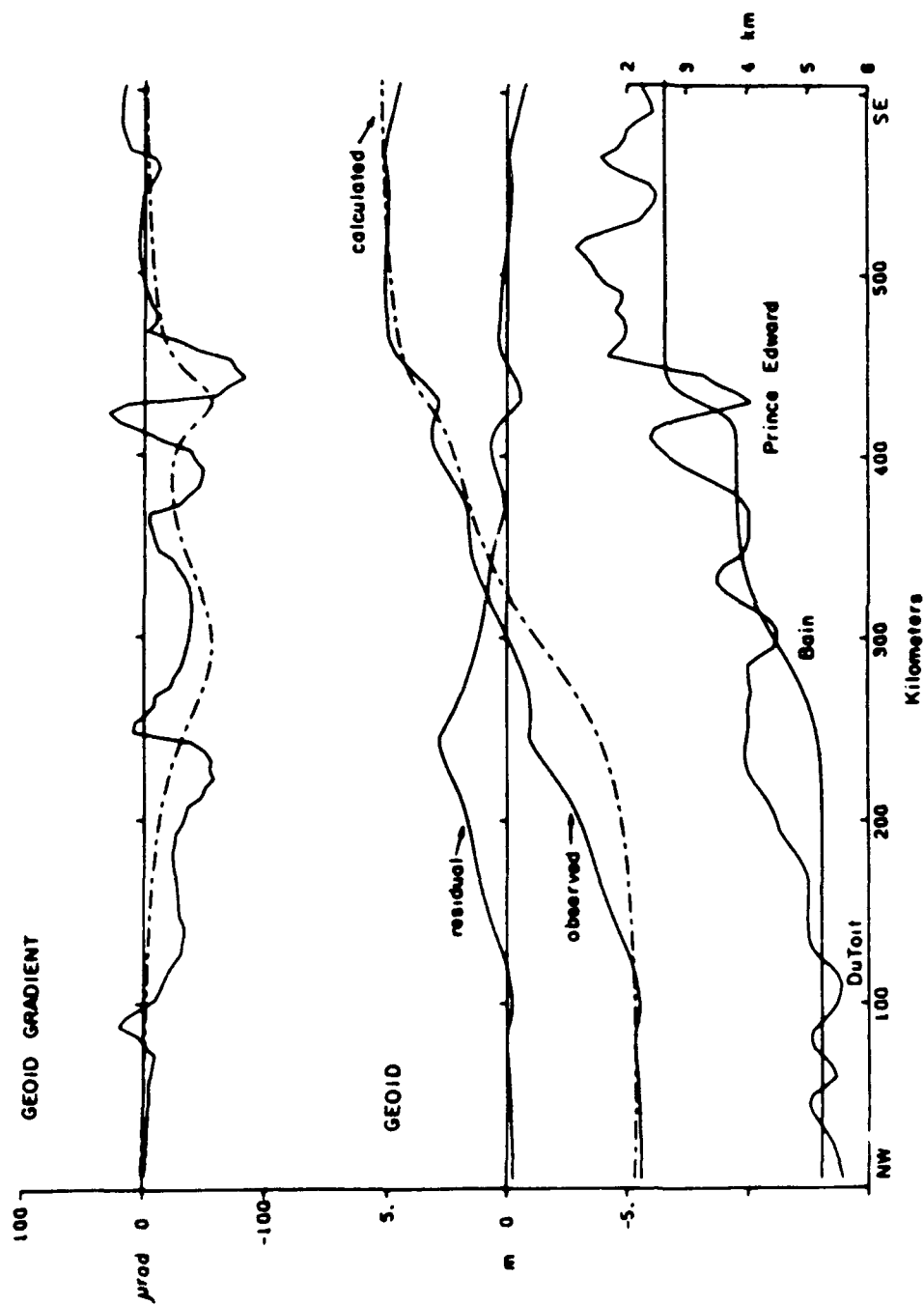


Figure 13. Bathymetric profile across DuToit, Bain and Prince Edward Fracture Zones and geoid profile interpolated from gridded Seasat altimetry, both along line 1 of Figure 8. Theoretical depth and geoid profiles were calculated for half-space vertical and lateral cooling across two fracture zones, one at 300 km and the other at 425 km. Ages from west to east are 75, 20 and 1 my. The upper profile compares geoid gradients calculated from the observed geoid (solid line) and theoretical geoid (dot-dashed line).

changed by moving the position of the fracture zone from 425 km to 435-440 km but in the next section when the effects of the topography are accounted for, this is seen to be unnecessary.

Another example of the dependence of the long-wavelength geoid anomaly on age of the seafloor is shown in Figure 14. The profile crosses DuToit and Bain Fracture Zones and is located along line 3 of Figure 8. In this example the fracture zones are again placed beneath the deepest points of the bathymetric profile at 360 km and 470 km. The calculated geoid profile matches the observed fairly well across Bain Fracture Zone (the western member) but is offset from the observed profile above Dutoit. The gradient is also seen to be offset by 20-25 km. The geoid calculated from the thermal model is not expected to match the short-wavelength geoid anomalies although it is normally assumed that the peaks in the observed and calculated gradients should overlie one another. This would require placing the fracture zone position in the thermal model 20-25 km away from the deepest part of the fracture zone towards younger seafloor. Although this is not completely unacceptable in view of our limited understanding of fracture zones, an examination of the effects of the unmodeled topography is needed before reaching such a conclusion.

#### Plate Compensation Model

To test how the short-wavelength geoid anomalies may be related to topographic variations, geoid heights are calculated assuming regional compensation given by a thin-elastic plate model. The relationship between geoid height and topography can be expressed in the Fourier domain by:

$$N(x) = F^{-1} \left\{ \frac{2\pi(\rho_c - \rho_w)G}{|u| \cdot g} \left[ e^{-uz_1} - \left( 1 + \frac{u^4 D}{g(\rho_m - \rho_c)} \right)^{-1} e^{-u(z_1 + t)} \right] F(h(x)) \right\}$$



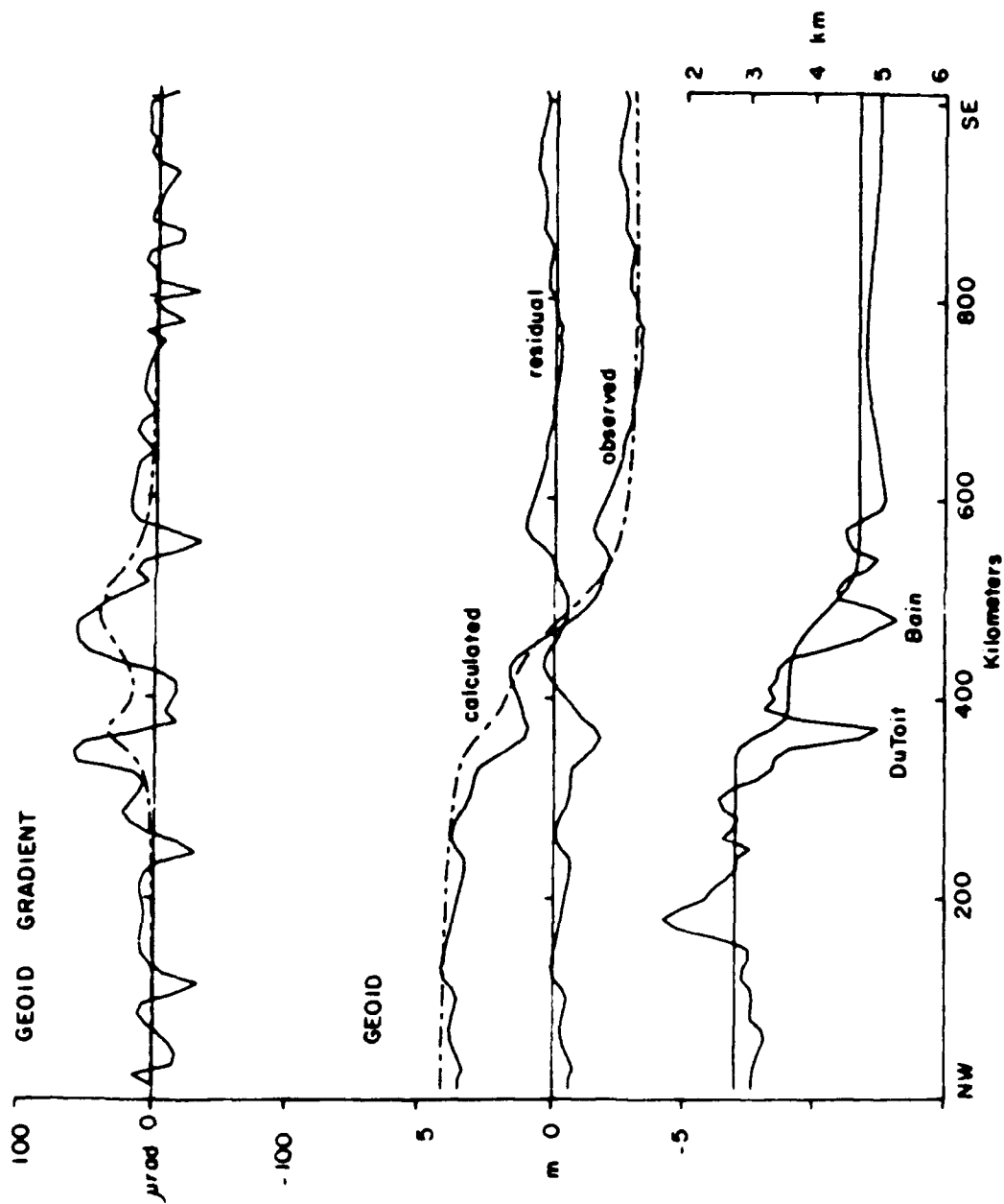


Figure 14. Bathymetry and geoid profiles across DuToit and Bain Fracture Zones located along line 3 of Figure 8. Theoretical geoid profiles calculated for cooling across two fracture zones located at 360 km and 470 km. Ages from west to east are 1 m.y., 15 m.y. and 50 m.y.

where  $z_1$  is the average depth of the topography and  $t$  is average crustal thickness.  $D$  is the flexural rigidity of the plate and for simplicity we have used a constant value rather than one which varies with age of the crust. Using an average crustal thickness of 6 km and elastic plate thicknesses of 6 and 15 km, geoid heights were calculated from the same bathymetric profiles used previously (Figures 13 and 14). In order to compare the shorter-wavelength anomalies in the observed geoid with the calculated anomalies, a 225 km running mean was removed from the observed geoid. Also, the bathymetry profile was tapered at each end to reduce edge-effects produced by the fast Fourier transform. The calculated and observed geoid anomalies are similar in several ways (Figure 15a). Over Prince Edward Fracture Zone and the fracture zone directly west of Prince Edward, shallow, <1 m deep depressions in the observed geoid are also seen in the plate-compensated models. The amplitudes of the anomalies produced by the 15 km thick plate are larger by up to 1 m than those produced by the 6 km thick plate. However, because we have arbitrarily removed a 225 km running mean, it is difficult to determine which plate thickness is more appropriate. Figure 15b shows the combined effects of the thermally-related geoid anomaly and geoid anomaly attributed to the compensation of seafloor topography for an elastic plate thickness of 6 km. The observed and calculated geoid profiles are more closely matched than the profiles which considered only the thermal effects. Including the effects of the topography has shifted the geoid step across Prince Edward Fracture Zone which can be seen most easily in the geoid gradient profiles. The observed and calculated geoid gradient profiles are closely matched and the peaks in the gradient profiles are in phase. The major discrepancies are the negative anomaly calculated over Bain Fracture Zone which is

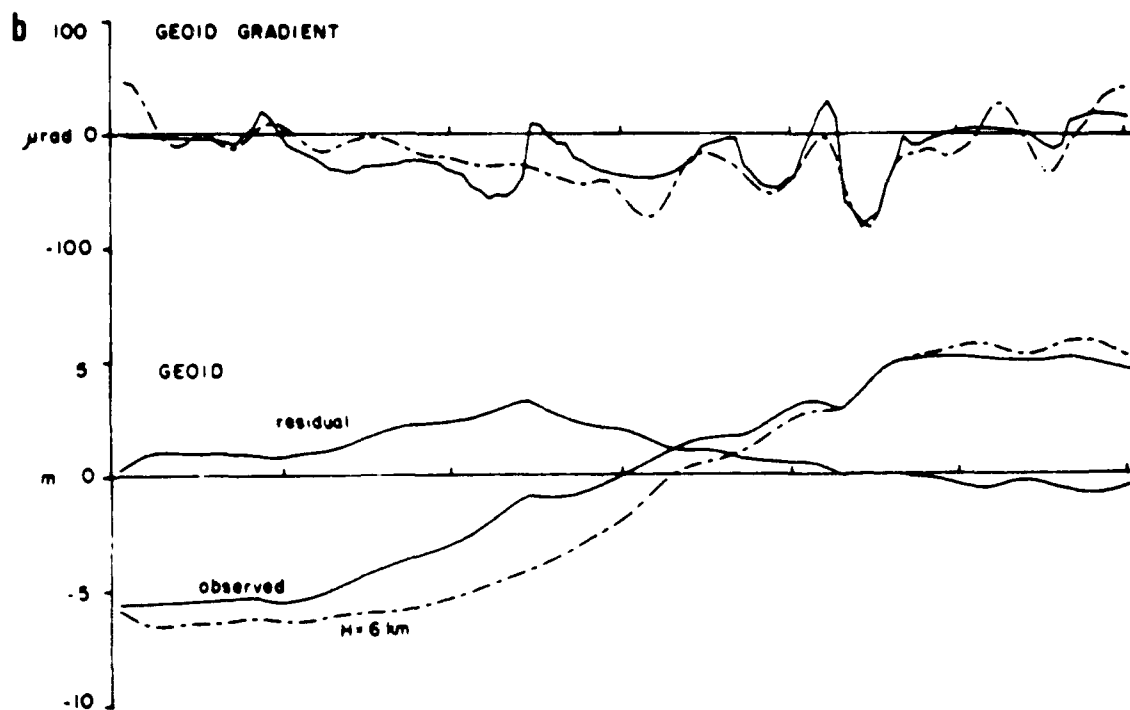
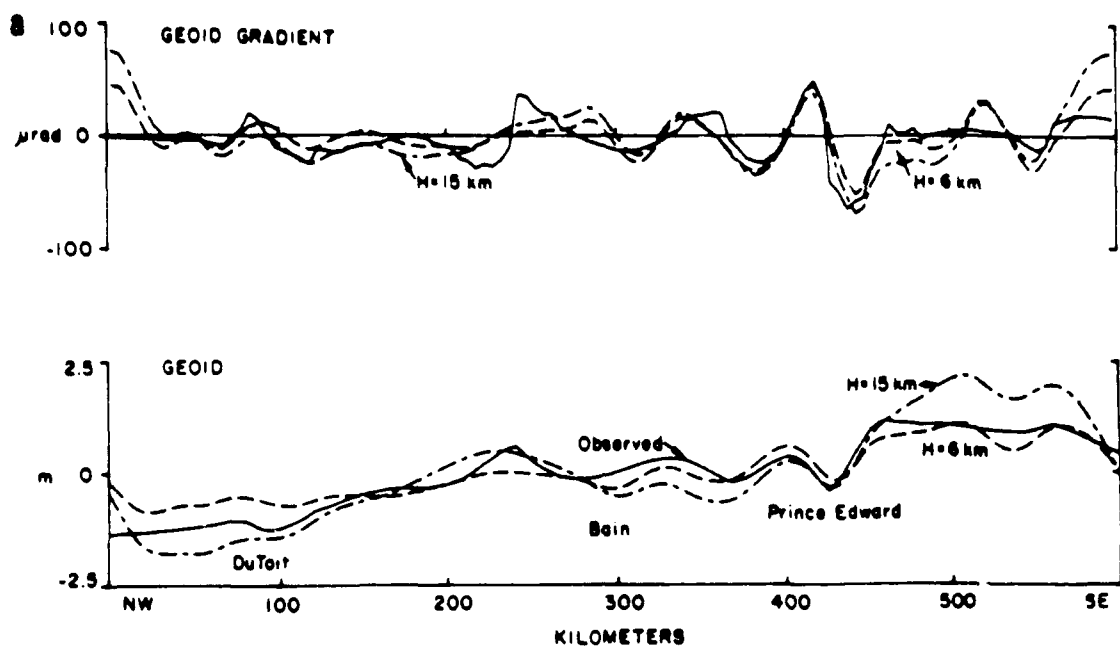


Figure 15a Geoid heights (from Figure 13) with a 225 km running mean removed compared to geoid heights calculated from the observed bathymetric profile (also from Figure 13) using a thin-elastic plate compensation model. Geoid and gradients calculated for plate thicknesses of 6 and 15 km are shown.

15b. Geoid and gradient profiles produced by combining the thermal-offset geoid anomaly (from Figure 13) with the anomaly due to the compensation of seafloor topography for an elastic plate thickness of 6 km (Figure 15a).

narrower than the observed, and the bump in the geoid profile west of Bain which isn't predicted in either the thermal or topographic anomalies.

Including the effects of the topography on the profile first shown in Figure 14a is slightly less satisfying but a similar shift in the position of the gradient anomalies is also seen (Figure 16a and 16b). A further example of the effect of topography on the geoid is shown in Figure 17. This profile crosses the deep transform valley within the active section of DuToit Fracture Zone (Figure 8: profile 2); as before, a 225 km running mean has been removed from the observed geoid heights. The match between the observed and calculated geoid anomalies in this tectonically-uncomplicated example is striking. The anomalies over DuToit and Bain Fracture Zones are very closely matched along both the geoid and geoid gradient profiles. Again, it is difficult to determine which of the plate thicknesses best fits the data. The close match between the observed and calculated anomalies suggests that the geoid gradients, in particular, are significantly affected by the fracture zone topography.

#### Discussion

The usefulness of the Seasat altimeter data for plate reconstruction depends both on its accuracy in identifying and delineating fracture zones and on the extent to which gravity field anomalies can be followed away from the ridge crest. From the comparisons and modeling results it is apparent that along this complex spreading-ridge system it is not possible to tell whether a lineated anomaly directly overlies a fracture zone trace without additional bathymetric data. In general, the axis of the fracture zone coincides with a dip or change in slope in the geoid profile. The trends of the anomalies are closely aligned with those of the fracture zones and should also lie on small-circles about the same rotation pole.

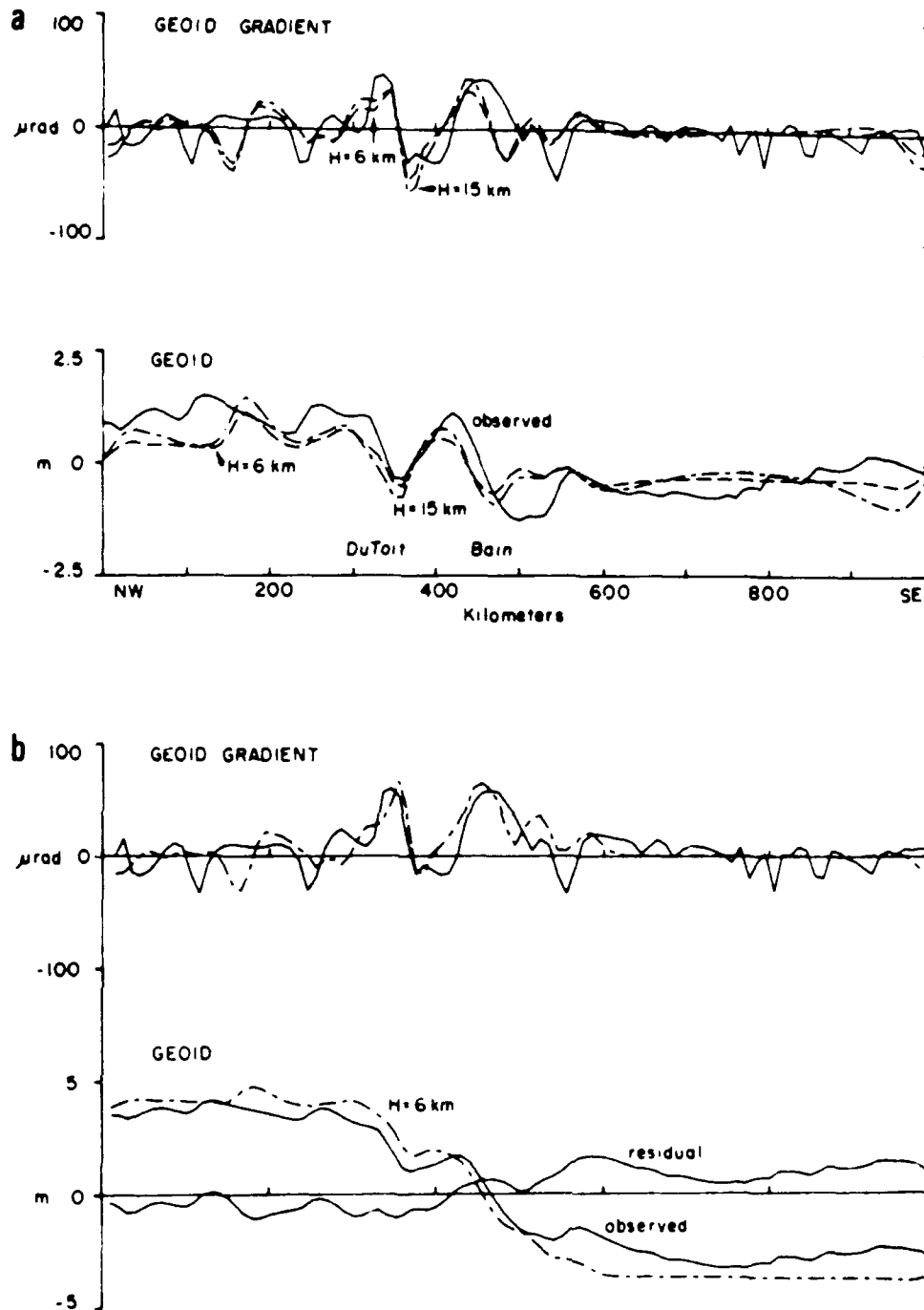


Figure 16a. Geoid heights (from Figure 14) with a 225 km running mean removed, compared to geoid heights calculated from the observed bathymetric profile using a thin-elastic plate compensation model. Geoid heights and gradients for plate thicknesses of 6 km and 15 km are shown.

Figure 16b. Geoid and gradient profiles produced by combining the thermal-offset geoid anomaly (from Figure 14) with the anomaly due to the compensation of seafloor topography for an elastic plate thickness of 6 km (Figure 16a).

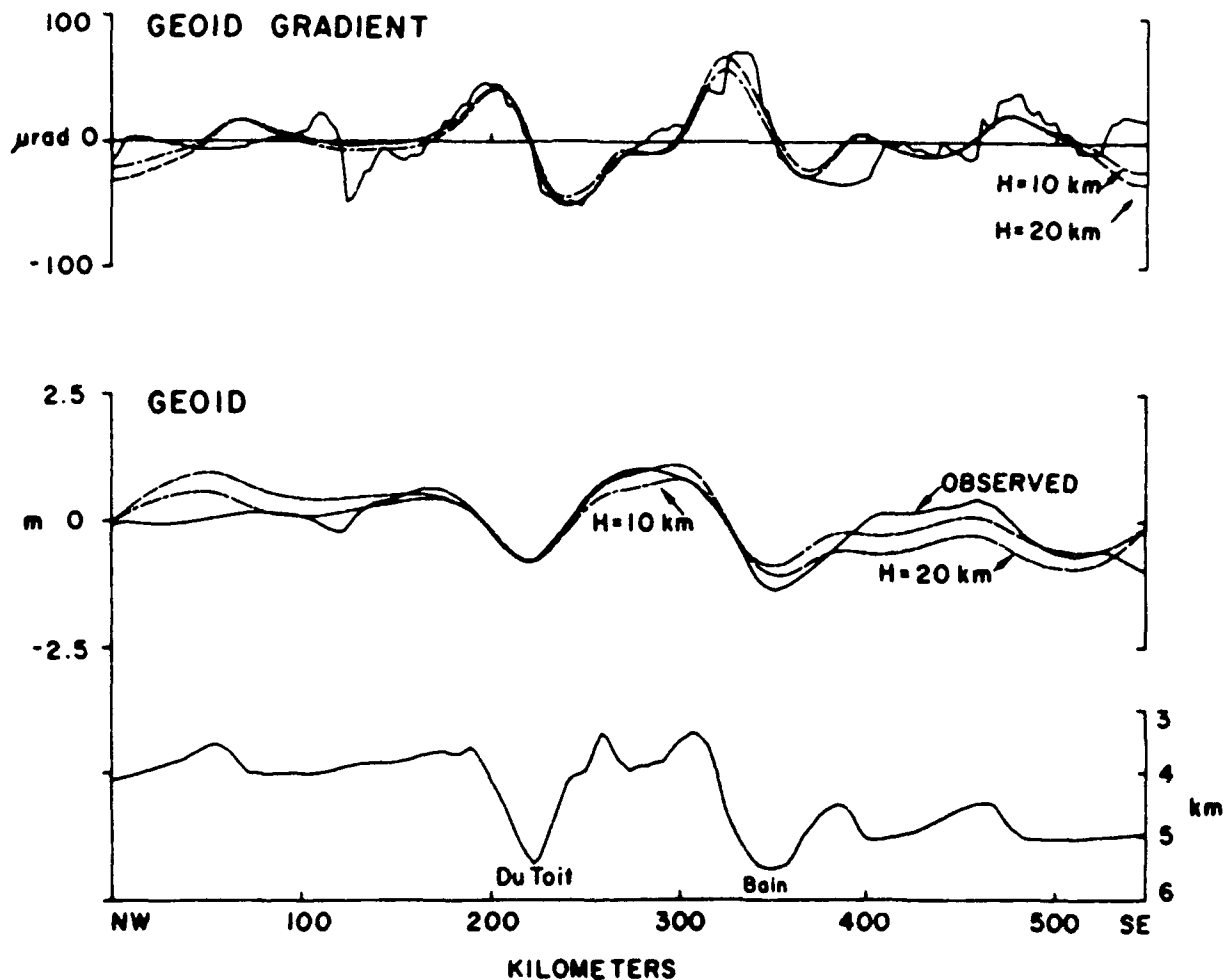


Figure 17. Bathymetry and geoid heights across the Du Toit and Bain

Fracture Zones (Figure 8: profile 2). Observed geoid heights (solid line) have a 225 km running mean removed. Dashed lines are geoid and geoid gradients calculated using a thin-elastic plate compensation model. Calculated profiles for plate thicknesses of 10 and 20 km are shown.

The anomalies could, therefore, be used to calculate both instantaneous and finite poles of rotation assuming there are independent age data. The anomaly trends can also be used to test previously-calculated poles of rotation. The distance to which the anomalies can be followed away from the spreading ridge generally increases with an increase in the age offset across the fracture zone. In this study area lineated anomalies can in some places be followed onto 80 my-old seafloor.

Previous studies of fracture zones have indicated that within the active transform zone movement between the two plates takes place along a narrow ( $\sim 4$  km) zone of shear aligned along the deepest part of the fracture zone trough (e.g., Otter, 1985). If the geoid anomaly were simply a result of the thermal contrast, the maximum or minimum gradient anomaly would overlie the deepest part of the fracture zone, which is not usually seen. To identify possible causes for this discrepancy we investigated the effects of the thermal structure and topography on the geoid anomaly. The intermediate-wavelength geoid anomaly predicted from the difference in thermal structure across the fracture zone agrees well with the observed anomaly. The gradient of this calculated anomaly, however, is much smoother than the observed gradient and the gradient peaks are offset by 10-20 km. The geoid calculated by assuming the topography is compensated by flexure of a thin-elastic plate agrees more closely with the shorter-wavelength anomalies ( $\lambda \leq 225$  km) of the observed geoid and with the geoid gradient. When both the seafloor topography and the thermal variations are modeled, the gradient anomalies are well matched and the data does not require the position of the thermal contrast beneath the fracture zone to be shifted outside the deep fracture zone axis. The observed geoid gradient cannot be analyzed solely in terms of the thermal

edge effect, but must be viewed as a combination of both the thermal anomaly and the fracture zone topography.

#### Acknowledgments:

We thank Dan McKenzie, Steve Daly and Linda Meinke for their contributions to the programs used to display the altimeter data. Philippe Patriat and Jacques Segoufin generously provided bathymetry along Marion Dufresne-34 lines. Kelly Luetkemeyer at Woods Hole Oceanographic Institution introduced us to the IDIMS image processing software package and his generous help and enthusiasm are greatly appreciated. This research was supported at MIT by ONR contract N00014-80-C-0273 and Univ. of Texas at Austin subcontract NSF DPP-8405968. The most recent bathymetry data were collected during the 1983-84 PROTEA expedition (R/V Melville ,(SIO)) which was supported by NSF grant OCE81-17702 with Scripps Institution of Oceanography.



TABLE 1

<u>Parameter</u>	<u>Definition</u>	<u>Value</u>
$\alpha$	thermal expansion coefficient	$3.0 \times 10^{-5} \text{ K}^{-1}$
$d_{\text{ref}}$	ridge crest depth	2100 m
$g$	acceleration of gravity	$9.80 \text{ m s}^{-2}$
$G$	gravitational constant	$6.67 \times 10^{-11} \text{ N m}^2 \text{ kg}^{-2}$
$\kappa$	thermal diffusivity	$8 \times 10^{-7} \text{ m}^2 \text{ s}^{-1}$
$\rho_m$	mantle density	$3330 \text{ kg m}^{-3}$
$\rho_w$	seawater density	$1025 \text{ kg m}^{-3}$
$T_m$	mantle temperature	$1365 \text{ }^\circ\text{C}$

## Appendix:

To determine the temperature structure across two fracture zones the two-dimensional heat-conduction equation must be solved. The solution to the equation

$$\frac{\partial^2 T}{\partial x^2} + \frac{\partial^2 T}{\partial z^2} = \frac{1}{\kappa} \frac{\partial T}{\partial t} \quad (A1)$$

can be expressed as a Green's function solution (Carslaw and Jaeger, 1959) where:

$$T(x, z, t) = \int_0^\infty \int_{-\infty}^\infty g(x-x_0, z-z_0, t-t_1) T(x_0, z_0, t_1) dx_0 dz_0 \quad (A2)$$

$T(x_0, z_0, t_1)$  is the initial condition at time  $t_1$  and the Green's function  $g(x-x_0, z-z_0, t-t_1)$  is given by:

$$g(x-x_0, z-z_0, t-t_1) = \frac{1}{4\pi\kappa(t-t_1)} \left\{ \exp\left[-((x-x_0)^2 + (z-z_0)^2)/4\kappa(t-t_1)\right] + \exp\left[-((x-x_0)^2 + (z+z_0)^2)/4\kappa(t-t_1)\right] \right\} \quad (A3)$$

The initial temperature structure for  $x < x_2$  is the solution to the two-dimensional heat-conduction equation which includes vertical cooling and lateral cooling across a fracture zone located at  $x = x_1$  (Sandwell and Schubert, 1982). The initial temperature for  $x > x_2$  is a constant,  $T_m$  (see Figure 10, this paper).

$$T(x_0, z_0, t_1) = \frac{T_m}{2} \left[ \operatorname{erfc} \frac{x_0 - x_1}{2\sqrt{\kappa t_1}} \operatorname{erf} \frac{z_0}{2\sqrt{\kappa t_0}} + \operatorname{erfc} \frac{-(x_0 - x_1)}{2\sqrt{\kappa t_1}} \operatorname{erf} \frac{z_0}{2\sqrt{\kappa t_1}} \right] \quad \begin{matrix} -\infty < x_0 < x_2 \\ x_2 < x_0 < \infty \end{matrix} \quad (A4)$$

The boundary condition is

$$T(x, 0, t) = T_S = 0^\circ\text{C} \quad (\text{A5})$$

The solution is obtained by inserting A3 and A4 into A2 and solving the integral. Because of its complexity, one term of the solution is left in integral form and is solved numerically. The final temperature distribution is given by:

$$\begin{aligned} T(x, z, t) = & \frac{T_m}{2} \left[ \frac{1}{2} \left( \operatorname{erf} \frac{z}{2\sqrt{k(t+t_0-t_1)}} + \operatorname{erf} \frac{z}{2\sqrt{kt}} \right) \operatorname{erfc} \frac{x-x_2}{2\sqrt{k(t-t_1)}} \right. \\ & + \left( \operatorname{erf} \frac{z}{2\sqrt{kt}} - \operatorname{erf} \frac{z}{2\sqrt{k(t+t_0-t_1)}} \right) \int_{-\infty}^{x_2} \frac{1}{2\sqrt{\pi k(t-t_1)}} \operatorname{erf} \frac{x_0-x_1}{2\sqrt{kt_1}} \\ & \left. e^{\frac{-(x-x_0)^2}{4k(t-t_1)}} dx_0 + \operatorname{erfc} \frac{-(x-x_2)}{2\sqrt{k(t-t_1)}} \operatorname{erf} \frac{z}{2\sqrt{k(t-t_1)}} \right] \end{aligned}$$

## References

- Barrett, D.M., 1977. The Agulhas Plateau: a marine geophysical study, Bull. Geol. Soc. America, 88, 749-763.
- Bergh, H.W., 1977. Mesozoic sea floor off Dronning Maud Land, Antarctica, Nature, 269, 686-687.
- Bergh, H.W. and I.O. Norton, 1976. Prince Edward Fracture Zone and the evolution of the Mozambique Basin, J. Geophys. Res., 81, 5221-5239.
- Born, G.H., J.A. Dunne, D.B. Lame, 1979. Seasat mission overview, Science, 204, 1405-1406.
- Briggs, I.C., 1974. Machine contouring using minimum curvature, Geophysics, 39, 39-48.
- Carslaw, H.S. and J.C. Jaeger, 1959. Conduction of heat in solids, Oxford University Press, New York, 519 pp.
- Detrick, R.S. Jr., 1981. An analysis of geoid anomalies over the Mendocino fracture: implications for thermal models of the lithosphere, J. Geophys. Res., 86, 11751-11762.
- Dixon, T.H., M. Naraghi, M.K. McNutt, and S.M. Smith, 1983. Bathymetric prediction from SEASAT altimeter data, J. Geophys. Res., 88, 1563-1571.
- Dixon, T.H. and M.E. Parke, 1983. Bathymetry estimates in the southern oceans from Seasat altimetry, Nature, 304, 406-411.
- Dorman, L.M., 1975. The gravitational edge effect, J. Geophys. Res., 80, 2949-2950.
- Fisher, R.L. and J.G. Sclater, 1983. Tectonic evolution of the Southwest Indian Ocean since the Mid-Cretaceous: plate motions and stability of the pole of Antarctica/Africa for at least 80 Myr, Geophys. J. R. astr. Soc., 73, 553-576.

- Freedman, A.P. and B. Parsons, 1986. Seasat-derived gravity over the Musicians Seamounts, J. Geophys. Res., 91, 8325-8340.
- Girod, M. and J. Nougier, 1971. Volcanism of the Sub-Atlantic Islands, in Antarctic Geology and Geophysics, pp. 777-788, ed. R.J. Adie, Universitetsforlaget, Oslo.
- Goslin, J., 1981. Étude géophysique des reliefs asismique de l'océan Indien occidental et austral, Unpub. D.Sc. thesis, Université Louis Pasteur de Strasbourg, 267 p.
- Goslin, J., M. Recq, and R. Schlich, 1981. Structure profonde du plateau de Madagascar: Relations avec le plateau de Crozet, Tectonophysics, 74, 75-97.
- Haxby, W.F., G.D. Karner, J.L. LaBreque, J.K. Weissel, 1983. Digital images of combined oceanic and continental data sets and their use in tectonic studies, Eos Trans. AGU, 64, 995-1004.
- Haxby, W.F. and D.L. Turcotte, 1978. On isostatic geoid anomalies, J. Geophys. Res., 83, 5473-5478.
- Hayes, D.E. and M. Vogel, 1981. 5.13: the Indian Ocean south of 46.5°S, General Bathymetric Chart of the Oceans (GEBCO), Canadian Hydrographic Service, Ottawa.
- Heezen, B.C. and M. Tharp, 1965. Descriptive sheet to accompany the physio-graphic diagram of the Indian Ocean, Geological Society of America, Inc., New York.
- Lambeck, K. and R. Coleman, 1982. A search for seamounts on the southern Cook and Austral region, Geophys. Res. Lett., 9, 389-392.
- Lazarewicz, A.R. and D.C. Schwank, 1982. Detection of uncharted seamounts using satellite altimetry, Geophys. Res. Lett., 9, 385-388.

- Louden, K.E. and D.W. Forsyth, 1976. Thermal conduction across fracture zones and the gravitational edge effect, J. Geophys. Res., 81, 4869-4874.
- Louden, K.E. and D.W. Forsyth, 1982. Crustal structure and isostatic compensation near the Kane Fracture Zone from topography and gravity measurements - I. Spectral analysis approach, Geophys. J. R. astr. Soc., 68, 725-750.
- OTTER, 1985. The geology of the Oceanographer transform: the transform domain, in press, Mar. Geophys. Res.
- Parmentier, E.M. and W.F. Haxby, 1986, Thermal stresses in the oceanic lithosphere: evidence from geoid anomalies at fracture zones, J. Geophys. Res., in press.
- Parsons, B. and F.M. Richter, 1980. A relation between the driving force and geoid anomaly associated with mid-ocean ridges, Earth Planet. Sci. Lett., 51, 445-450.
- Rabinowitz, P.D. and J. LaBrecque, 1979. The Mesozoic South Atlantic Ocean and evolution of its continental margins, J. Geophys. Res., 84, 5973-6002.
- Rapp, R.H., 1982. A summary of the results from the OSU analysis of Seasat altimeter data, Rep. No. 335 of the Dept. of Geodetic Science and Surveying.
- Sailor, R.V. and E.A. Okal, 1983. Applications of SEASAT altimeter data in seismotectonic studies of the south-central Pacific, J. Geophys. Res., 88, 1572-1580.
- Sandwell, D.T., 1984a. Thermomechanical evolution of oceanic fracture zones, J. Geophys. Res., 89, 11, 401-11,413.

- Sandwell, D.T., 1984b. A detailed view of the south Pacific geoid from satellite altimetry, J. Geophys. Res., 89, 1089-1104.
- Sandwell, D.T., 1984c. Along-track deflection of the vertical from SEASAT -GEBCO overlays. NOAA Tech. Memo. NOS NPS-40.
- Sandwell, D.T. and G. Schubert, 1980. Geoid height versus age for symmetric spreading ridges, J. Geophys. Res., 85, 7235-7241.
- Sandwell, D.T. and G. Schubert, 1982. Geoid height-age relation from SEASAT altimeter profiles across the Mendocino Fracture Zone, J. Geophys. Res., 87, 3949-3958.
- Schlich, R., 1982. Structure and age of the western Indian Ocean - Results of deep sea drilling, in Antarctic Geoscience, ed. Campbell Craddock, Univ. of Wisconsin Press: Madison, Wisconsin.
- Sclater, J.G., R.L. Fisher, P. Patriat, C. Tapscott, and B. Parsons, 1981. Eocene to recent development of the Southwest Indian Ridge, a consequence of the evolution of the Indian Ocean triple junction, Geophys. J. R. astr. Soc., 64, 587-604.
- Simson, E.S.W., J.G. Sclater, B. Parsons, I. Norton and L. Meinke, 1979. Mesozoic magnetic lineations in the Mozambique Basin, Earth Planet. Sci. Lett., 43, 260-264.
- Swain, C.J., 1976. A Fortran IV program for interpolating irregularly spaced data using the difference equations for minimum curvature, Computers & Geosciences, 1, 231-240.
- Tucholke, B.E., R.E. Houtz, and D.M. Barrett, 1981. Continental crust beneath the Agulhas Plateau, Southwest Indian Ocean, J. Geophys. Res., 86, 3791-3806.

- Verwoerd, W.J., 1971. Geology, in Marion and Prince Edward Islands, pp. 40-62, eds. van Zinderen Bakker, E.M. (Sr.), Winterbottom, J.B., and Dyer, R.D., A.A. Balkema, Cape Town.
- Vogt, P.R., B. Zondek, P.W. Fell, N.Z. Cherkis, and R.K. Perry, 1984. Seasat altimetry, the North Atlantic geoid, and evaluation by shipborne subsatellite profiles, J. Geophys. Res., 89, 9885-9903.
- Watts, A.B., J.R. Cochran, P. Patriat and M. Doucoure, 1985. A bathymetry and altimetry profile across the Southwest Indian Ridge crest at 31°S latitude, Earth Planet. Sci. Lett., 73, 129-139.
- Watts, A. B., 1979. On geoid heights derived from GEOS3 altimeter data along the Hawaiian-Emperor Seamount chain, J. Geophys. Res., 84, 3817-3826.



Chapter 3. Eocene to present-day plate motions at the  
Southwest Indian Ridge

## INTRODUCTION

The primary elements in the tectonic evolution of many ocean basins are now well-documented. Researchers have analyzed bathymetric, teleseismic and magnetic data to locate present and past plate boundaries and have constructed tectonic histories from these data. The plate motions are successively refined and reinterpreted as additional geophysical information becomes available and more sophisticated methods of analysis are developed. Such studies are valuable for testing certain aspects of plate tectonics on an increasingly finer scale. Additionally, the refined rotation parameters can be combined with fewer accumulated errors and can then be used to determine more accurately the relative motions between plates such as the Pacific and North American plates that share little or no divergent boundaries. Because the African and Antarctic plates share common boundaries with six of the major plates, accurate poles of rotation for the motion between Africa and Antarctica are important to many studies combining plate rotations.

In this study, fracture zone crossings on the African and Antarctic plates are compiled from altimeter profiles and bathymetric charts and used to augment the existing magnetic and bathymetric data. These data are used to determine a present-day pole of rotation and three finite rotation poles for the times of magnetic anomalies 6( 20 Ma), 13( 37 Ma) and 20( 45 Ma) which are found to be located reasonably close to previously published poles based on smaller data sets.

The instantaneous motion between Africa and Antarctica has been derived in previous studies using several different methods and various combinations and quantities of angular rotation rates, earthquake slip vectors and transform fault trends. These poles are listed in Table 1

and plotted in Figure 1. The initial pole determinations (McKenzie and Sclater, 1971; Chase, 1972; Minster et al., 1974; Forsyth, 1975 and Forsyth reported in Sclater et al., 1976) are scattered and primarily reflect inadequate data constraints. Minster and Jordan's (1978) pole derived using a global inversion model compensated for the relative lack of data at the spreading ridge by using slip vectors, spreading rates and transform fault azimuths from all the major plate boundaries. Their pole for African-Antarctic plate motion (RM2 pole) is very close to more recent poles which are based mainly on transform azimuths (Sclater et al., 1981; Tapscott et al., 1980), which place the tightest constraints on the location of the pole of rotation. In the present study 14 azimuths (5 more than used in Sclater et al., 1981) define a pole at  $2.7^{\circ}$  N,  $36.7^{\circ}$ W. This pole falls within the 90% confidence ellipse of the Sclater et al. (1981) pole and within one standard deviation of the RM2 pole obtained by Minster and Jordan (1978).

Original reconstructions of the Indian Ocean by McKenzie and Sclater (1971), Sclater and Fisher (1974) and Norton and Sclater (1979) clarified the pattern of breakup and separation of the Indian, African and Antarctic plates. More accurate poles describing the development of the Southwest Indian Ocean during the Cretaceous to the present have since been determined (Sclater et al., 1981; Fisher and Sclater, 1983; Patriat, 1983; Patriat et al., 1985; Molnar and Stock, 1987 in preparation). One major result of Fisher and Sclater (1983) is the apparent stability of the pole of rotation for the past 80 Myr. This conflicts with the findings of Patriat (1983) and Patriat et al. (1985), who suggest that a major plate reorganization occurred somewhere between the times of magnetic anomalies 32 (74 Ma) and 24 (56 Ma). In this

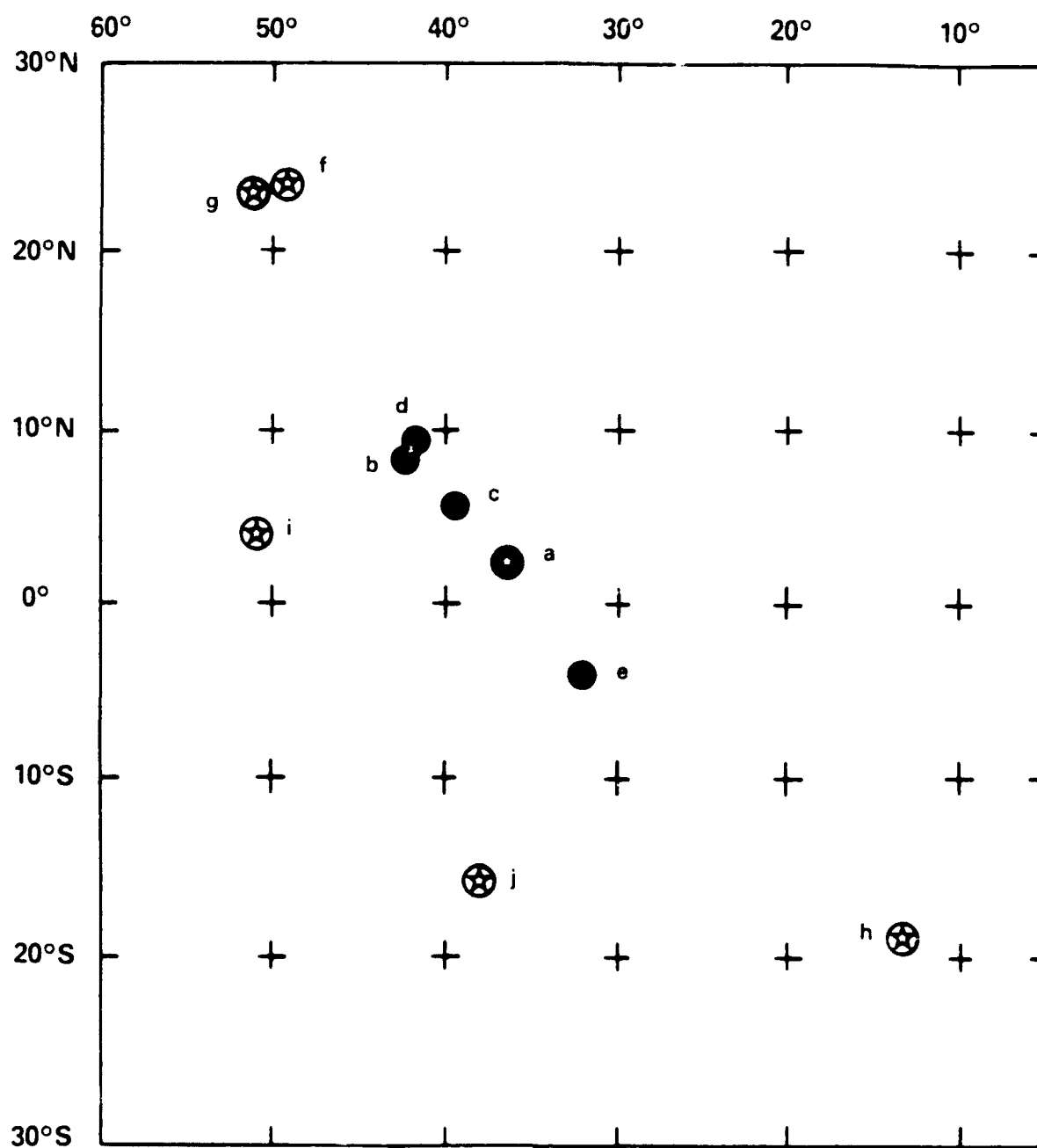


Figure 1 Locations of instantaneous poles of rotation from this study (circled star) and previous studies (listed in Table 1). Unfilled symbols are poles determined before 1975, filled symbols are poles based on larger data sets available after 1975.

study, the directions of motion recorded by fracture zone traces are consistent with the stability of the pole for at least the past 47 Myr. The two youngest finite rotation poles determined here for magnetic anomalies 6 and 13 are similar to those reported in Fisher and Sclater (1983). The older pole at anomaly 20 predicts a plate rotation significantly different from that found by Fisher and Sclater (1983) and is located near the anomaly 24 pole found by Patriat (1983). For older seafloor we were not able to determine a sufficient amount of new fracture zone information to warrant a revised reconstruction. The altimeter profiles, however, are searched for evidence of fracture zone trends which either continue their present orientations or swing around to the new orientation dictated by the proposed change in plate motion. (The results of this search are described in the discussion).

The remaining sections of this paper focus on the tectonic nature of the spreading ridge, the determination of fracture zone crossings from altimeter data, and the calculation of the instantaneous and finite rotation poles.

#### THE AFRICAN-ANTARCTIC PLATE BOUNDARY--PAST AND PRESENT

The African and Antarctic plates are bounded by a spreading ridge that extends from the Bouvet Triple Junction in the South Atlantic ( $54^{\circ} 50'S$ ,  $0^{\circ}40' W$ ) to the Indian Ocean Triple Junction at  $25^{\circ}S$ ,  $70^{\circ}E$  (Figure 2). The half-spreading rate is about 0.8 cm/yr and the morphology of the ocean basin is extremely rough which is typical of seafloor formed at slow-spreading ridges.

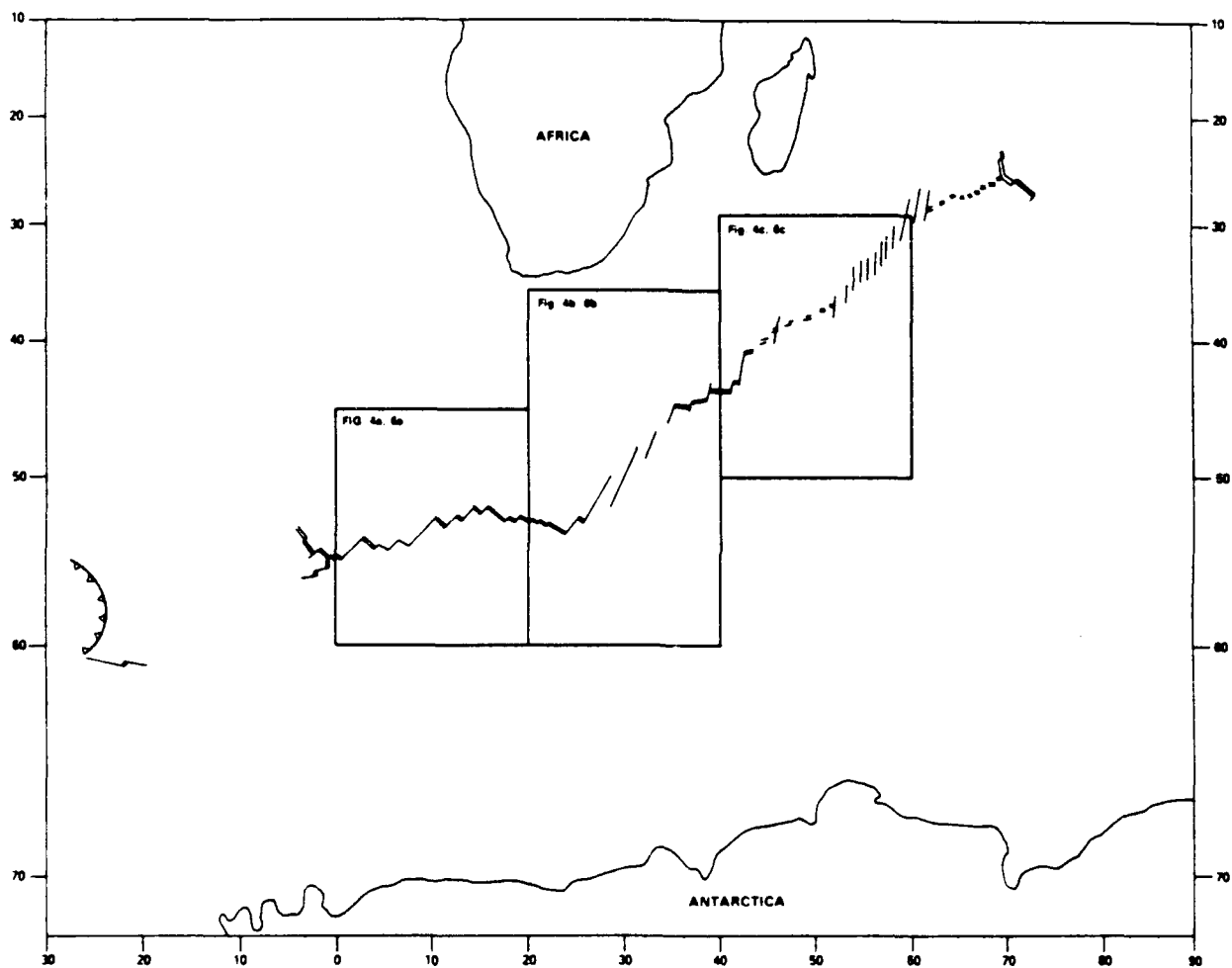


Figure 2 Location of the Southwest Indian Ocean Ridge.

Fracture zones intersect the ridge axis approximately every 80-100 km. Several of the fracture zones, notably the Bain, Prince Edward and Discovery II Fracture Zones are composed of two or more closely spaced transform valleys. Bergh and Norton (1976) suggest that slight changes in the pole of rotation may have caused the development of the two transform valleys at the Prince Edward Fracture Zone.

#### Magnetic Anomalies:

Because of the slow spreading rate and rough morphology, magnetic profiles are difficult to interpret and the relative sparseness of magnetic anomaly identifications has made reconstructions of this ocean particularly difficult. Magnetic anomaly identifications used in this paper were provided by Molnar and Stock (1987, in preparation) who reanalyzed published magnetic profiles. For anomaly 6, three pairs of magnetic lineations are obtained from magnetic profiles published in Patriat (1983). For anomaly 13, profiles from Bergh and Norton (1976), Patriat (1983) and Patriat et al. (1985) provide identifications for 3 lineation pairs, and for anomaly 20, 4 pairs of lineations are determined from profiles in Patriat (1983), Patriat et al. (1985) and Fisher and Sclater (1983).

#### Fracture Zones:

The close spacing of fracture zones and relatively large distances between ship tracks have made it difficult to correlate fracture zone crossings between bathymetric profiles. Consequently, few of the fracture zones are well-sampled along their entire lengths, particularly

south of the spreading ridge. The mapping of fracture zone traces is improved here by analyzing Seasat altimeter profiles. The satellite tracks provide fairly uniform coverage in the Southwest Indian Ocean (Figure 3). Driscoll et al. (1987) show that fracture zones along this spreading ridge appear as local depressions in the altimeter profiles superimposed on an intermediate-wavelength step. Spreading ridge segments appear in the altimeter profiles as local maxima with depressions directly over the median valleys (Watts et al., 1986). Using our current knowledge of the bathymetry and evidence of the active plate boundary from the pattern of seismicity, spreading ridge segments and fracture zone crossings are identified along each altimeter profile. A map summarizing this compilation is shown in Figures 4a, 4b and 4c.

Several difficulties were encountered in identifying the fracture zone and ridge crest crossings. The angle at which a track crosses a feature is crucial to the accuracy of the identification. Ideally, tracks should be perpendicular to the trend of the fracture zone or ridge segment so that the lateral extent of the feature in the profile is minimized. The ascending satellite tracks (tracks approaching from the southeast and ascending in latitude to the northwest) cross the fracture zones west of Discovery II Fracture Zone at a fairly high angle. East of this, however, the fracture zones trend north-south and the crossing angle is closer to  $45^\circ$  which makes the identification of fracture zone crossings difficult. The descending tracks are almost parallel to the western fracture zones rendering them useless for identifying fracture zones but ideal for locating ridge segments. An additional criterion for a positive identification is that the feature



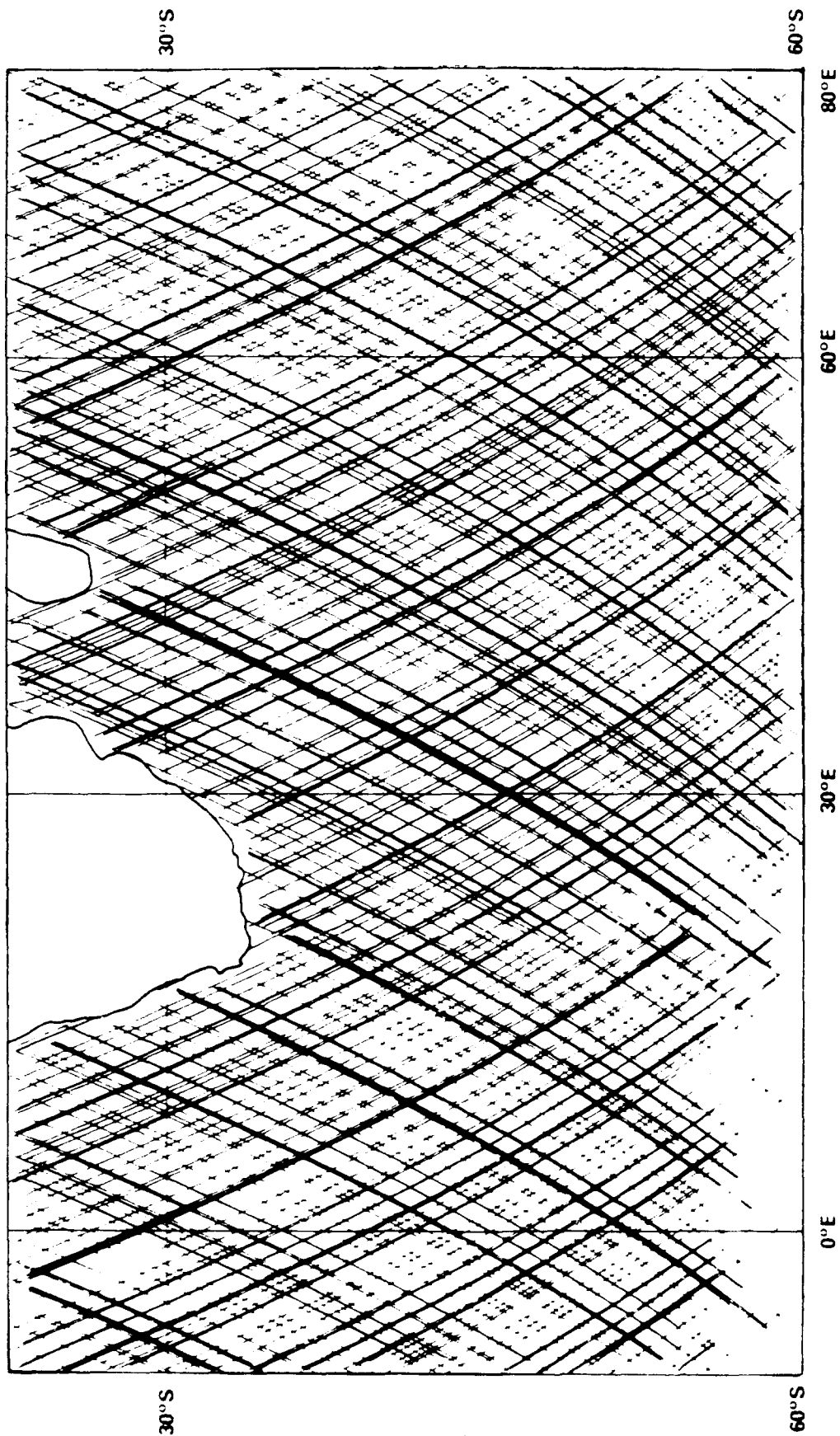


Figure 3 Track chart for Seasat satellite passes. Ascending tracks approach from the southeast and gain in latitude towards the northwest. Descending tracks approach from the northeast and descend in latitude towards the southwest.

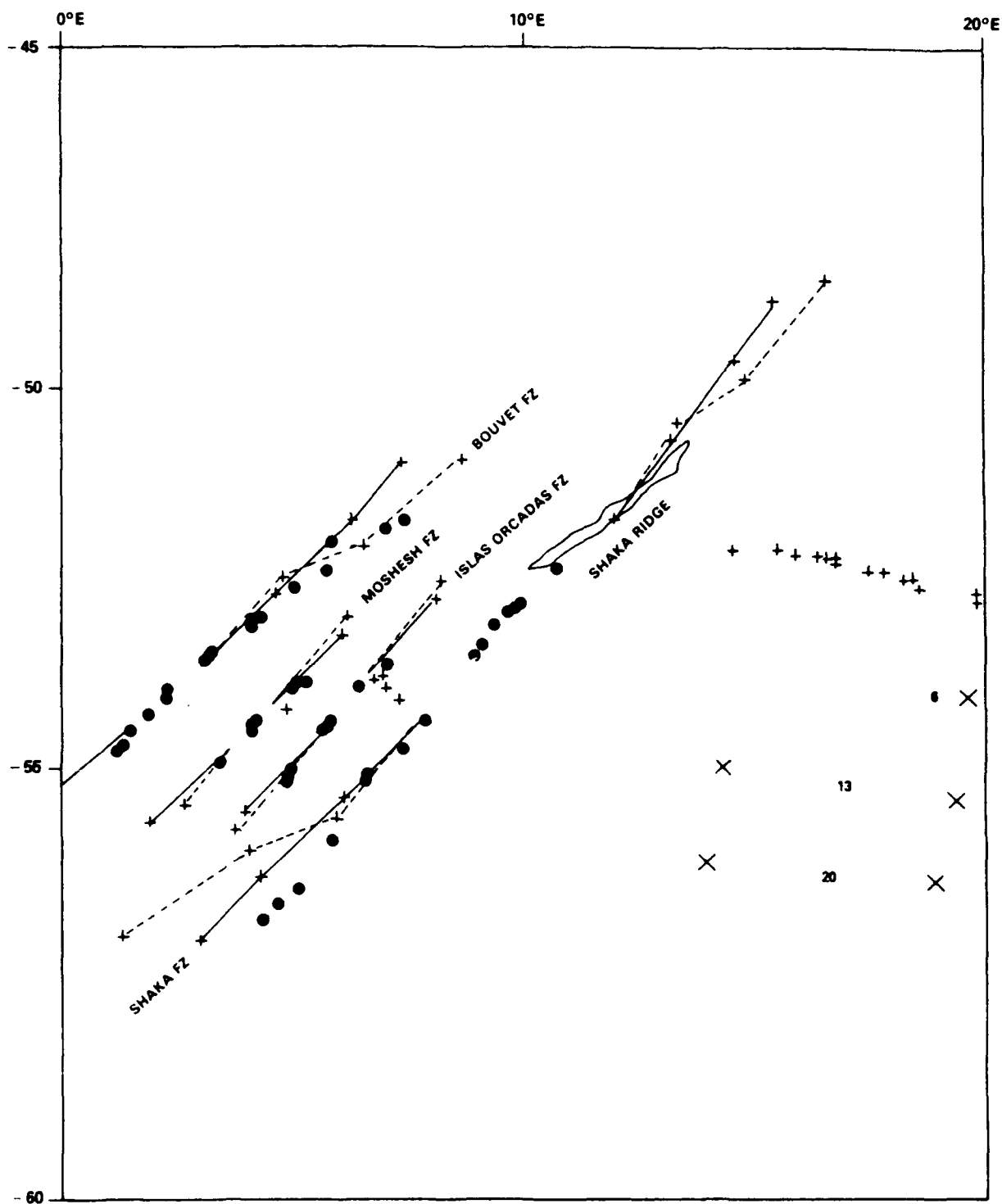


Figure 4a Ridge crest crossings from altimetry (+ on figure), fracture zone crossings from altimetry (●) and bathymetry (o), and magnetic anomaly identifications (x). Flowlines are calculated from poles of rotation determined in this paper (solid lines), in Fisher and Sclater, 1983 (dashed lines) and Patriat, 1983; Patriat et al., 1985 (dotted lines).

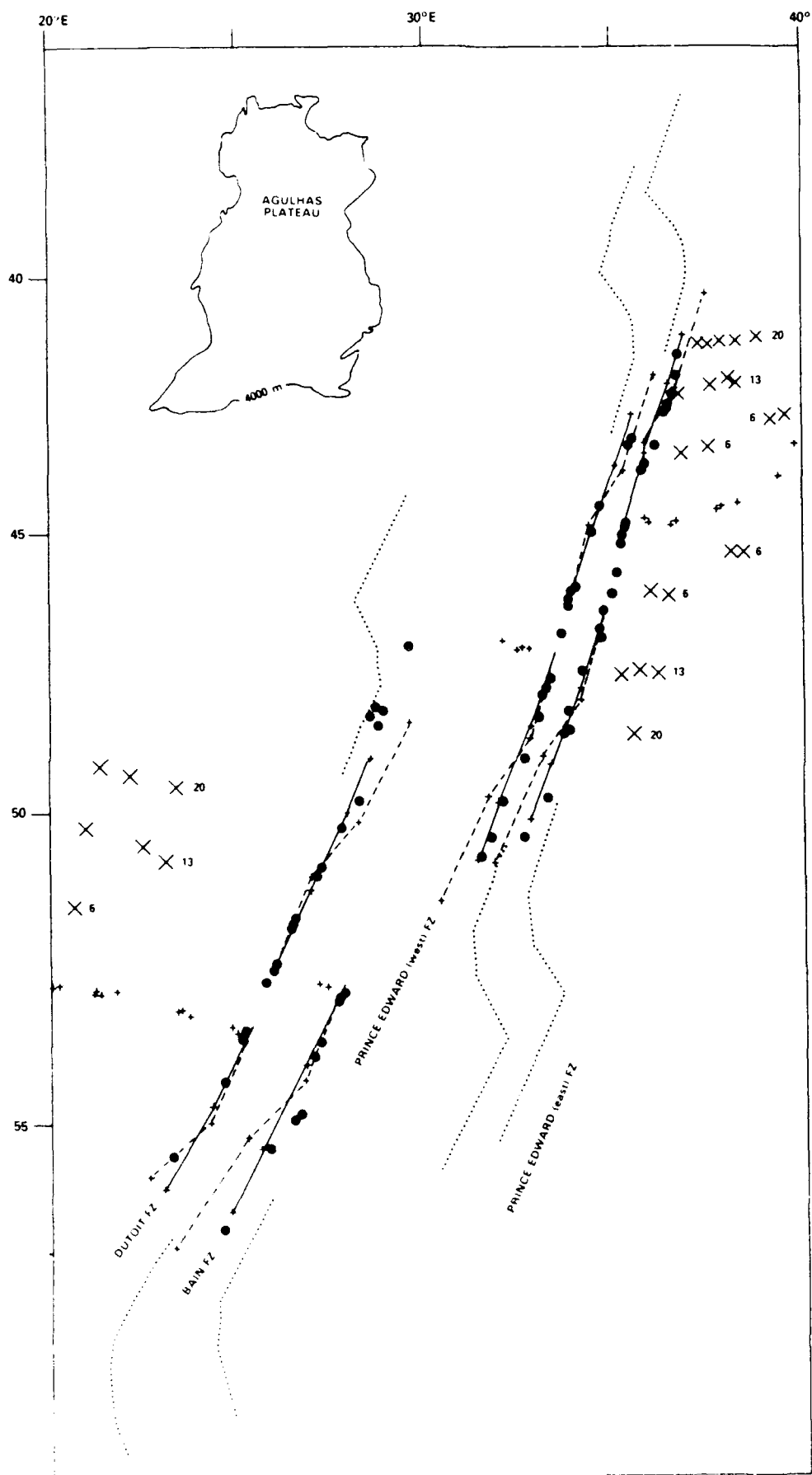


Figure 4b (same as Figure 4a)

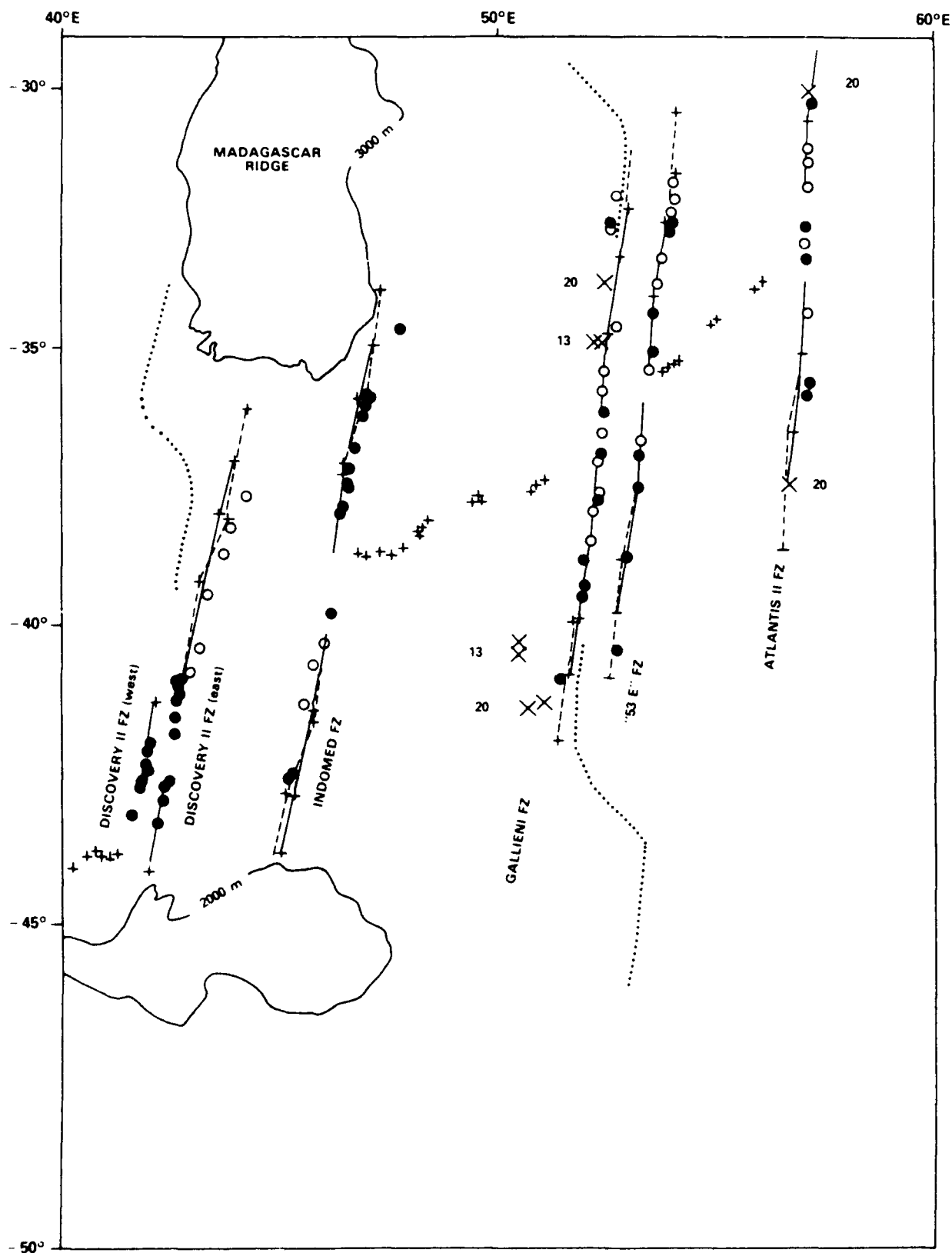


Figure 4c (same as Figure 4a)

must be correlated between successive track lines or line up with a known bathymetric feature.

The extent of the identifications north and south of the ridge crest is limited to seafloor younger than about 50 Myr. The fracture zone signals in altimeter profiles across older seafloor become indistinct and may indicate either a rapid disappearance of the underlying topographic expression of the fracture zones, or a change in fracture zone orientation such that the profiles no longer cross features at an optimum angle for detection. Supporting the first hypothesis is the decrease in spreading rate after anomaly 28 from 3.25 cm/yr to the present rate of 0.8 cm/yr (Fisher and Sclater, 1983). At faster spreading rates fracture zone morphology becomes more subdued and the local depression in the geoid (which is the combined effect of both the topography and its compensation) would also be subdued. In addition, the second hypothesis may also be valid although it is difficult to test because of the limits imposed on a search for new fracture zone orientations by the track spacings and orientations and also because, again, the faster spreading rate may have produced subdued fracture zone traces.

Additional fracture zone crossings were digitized from bathymetric charts presented in Fisher and Sclater (1983) and Driscoll et al. (1987). These fracture zone identifications are made only where ship tracks cross the trace and are used (when available) to fill in the holes between satellite tracks or where the fracture zone signal is unclear.

A location error was estimated for each fracture zone crossing for use as a weighting function in determining rotation poles. For the

digitized bathymetric crossings an error of 30 km was used which was chosen to reflect possible errors in digitizing and the use of an interpretive contour map (rather than the original bathymetric profiles) to estimate the deepest part of the fracture zone valley. (It is this deepest point that we assume we are locating in the altimeter profiles.) For the altimeter crossings an error of 15 km was estimated. The data points along the profiles are about 7 km apart and frequently the local minimum was V-shaped which allows a very accurate location to be made. Other local minima were more U-shaped. On these the center was chosen as the fracture zone crossing and an error of 15 km represents the possibility of the deepest part of the fracture zone being  $\pm 2$  data points from the center of the anomaly.

#### PRESENT-DAY POLE OF ROTATION

Three or more crossings of the active transform sections of 11 fracture zones are used to determine the directions of instantaneous relative motion between Africa and Antarctica. The azimuth at Bain Fracture Zone is determined from fracture zone crossings near its southern ridge-transform intersection where the fault is known from seismicity to be active. Also used are the azimuths for fracture zone 'S' determined by Norton (1976) and those reported in Tapscott et al. (1980) for the Atlantis II, '58 E', and Melville Fracture Zones. The pole of rotation that minimizes the sum of the squared differences between observed and expected azimuths lies at  $0.5^{\circ}\text{N}$ ,  $35.12^{\circ}\text{W}$ . All observed azimuths are within  $5^{\circ}$  of the expected ones for this pole except for the azimuth at Indomed where there is a  $5.6^{\circ}$  difference. If Indomed is excluded, the best-fitting pole lies at  $2.7^{\circ}\text{N}$ ,  $36.7^{\circ}\text{W}$  and the

differences between observed and expected azimuths are all less than  $5^\circ$  (Table 2). For this reason, this second pole is preferred over the first and taken to represent the present-day plate motion.

Although new rate data have not been collected in this study, the rates published for the African-Antarctic plate boundary in Minster and Jordan (1978) are used to minimize the sum of the squared differences between the observed and expected velocities given the new pole position. For the pole at  $2.7^\circ\text{N}$   $36.7^\circ\text{W}$  this rate is  $0.152^\circ/\text{my}$ .

As previously noted in the introduction, this new pole is close to the instantaneous poles derived from smaller data sets with various criteria for goodness-of-fit (Table 1 and Figure 1). It is  $4^\circ$  from the pole derived by Tapscott et al. (1980) which is the best-fit solution for directions and rates across the common boundaries of the African, Indian, Antarctic and South American plate system. It is  $25^\circ$  from the poles calculated by minimizing directions and rates across the Antarctic, African and South American 3-plate system (Forsyth, 1975; Sclater et al., 1976). If only the westernmost 4 fracture zones in this study are used to calculate a best-fitting pole it lies at  $2.5^\circ\text{N}$ ,  $36.1^\circ\text{W}$ , almost identical in location to the best-fitting pole for the complete data set. The earthquake mechanisms (events 1 and 2 in Forsyth, 1975) and transform fault azimuths (Sclater et al., 1976) from these studies are consistent with the directions of motion used in this study, and the differences in pole position is likely caused by inadequate data constraints on the Antarctic-African plate boundary in their solution. Transform fault azimuths located along almost the entire length of the spreading ridge are consistent with a single instantaneous pole of motion.

## FINITE POLE FOR ANOMALIES 6 (20 Ma), 13 (37 Ma) AND 20 (45 Ma)

### METHOD

Finite poles of rotation are determined using Hellinger's (1981) method in which points representing the plate boundary on the Antarctic plate at a discrete time in the past are rotated back into coincidence with points on the African plate. Individual segments of the plate boundary represented by fracture zone traces and magnetic lineations are fit by great-circle arc segments, and the distances between data points and arc segments are minimized to find the best-fitting finite rotation pole and angle. Fossil transform fault and magnetic anomaly lineations and their errors used in this analysis are listed in Table 2 and plotted in Figures 4a, 4b and 4c.

### ANOMALY 6:

The best-fitting pole for anomaly 6 is at  $5.6^{\circ}\text{N}$ ,  $37.4^{\circ}\text{W}$  with a rotation angle of  $2.8^{\circ}$ . The error ellipse is elongated in a northwest-southeast direction and is fairly narrow (Figure 5a).

If deformation has not occurred at the fracture zones, then crossings on the Antarctic plate when rotated about the best-fitting pole should overlie fossil transform sections on the African plate. The pole for anomaly 6 is within about  $3^{\circ}$  of the present-day pole of rotation, and significant deformation related to a change in the direction of spreading is not expected. Rotated points at Bouvet, DuToit, Prince Edward (west and east transform valleys), Discovery II (east), Indomed, Gallieni, "53 E" and Atlantis II line up very well with



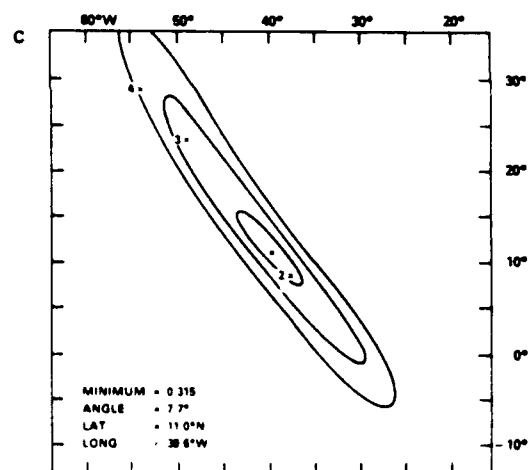
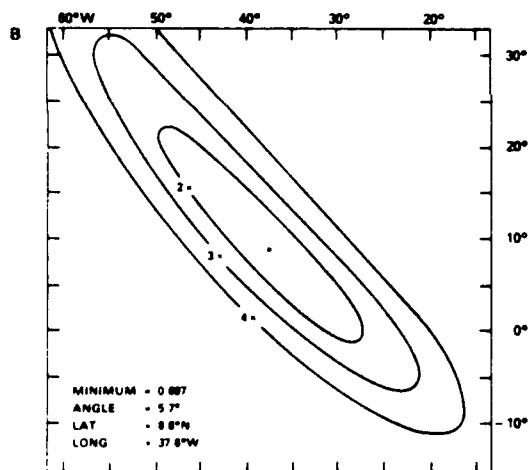
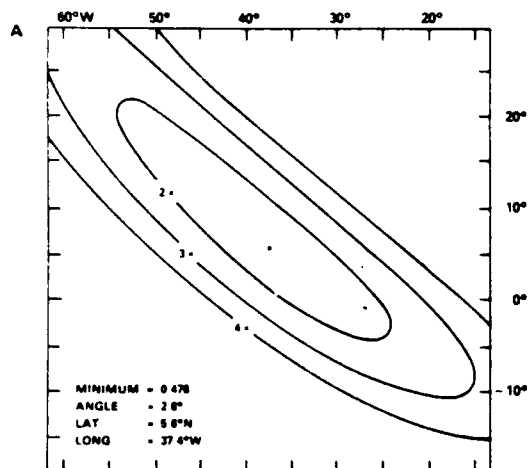


Figure 5 Contour plots of weighted errors for poles in the neighborhood of the best-fitting poles of rotation for 5a) anomaly 6; 5b) anomaly 13; 5c) anomaly 20.

fixed points and bathymetric trends (Figures 6a, 6b and 6c). There are few bathymetric data for the Moshesh and Islas Orcadas fracture zones but the rotated and fixed points define trends of around 40 which are consistent with those observed at Bouvet and Shaka Fracture Zones (Figure 6a).

Three magnetic lineations are used to constrain the pole of rotation and the quality of their reconstructions are variable. The reconstructions of the two lineations between Prince Edward and Discovery II Fracture Zones (Figure 6b) are not as good as expected given the exceptionally good reconstruction of the fracture zones, but are acceptable within the errors of 20 km assigned to these data points. Only one fixed and one rotated point are available to define a lineation west of DuToit Fracture Zone (Figure 6b). The two points overlie points from the present-day ridge crest that are rotated by half the total angle and the reconstruction of this lineation is considered to be good.

#### ANOMALY 13:

Four fracture zone segments and three magnetic lineations constrain the finite rotation pole for Anomaly 13. The best-fitting pole lies at  $8.8^{\circ}\text{N}$ ,  $37.6^{\circ}\text{W}$  with a total rotation angle of  $5.7^{\circ}$  (Figure 5b). This pole is only  $2.5^{\circ}$  away from the anomaly 6 pole. Rotated fracture zone crossings from the Antarctic plate at DuToit, Indomed and "53 E" are aligned with fixed African crossings. The alignment is not as good at Prince Edward (west and east) and Gallieni, but the rotated points are within 15-20 km of the fracture zone valley. Although they were not used in determining the rotation pole, the rotated points from the Antarctic side of Shaka Fracture Zone (Figure 6a) trend more northerly

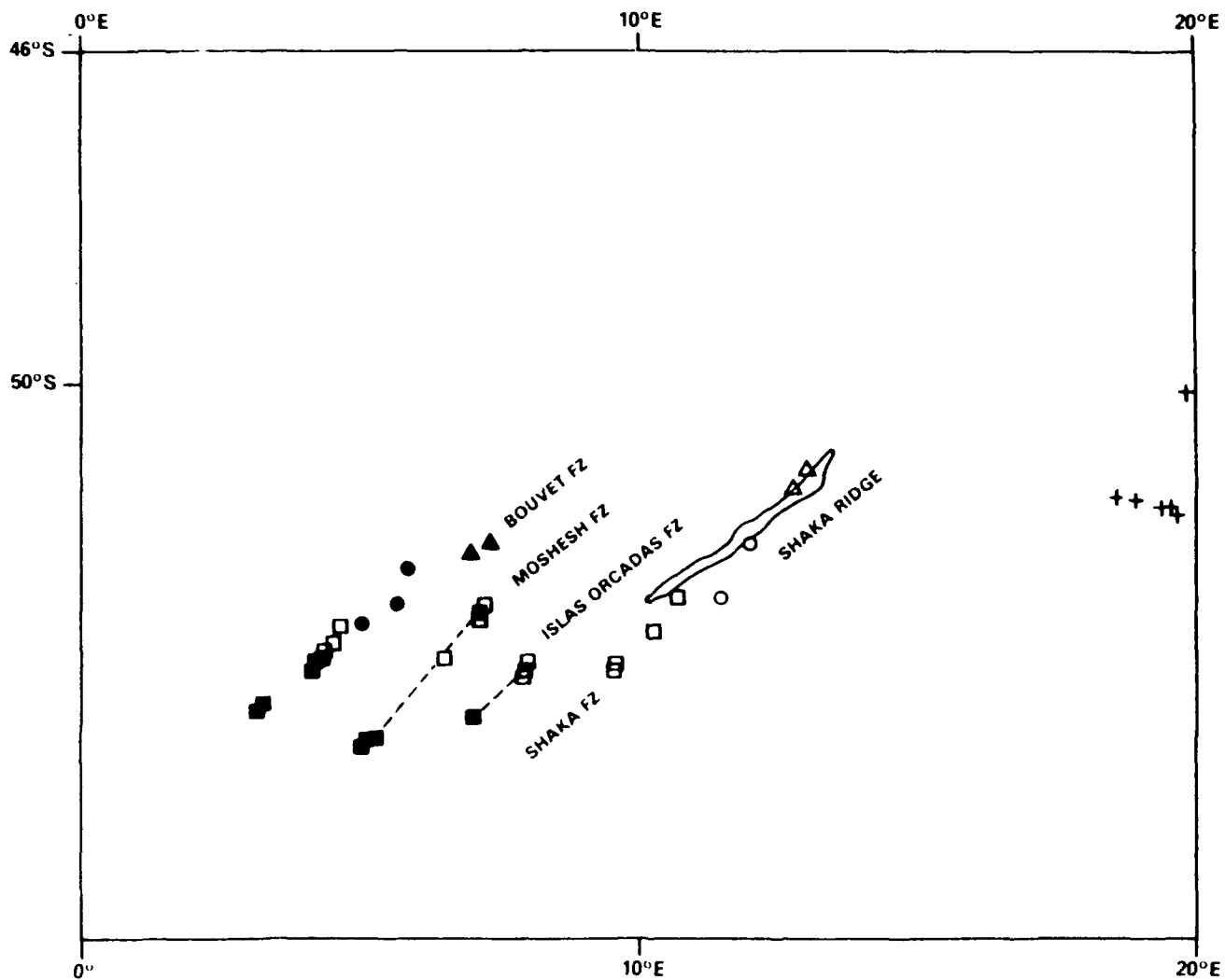


Figure 6a Reconstructions of magnetic lineations and fossil transform faults for anomalies 6 (squares), 13 (circles) and 20 (triangles). Open symbols are rotated points from the Antarctic plate, closed symbols are fixed points on the African plate.

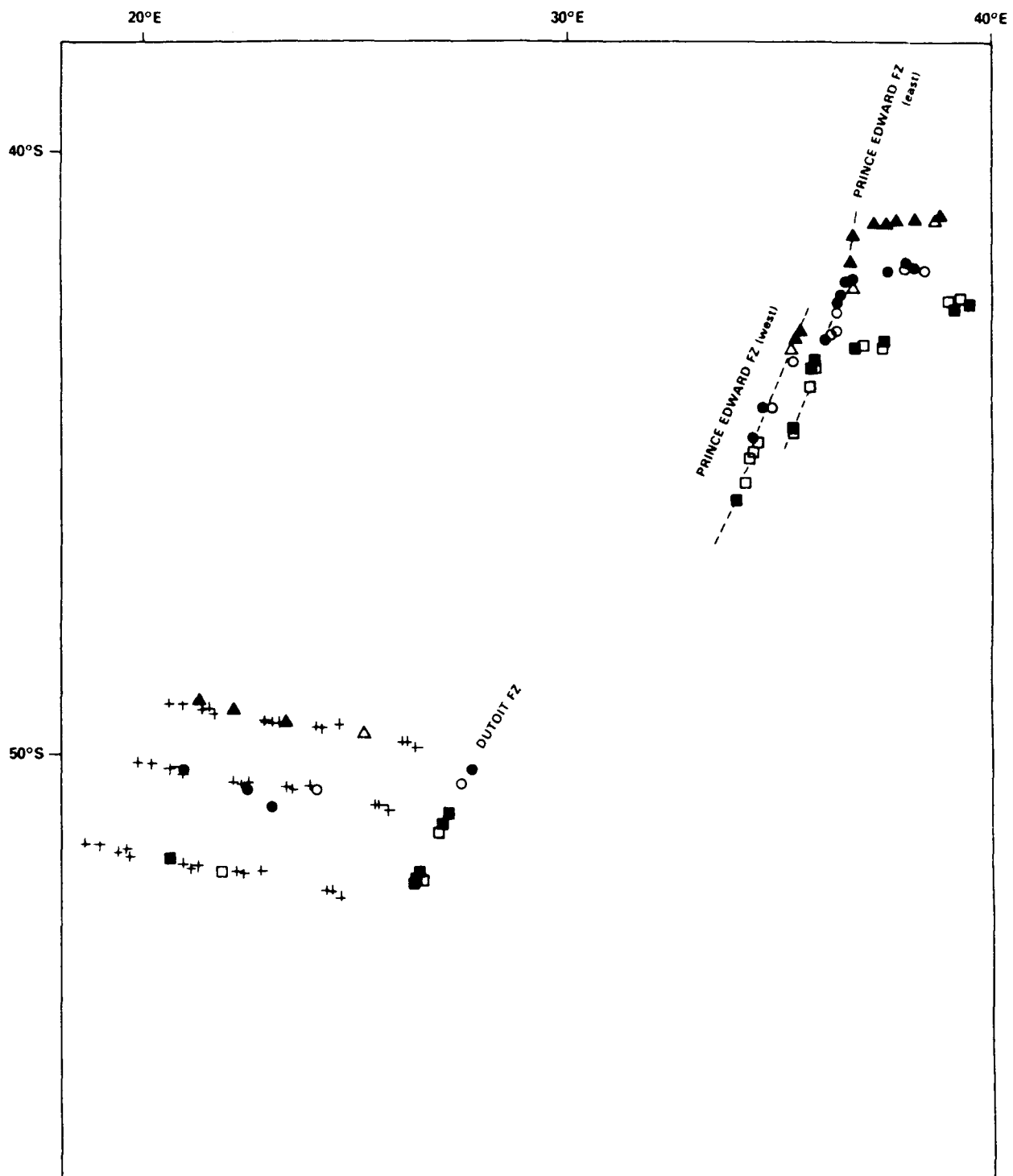


Figure 6b (same as Figure 6a)

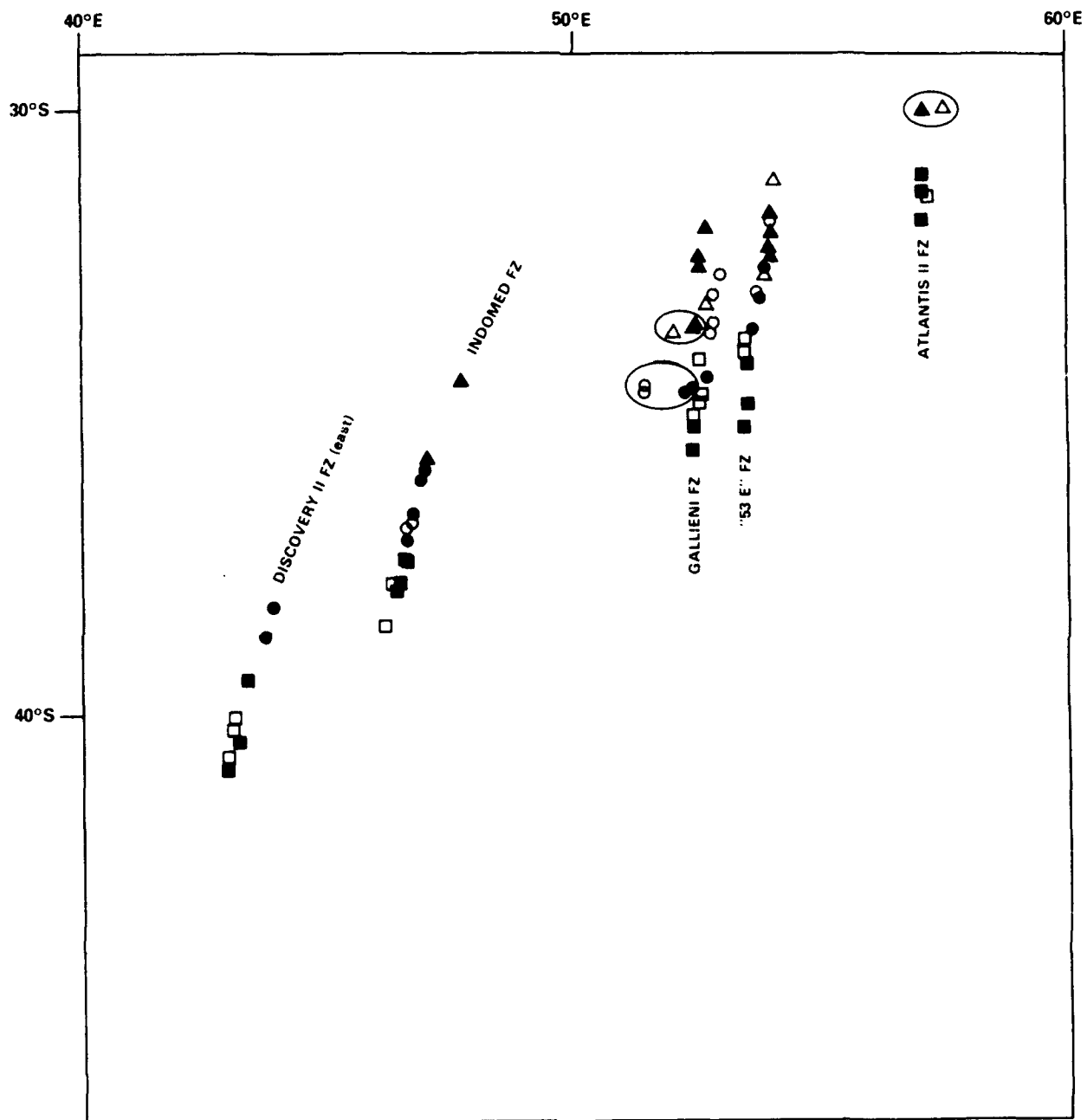


Figure 6c (same as Figure 6a; reconstructed magnetic anomalies circled)

than the northern extension of Shaka Fracture Zone. In view of the acceptable reconstructions at the other fracture zones, this misfit may indicate that at this latitude the Shaka Ridge is not the northern continuation of Shaka Fracture Zone.

#### ANOMALY 20:

The best-fitting pole for anomaly 20 lies at  $11.0^{\circ}\text{N}$ ,  $39.6^{\circ}\text{W}$  with a rotation angle of  $7.7^{\circ}$  (Figure 5c). Fossil transform faults are adequately reconstructed at Prince Edward (west and east), and "53 E" Fracture Zone. The reconstruction at Gallieni is not good; rotated points lie 40-50 km west of the fracture zone trace. All four of the magnetic lineations are adequately reconstructed with this pole of rotation. With this pole, rotated points from the Antarctic side of Shaka Fracture Zone overlie the Shaka Ridge.

#### FLOWLINES:

To check how well the finite poles predict the relative motion between Africa and Antarctica, flowlines are constructed using the appropriate stage poles (listed in Table 4) and compared to the observed fracture zone traces. Flowlines are calculated by rotating the northern ridge-transform intersections north about the African stage poles and the southern ridge-transform intersections about the Antarctic stage poles. From the present-day to anomaly 13, fracture zone trends and predicted flowlines coincide at all fracture zones except for Shaka, Bouvet and the Antarctic side of DuToit (Figures 4a, 4b). Observed and calculated trends match from the present to anomaly 6 but then deviate by up to 50 km on the Antarctic branch (Figure 6a, 7). One possibility

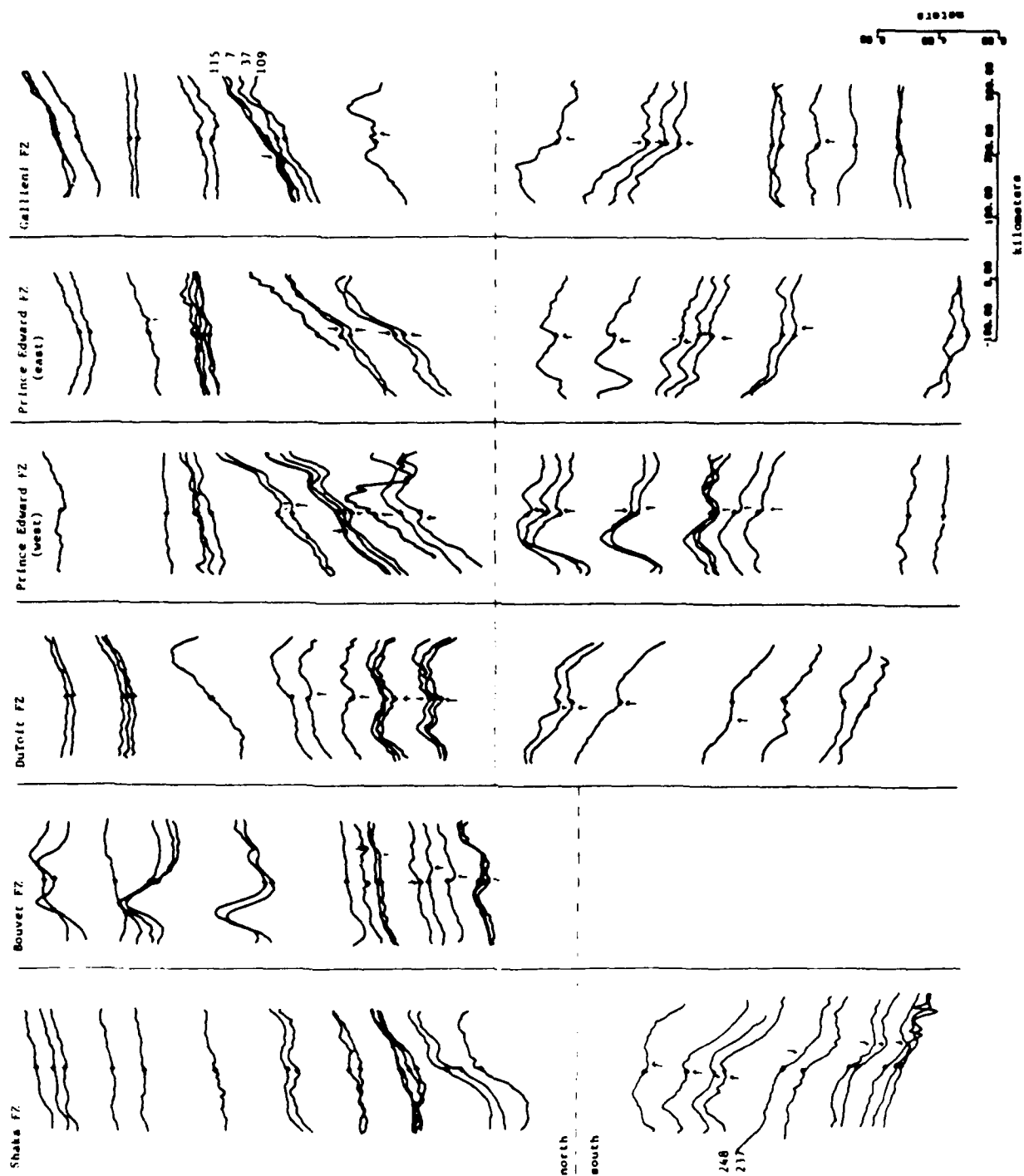


Figure 7 Seasat altimeter profiles projected perpendicular to the trend of flowlines calculated from the best-fitting poles for anomalies 6, 13 and 20. Intersections of track lines with predicted flowlines are marked by crosses. Arrows mark the locations of fracture zone crossings used in this study.

for this deviation is if the currently active Shaka transform did not exist prior to anomaly 13 and the observed fracture zone crossings represent a previously active transform. On the altimeter profiles (Figure 7) the shape of the fracture zone anomaly changes between profiles 248 and 237, which is also where the deviation occurs. The Shaka Transform is about 400 km long and the relatively small pole changes could conceivably have caused deformation within the transform so that the apparent fracture zone does not follow a flowline. At Bouvet Fracture Zone, fracture zone crossings are not easily identified (Figure 7) and appear to trend more easterly than the calculated flowlines. Changes in the pole position leading to improvements to the fit at Bouvet would increase the discrepancy at Shaka Fracture Zone, and vice versa. It is likely that the northern crossings at Bouvet (Figure 6) are not representative of the continuation of the present-day Bouvet transform but are instead attributable to another transform fault or tectonic feature.

The last section of predicted flowline from anomaly 13 to anomaly 20 compares well with the trends at DuToit (African plate), Prince Edward (west and east), Indomed, "53 E", and Atlantis II fracture zones. The northern bathymetric trend at Discovery II (eastern transform) is more easterly than predicted, and that at Gallieni is more westerly. There is some evidence in the altimeter profiles (Figure 7, Gallieni, profiles 109, 37, 7, 115) that the fracture zone trace could, in fact, be to the east but the correlation between track lines is too poor to resolve the trend.

Although this comparison between flowlines and fracture zone traces is somewhat redundant because the fracture zone trends are used to



construct the rotation parameters, the use of the magnetic anomaly lineations in the pole determinations introduces a certain amount of independence between the flowlines and fracture zone traces. Also, although the calculated finite poles may be correct, the time interval between successive poles may contain changes in spreading direction that are not resolved. If the data are sufficiently dense, such changes will be evident when flowlines and fracture zone trends are compared. The generally good coincidence of the trends and flowlines supports the use of these poles as accurate descriptors of African/Antarctic plate motion. Flowlines corresponding to the rotations derived in Fisher and Sclater (1983) are also indicated in Figures 4a, 4b and 4c (dashed lines). The primary difference in trends occurs between the anomaly 20-13 stage pole for this study and their anomaly 22-13 stage pole. Their pole was computed by fitting small circle arcs to the northern extensions of Shaka, Discovery II and Indomed Fracture Zones. Besides fitting these three fracture zones, the flowline predicted by this pole also coincides with the northern fracture zone crossings at Bouvet Fracture Zone. The flowlines fail to match fracture zone traces on the Antarctic side of Prince Edward (west and east transforms) and the African side of DuToit Fracture Zone. (The calculated flowlines for fracture zones east of Indomed cannot be distinguished from one another.) The fracture zone crossings at Prince Edward on the Antarctic plate are very well located (Figure 7) and are offset by 40-50 km from the Fisher and Sclater (1983) predictions. The crossings at DuToit on the African plate are much less clear (Figure 7) and the bathymetry in this region consists of a series of lineated ridges and valleys that makes it difficult to precisely determine the northern extension of

DuToit (see bathymetric map in Driscoll et al., 1987, and Figure 2, Chapter 2 of this thesis). It is not possible to determine which pole is more accurate with the limited amount of available geophysical information. However, because the finite rotation poles for anomalies 13 and 20 derived in this paper are based on a considerably larger data set that also includes magnetic anomaly information, they are preferred over previously published poles.

## DISCUSSION

### Mid-Cretaceous to Eocene plate motion:

The signatures of the presently active fracture zones in the altimeter profiles rapidly disappear on seafloor older than anomaly 20 and thus cannot be used to calculate finite rotation poles for earlier ages. Published rotation parameters for the Mid-Cretaceous to Eocene have been derived by reconstructing magnetic lineations and have resulted in two conflicting tectonic histories. One hypothesis is that the pole of rotation has remained stable for the past 80 Myr (Fisher and Sclater, 1983), and the other is that a major change in the direction of spreading occurred between anomalies 32 and 24 (Patriat, 1983; Patriat et al., 1985) and was followed by a return to a direction similar to the present-day direction of spreading. If the presently active fracture zones were also active before and during the proposed change in the direction of seafloor spreading, their trends would be as illustrated by the dotted lines in Figures 4a, 4b and 4c. The altimeter profiles for DuToit and Prince Edward do not show obvious traces of the fracture zones prior to about anomaly 22 time (Figure 7). Royer et al. (1987)

propose that the change in plate motion caused a major plate reorganization, with the destruction of the previously active fracture zones and the creation of the presently active fractures. A general search in the proposed direction of motion on seafloor between anomalies 32 and 24 does not show compelling evidence for fracture zone traces in this direction except for two short segments east of DuToit (Figure 8). Because of the expected weakness of the altimeter signal for these older ages, the lack of obvious trends does not disprove the hypothesis. A necessary check on the validity of the proposed change in plate motion will be best accomplished by the acquisition of additional magnetic lineation pairs, particularly on seafloor west of Indomed Fracture Zone.

#### Improvements in the parameters of plate rotation:

The finite rotation poles determined in this study are well-constrained and accurate for the three discrete time intervals represented by magnetic anomalies 6, 13, and 20. The method by which they are determined, however, does not fully exploit the information available in the altimeter profiles. To fully utilize this information on fracture zone trends within the data set, an inversion scheme such as that developed by Shaw (1987) should be used. With this method, fracture zone crossings on all altimeter profiles for a given time period and set of transform faults are identified simultaneously. The stage poles which minimize the error between the predicted flowlines and fracture zone identifications are found for each plate of the two plate system. A major advantage of the inversion method over the one used in this paper is that it is not necessary to have fracture zone crossings on both plates for any given time interval because stage poles and not

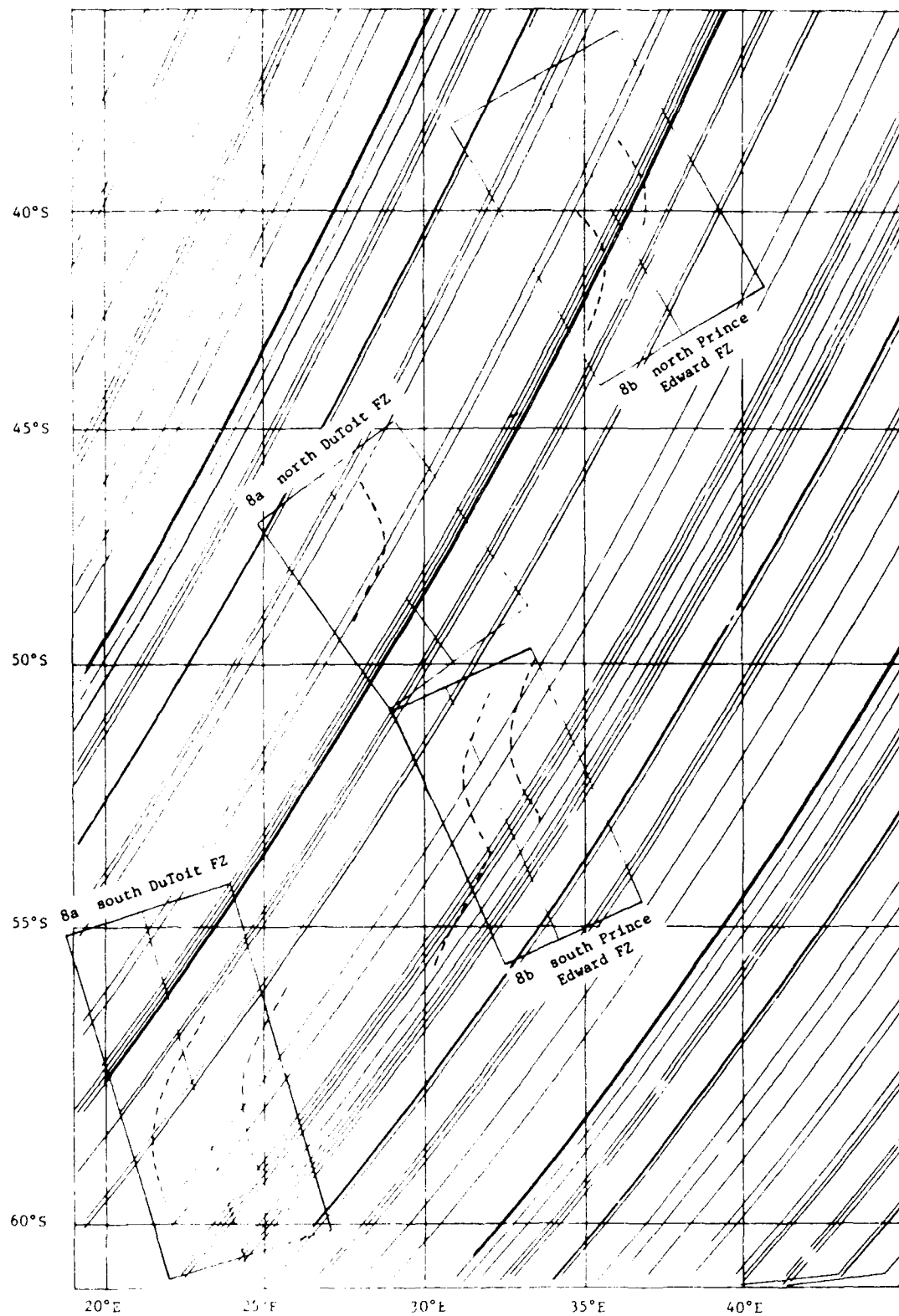


Figure 8 Index map. Dashed lines correspond to proposed flowlines for anomaly 32 to 28 plate motions.

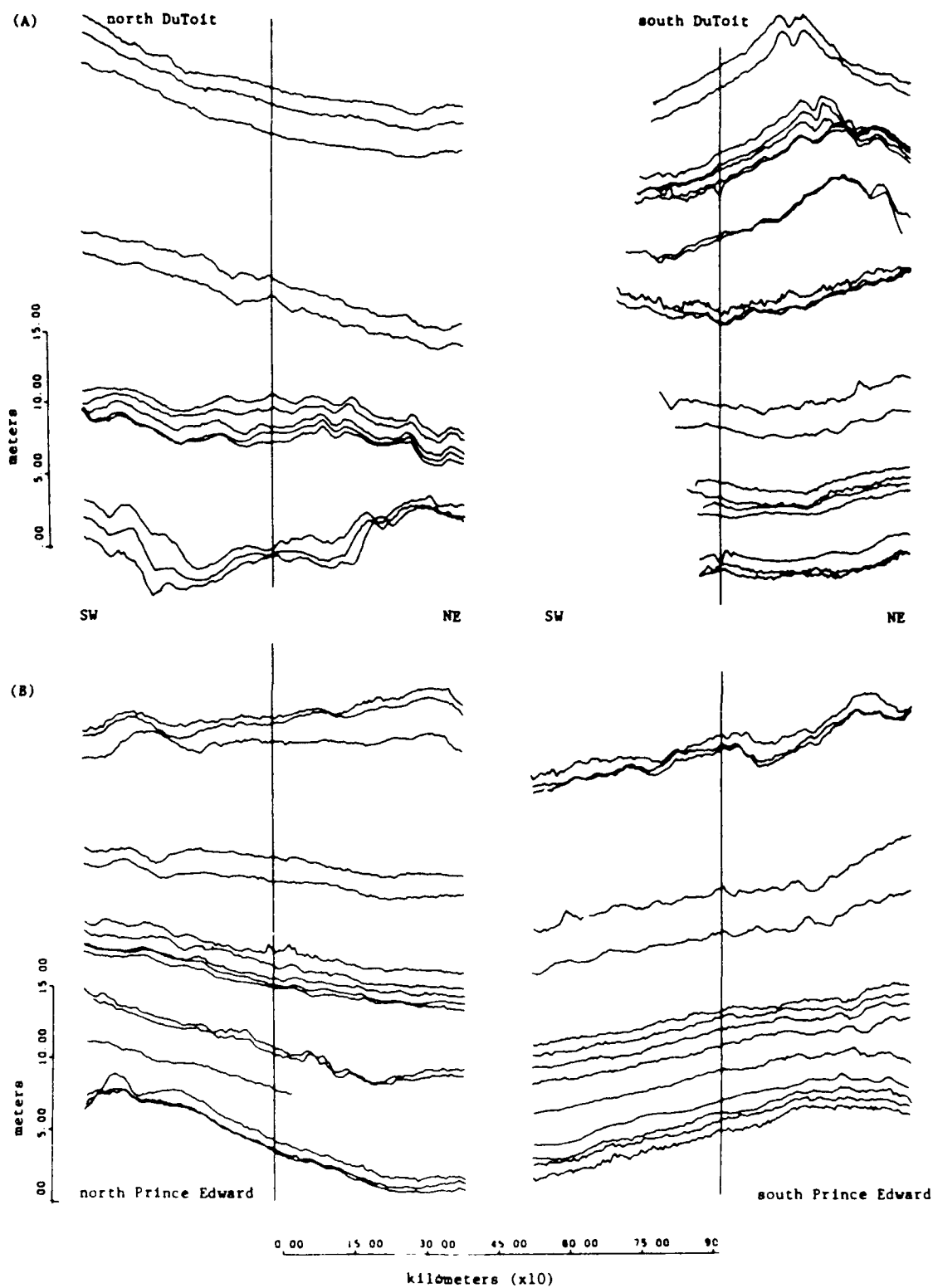


Figure 8 Seasat altimeter profiles projected perpendicular to the trend of the hypothesized change in direction of plate motion during the interval between magnetic anomalies 28 and 32.

finite rotation poles are determined. The limitations on the accuracy and suitability of the inversion depend on the amount of deformation that may have occurred within the active transform and on the longevity of the currently active transform faults. The first limitation should be minimal on post-anomaly 20 seafloor which has seen only minor changes in the direction of spreading. As discussed in the preceding section, the question of the longevity of the fracture zones is unresolved. If the inversion fails on seafloor older than about anomaly 24 then the non-stationary behaviour proposed by Patriat et al. (1985) has most likely occurred.

#### Conclusions:

Instantaneous and finite rotation poles for the times of anomalies 6, 13 and 20 determined from a set of magnetic lineations and fracture zone crossings confirm the stability of the African-Antarctic pole of motion for the past 47 Myr. The instantaneous pole is based entirely on fracture zone azimuths from the Southwest Indian Ridge and is located within  $9^\circ$  of poles determined by using global inversions and by closure around a 4-plate system.

The finite rotation poles for anomalies 13 and 20 are significantly different from those published in Fisher and Sclater (1983). Although the finite poles for anomalies 6, 13 and 20 correctly predict the observed motion at most fracture zones, discrepancies exist at the Bouvet and Shaka Fracture Zones and additional work is necessary to assess the accuracy of these poles.

## BIBLIOGRAPHY

- Bergh, H.W. and I.O. Norton, 1976, Prince Edward Fracture Zone and the evolution of the Mozambique Basin. *J. Geophys. Res.*, 81, 5221-5239.
- Cande, S.C., J.L. LaBrecque, W.F. Haxby, S. Mello, and D.B. Rawley, A high resolution sea floor spreading history of the South Atlantic, Geodynamics symposium, Texas A & M University, April 1986.
- Chase, C.G., 1972, The N plate problem of plate tectonics, *Geophys. J. R. astr. Soc.*, 29, 117-122.
- Driscoll, M.L., R.L. Fisher and B. Parsons, 1987, Fracture zone trends and structure at the Southwest Indian Ridge: An investigation using Seasat altimetry and surface-ship bathymetry, *Geophys. J. R. astr. Soc.* (submitted).
- Fisher, R.L. and J.G. Sclater, 1983, Tectonic evolution of the Southwest Indian Ocean since the Mid-Cretaceous: Plate motions and stability of the pole of Antarctica/Africa for at least 80 Myr. *Geophys. J. R. astr. Soc.*, 73, 553-576.
- Forsyth, D.W., 1975, Fault plane solutions and tectonics of the South Atlantic and Scotia Sea., *J. Geophys. Res.*, 80, 1429-1443.
- Hellinger, S.J., 1981, The uncertainties of finite rotations in plate tectonics, *J. Geophys. Res.*, 86, 9312-9318.
- Minster, J.B., and T.H. Jordan, 1978, Present-day plate motions, *J. Geophys. Res.*, 83, 5331-5354.
- Minster, J.B., T.H. Jordan, P. Molnar and E. Haines, 1974, Numerical modelling of instantaneous plate tectonics, *Geophys. J. R. astr. Soc.*, 36, 541-576.
- McKenzie, D. and J.G. Sclater, 1971, The evolution of the Indian Ocean since the late Cretaceous, *Geophys. J. R. astr. Soc.*, 25, 437-528.
- Norton, I.O., 1976, The present relative motion between Africa and Antarctica, *Earth Planet. Sci. Lett.*, 33, 219-230.
- Norton, I.O. and J.G. Sclater, 1979, A model for the evolution of the Indian Ocean and the breakup of Gondwanaland, *J. Geophys. Res.*, 84, 6803-6830.
- Patriat, P., 1983, Evolution du systeme de dorsales de l'Ocean Indien, These de Doctorat d'Etat, Universite' Pierre et Marie Curie, Paris.
- Patriat, P., J. Segoufin, J. Goslin and P. Beuzart, 1985, Relative positions of Africa and Antarctica in the upper Cretaceous: Evidence for unstationary behaviour of fracture zones., *Earth planet. Sci Lett.*, 75, 204-214.
- Royer, Jean-Yves, p. Patriat, H.W. Bergh and C.R. Scotese, 1987, Evolution of the Southwest Indian Ridge from the late Cretaceous (anomaly 34) to the Middle Eocene (anomaly 20), *Tectonophysics* (submitted).

- Sclater, J.G. C. Bowin, R. Hey, H. Hoskins, J. Pierce, J. Phillips and C. Tapscott, 1976, The Bouvet Triple Junction, J. Geophys. Res., 81, 1857-1869.
- Sclater, J.G., H. Dick, I.O. Norton, and D. Woodroffe, 1978, Tectonic structure and petrology of the Antarctic plate boundary near the Bouvet Triple Junction, Earth planet. Sci. Lett., 37, 393-400.
- Sclater, J.G. and R.L. Fisher, 1974, The evolution of the east central Indian Ocean, Bull. geol. Soc. Am., 85, 683-702.
- Sclater, J.G. R.L. Fisher, P. Patriat, C. Tapscott and B. Parsons, 1981, Eocene to recent development of the South-west Indian Ridge, a consequence of the evolution of the Indian Ocean Triple Junction, Geophys. J. R. astr. Soc., 64, 587-604.
- Shaw, P.R., 1987, Investigations of relative plate motions in the South Atlantic using Seasat altimeter data, J. Geophys. Res., (in press).
- Tapscott, C.R., P. Patriat, R.L. Fisher, J.G. Sclater, H. Hoskins and B. Parsons, 1980, The Indian Ocean Triple Junction, J. Geophys. Res., 85, 4723-4739.
- Watts, A.B., J.R. Cochran, P. Patriat and M. Doucoure, 1985, A bathymetry and altimetry profile across the Southwest Indian Ridge crest at 31 S latitude, Earth Planet. Sci. Lett., 73, 129-139.



TABLE 1 INSTANTANEOUS POLES OF ROTATION

	LATITUDE N	LONGITUDE E	RATE (DEG/MY)	SOURCE
A	2.74	-36.67	0.150	THIS STUDY
B	8.40	-42.40	0.150	SCLATER ET AL., 1981
C	5.60	-39.40	0.150	TAPSCOTT ET AL., 1980
D	9.50	-41.70	0.149	MINSTER AND JORDAN, 1978
E	-4.00	-32.00	--	SCLATER ET AL., 1978
F	23.40	-49.40	0.166	SCLATER ET AL., 1976
G	23.10	-51.30	0.176	FORSYTH, 1975
H	-19.00	-13.30	0.190	MINSTER ET AL., 1974
I	4.00	-51.00	0.212	CHASE, 1972
J	-16.00	-38.00	0.180	MCKENZIE AND SCLATER, 1971

Table 2. Comparison between observed and predicted fracture zone azimuths §

Latitude °N	Longitude °E	observed azimuth	calculated azimuth	difference in azimuths (deg)
-54.04	2.38	N 46.81 E	N 46.19 E	0.62
-54.36	5.89	40.74	42.81	-2.07
-53.19	9.46	40.67	38.99	1.68
-52.20	14.00	36.00 a	34.42	1.58
-52.83	25.67	25.17	24.24	0.93
-51.50	28.63	22.25	21.44	0.81
-46.40	33.72	13.23	16.33	-3.10
-45.42	35.12	10.29	15.09	-4.80
-42.93	41.75	14.57	9.94	4.63
-41.98	42.59	7.23	9.26	-2.03
-36.57	52.35	3.28	2.78	0.50
-33.00	57.00	0.00 b	0.30	-0.30
-31.70	58.35	2.00 b	-0.30	2.30
-31.00	60.75	-2.00 b	-1.34	-0.66

§ for pole of rotation at 2.7°N, 36.7°W

a from Norton, 1976

b from Tapscott et al., 1981

Table 3. Fracture zone crossings, magnetic anomaly lineations and their uncertainties for magnetic anomaly 6, 13, and 20 reconstructions

Anomaly 6 magnetic lineations	African Plate			Antarctic Plate		
	Lat.°N	Long.°E	error(km)	Lat.°N	Long.°E	error(km)
1.	-55.55	20.60	20.	-54.12	19.60	30.
2.	-43.48	36.76	20.	-46.10	35.92	20.
	-43.36	37.46	20.	-46.17	36.40	20.
3.	-42.80	39.14	20.	-45.38	38.09	20.
	-42.74	39.50	20.	-45.36	38.35	20.
Bouvet FZ	-53.63	3.14	15.	-54.79	1.17	15.
	-53.56	3.25	15.	-54.72	1.33	15.
	-53.20	4.12	15.	-54.55	1.49	15.
	-53.10	4.19	15.			
	-53.08	4.28	15.			
Moshesh FZ	-54.00	5.00	15.	-54.95	3.40	15.
	-53.95	5.12	15.	-54.55	4.11	15.
	-53.94	5.24	15.	-54.48	4.10	15.
				-54.40	4.20	15.
Islas Orcadas FZ	-53.70	7.01	15.	-55.19	4.86	15.
				-55.14	4.89	15.
				-55.04	4.95	15.
DuToit FZ	-51.93	26.34	15.	-54.36	24.54	15.
	-51.88	26.37	15.	-53.70	25.00	15.
	-51.77	26.45	15.	-53.57	25.10	15.
Prince Edward FZ (western transform)	-46.02	33.95	15.	-48.37	32.92	15.
				-47.97	33.03	15.
				-47.87	33.12	15.
				-47.68	33.26	15.
(eastern transform)	-44.84	35.29	15.	-47.55	34.12	15.
	-43.83	35.72	15.	-46.80	34.58	15.
	-43.71	35.81	15.	-46.46	34.68	15.
Discovery II (eastern)	-40.84	42.92	30.	-43.40	42.22	15.
	-40.42	43.15	30.	-43.01	42.32	15.
	-39.48	43.33	30.	-42.79	42.37	15.
Indomed FZ	-38.06	46.35	15.	-41.40	45.54	30.
	-37.94	46.41	15.	-40.72	45.72	30.
	-37.60	46.56	15.	-40.33	45.98	30.
	-37.55	46.53	15.			

Gallieni FZ	-35.80	52.36	30.	-38.00	52.12	30.
	-35.41	52.42	30.	-37.78	52.26	15.
				-37.66	52.29	30.
				-37.09	52.25	30.
" 53 E" FZ	-35.42	54.44	30.	-36.96	53.20	15.
	-35.05	53.52	15.	-36.72	53.22	30.
	-34.36	53.51	15.			
Atlantis II FZ	-31.92	57.05	30.	-34.30	57.05	30.
	-31.44	57.08	30.			
	-31.15	57.07	30.			

<u>Anomaly 13</u>				<u>African Plate</u>			<u>Antarctic Plate</u>		
magnetic lineations	Lat.°N	Long.°E	error(km)	Lat.°N	Long.°E	error(km)			
1.	-50.25	20.90	20.	-55.40	19.35	20.			
	-50.55	22.40	15.						
	-50.80	23.00	25.						
2.	-42.30	36.71	15.	-47.60	35.12	15.			
	-42.17	37.54	15.	-47.58	36.10	20.			
	-42.04	38.02	15.	-47.52	35.60	20.			
	-42.09	38.17	15.						
3.	-34.85	52.25	15.	-40.48	50.44	15.			
	-34.80	52.40	20.	-40.37	50.45	15.			
DuToit FZ	-51.07	27.01	15.	-55.49	23.17	15.			
	-50.92	27.14	15.						
	-50.27	27.69	15.						
Prince Edward FZ (western)	-45.00	34.38	15.	-49.82	31.97	15.			
	-44.49	34.59	15.	-49.08	32.55	15.			
(eastern transform)	-43.35	36.08	30.	-48.64	33.61	15.			
	-42.69	36.35	15.	-48.59	33.74	15.			
	-42.56	36.44	15.	-48.25	33.74	15.			
	-42.35	36.55	30.						
Indomed FZ	-37.25	46.58	15.	-42.65	45.16	15.			
	-36.85	46.70	15.	-42.56	45.28	15.			
	-36.28	46.85	15.						
	-36.12	46.93	15.						
Gallieni FZ	-34.60	52.69	30.	-39.51	51.89	15.			
				-39.31	51.95	15.			
				-38.84	51.93	15.			
				-38.50	52.10	30.			
" 53 E" FZ	-33.80	53.62	30.	-38.81	52.89	15.			
	-33.26	53.75	30.	-37.55	53.18	15.			
	-32.75	53.88	15.						

Table 3. continued

<u>Anomaly 20</u>	<u>African Plate</u>			<u>Antarctic Plate</u>		
magnetic lineation	Lat.°N	Long.°E	error(km)	Lat.°N	Long.°E	error(km)
1.	-49.20	21.30	20.	-56.38	18.90	25.
	-49.35	22.10	20.			
	-49.55	23.30	20.			
2.	-41.34	37.25	20.	-48.65	35.45	20.
	-41.34	37.50	20.			
	-41.29	37.76	20.			
	-41.27	38.23	20.			
	-41.21	38.76	20.			
3.	-33.75	52.45	20.	-41.34	51.05	20.
				-41.42	50.65	20.
	-30.05	57.10	20.	-37.50	56.65	20.
Prince Edward	-43.23	35.47	15.	-50.75	31.40	15.
FZ(western)	-43.35	35.37	15.	-50.43	31.65	15.
(eastern)	-42.00	36.67	15.	-49.76	33.17	15.
	-41.55	36.72	15.			
Gallieni FZ	-32.75	52.35	30.	-40.95	51.39	15.
	-32.57	52.52	15.			
	-32.10	52.67	30.			
" 53 E" FZ	-32.58	53.97	15.	-40.43	52.67	15.
	-32.39	53.94	30.	-38.81	52.89	15.
	-32.13	54.00	30.			
	-31.84	53.96	30.			

Table 4. Finite Rotation Poles and Stage Poles for Africa/Antarctica

Finite Rotation Pole (Africa Fixed)

Anomaly	Latitude (°N)	Longitude (°E)	Rotation Angle (°)
6	5.6	-37.4	2.8
13	8.8	-37.6	5.7
20	11.0	-39.6	7.7

Stage Poles:

anomaly interval	Latitude (°N)	Longitude (°E)	Rotation Angle (°)
<u>African Plate</u>			
0-6	5.6	-37.4	1.40
6-13	11.87	-38.0	1.46
13-20	16.72	-45.8	1.01
<u>Antarctic Plate</u>			
0-6	5.6	-37.4	-1.40
6-13	11.89	-37.6	-1.46
13-20	17.49	-45.0	-1.01

Chapter 4. Cooling of the oceanic lithosphere -- Evidence from geoid anomalies across the Udintsev and Eltanin Fracture Zones

Abstract:

The often step-like variation in the marine geoid across fracture zones is believed to reflect the change in age of the ocean floor, and hence in temperature structure of the plate across the fracture zone. The rate of change of the geoid with age has been estimated as a function of age from geoid offsets across fracture zones and used to constrain thermal models of lithospheric cooling. Results from three studies of the geoid offsets across the Mendocino fracture zone are consistent with a thermal plate cooling model having a plate thickness between 100 km and 125 km. This is in contrast to results obtained from the combined measurements from fracture zones in the South Pacific, which are not consistent with either the plate model or boundary layer model of cooling. To examine this inconsistency we have measured geoid offsets on Seasat profiles across the Udintsev and Eltanin fracture zones in the South Pacific and tested the robustness of the measurement technique. We used a second-order polynomial that included a step function centered on the fracture zone to estimate the regional geoid and the geoid offset. The polynomials were fit to the geoid profiles using least-squares minimization criteria. Data within a certain distance of the fracture zone were excluded from the fitting procedure in order to account for horizontal cooling and lithospheric deformation near the fracture zone. We find that the estimate of the geoid offset is very sensitive to the length of data excluded and that generally, an exclusion width of 100-200 km is needed to avoid anomalies (unrelated to the regional geoid offset) near the fracture zone. Exclusion widths of less than 100 km generally lead to unpredictable errors in the geoid offset estimates.

Using exclusion widths of between 150 km and 200 km on most profiles, we constructed geoid slope versus average age plots for each of the limbs



of the two fracture zones. Similar trends were found on both the east and west limbs of the Eltanin and the east limb of the Udintsev. The trends were inconsistent with a single thermal plate thickness and instead showed an initial decrease in slope between 0 and 35 m.y., followed by an abrupt increase followed again by a decrease in slope. In contrast, the west branch of the Udintsev shows an increase in geoid slope values between 20 and 35 m.y., followed by a decrease. The difference in observed trends across the western limb of the Udintsev may be due to the effects of the Louisville Ridge (north of the fracture zone) on the regional geoid. The similarity in trends on the remaining three limbs argues against the effects of isolated thermal or bathymetric anomalies and appears instead, to reflect a general feature of the geoid-slope versus average age relationship across fracture zones. Although the thermal plate cooling model is successful in predicting both seafloor depths and heat flow values out to ages of at least 80 m.y. B.P., it cannot explain the observed geoid slope values for these two fracture zones. It is not clear at this point whether this is due to inadequacies in the cooling model or to peculiarities in fracture zone evolution, possibly caused by small-scale convection driven by the horizontal temperature gradients beneath fracture zones.

## Introduction:

As oceanic lithosphere is created and transported away from mid-ocean spreading ridges it cools and contracts and the depth to the seafloor deepens. Empirical depth versus age curves have been compiled for the major ocean basins [1, 2] and, in general, show mean seafloor depths increasing as the square root of age out to 60-80 m.y. B.P. For older ages, the seafloor asymptotically approaches a constant depth. Several thermal cooling models have been proposed in order to explain the observed depth versus age relations. In the simplest case heat is lost through vertical heat conduction with no limit on the depth to which cooling can occur. This model accurately describes the subsidence of the oceanic lithosphere up to ages between 60-80 m.y. B.P. but does not predict the flattening of the mean depth versus age curves for older seafloor. Alternatively, cooling of a finite thickness plate with a bottom surface held at a constant temperature accurately predicts seafloor depths for both young and old ages when the thickness of the plate and the bottom boundary temperature are suitably adjusted. At older ages in this model, the heat lost through the upper surface of the plate balances the heat flux from the bottom surface which results in the observed flattening of seafloor depths at large ages. Although the plate cooling model provides an accurate mathematical description of the observed seafloor depths, the model does not specify how the isothermal condition required at the base of the plate could be maintained within the earth. One physical mechanism which has been proposed to bring heat to the base of the plate is small-scale convection [3]. This convection would occur on scales much smaller than the plates themselves and would advect hot material from within the mantle up to the base of the cooling lithosphere.

More recently, variations in the height of the marine geoid with seafloor age have been used to constrain thermal cooling models. The isostatic geoid anomaly due to the cooling of the lithosphere is more sensitive than the subsidence of the seafloor to temperature variations at larger depths. This difference is reflected in the weighting by  $z$  that appears in the integral equation for the isostatic geoid anomaly and not in the equation for seafloor subsidence:

$$w(t) = \frac{\rho_m \alpha}{(\rho_m - \rho_w)0} \int_0^{d_c} [T_m - T(t, z)] dz \quad (1)$$

$$N(t) = \frac{-2\pi G \rho_m}{g} \int_0^{d_c} z [1 - \alpha(T(t, z) - T_m)] dz \quad (2)$$

where  $w(t)$  is the variation in seafloor depth with age,  $N(t)$  is the variation in geoid height with age and  $d_c$  is the compensation depth. The remaining parameters are defined in Table 1. The temperature structure  $T(t, z)$  is dependent on the assumed cooling model. For half-space cooling the temperature varies as

$$T(t, z) = T_m \operatorname{erf}\left(\frac{z}{2\sqrt{\kappa t}}\right) \quad (3)$$

and for the plate-cooling model,

$$T(t, z) = T_m \left[ \frac{z}{a} + \frac{2}{\pi} \sum_{n=1}^{\infty} \frac{1}{n} \exp(-n^2 \pi^2 \kappa t / a^2) \sin(n \pi z / a) \right] \quad (4)$$

where  $a$  is the thickness of the plate. Unlike seafloor depths, the geoid contains large amplitude variations which are caused by lateral density variations within the mantle. Separating these large-amplitude, long-wavelength anomalies from those arising from density and temperature variations within the lithosphere is difficult. Because of this, it is impossible, in most cases, to directly measure geoid height variations as a

function of seafloor age. An exception to this is at oceanic fracture ones where there is an abrupt change in the age of the seafloor across the fracture zone and a corresponding change in the height of the geoid. This offset in the geoid occurs over a distance of several hundred kilometers. A long-wavelength geoid can be subtracted from the observed profile and the remaining geoid offset measured as a function of the age difference across the fracture zone. We assume that the long-wavelength geoid which is removed adequately approximates the regional geoid field unrelated to lithospheric cooling, although in our analysis we find that this may not be true in all cases.

Geoid slopes (geoid offsets divided by the age offset) estimated across the Mendocino Fracture Zone show a decrease with increasing age of the seafloor. The measurements are compatible with the plate cooling model assuming a plate thickness of 100-120 km [4, 5]. These plate thicknesses agree with those found by modeling the subsidence of the seafloor in the North Pacific [1]. However, offsets across the Udintsev Fracture Zone in the South Pacific were measured by Cazenave et al. [6] who found that a thermal plate thickness of 50-70 km fit the data for ages less than 30 m.y. and a larger plate thickness in the range of 70-90 km for older ages. Subsequent analyses by Cazenave [7, 8] concluded that distinct thermal plate thicknesses for ages less than 30 m.y. and greater than 30 m.y. are representative of the whole Pacific Ocean. This unexpected finding and the large discrepancy in the estimates of thermal plate thickness between the Mendocino and Udintsev Fracture Zones are not satisfactorily explained by either the half-space or the plate cooling models.

In this paper we analyze Seasat profiles across the Eltanin and Udintsev fracture zones for two main purposes. The first is to test the

accuracy of the measurement technique used here to determine the geoid offsets across the fracture zones. The geoid profiles are approximated by a second-order polynomial which includes a step function, and both the length of the profile and the amount of data excluded near the fracture zone are found to greatly affect the determination of the geoid offset. Secondly, each branch of the fracture zones is analyzed separately to see whether observed trends in the geoid slopes are consistent across the whole area and indicative of regional trends, or confined to a particular fracture zone and representative of local thermal or structural anomalies. Both the measurement technique and data presentation used here are significantly different from that in Cazenave [7, 8] and Cazenave et al.[6], and roughly twice as many profiles across the Udintsev and Eltanin are used in this analysis than in the previous ones.

Despite the differences in method, our results from the Eltanin Fracture Zone System agree with the previous findings [7, 8] that a simple plate cooling model cannot explain the observed geoid offsets. Results from the Udintsev Fracture Zone were less conclusive and differences were found in the geoid slope-age relationship between the western and eastern limbs of the fracture zone. However, neither the plate cooling model or half-space cooling model are able to explain the observed geoid slope-age relationships.

#### Udintsev and Eltanin Fracture Zones:

The Udintsev and Eltanin fracture zones in the South Pacific are located on the Pacific-Antarctic Rise which is currently spreading at a full rate of  $\sim 60$  mm/yr (Figure 1). Seafloor topography is smooth and the spacing between major fracture zones is fairly large, typical of fast-spreading ridges. Ship-track coverage is sparse but several track lines parallel to

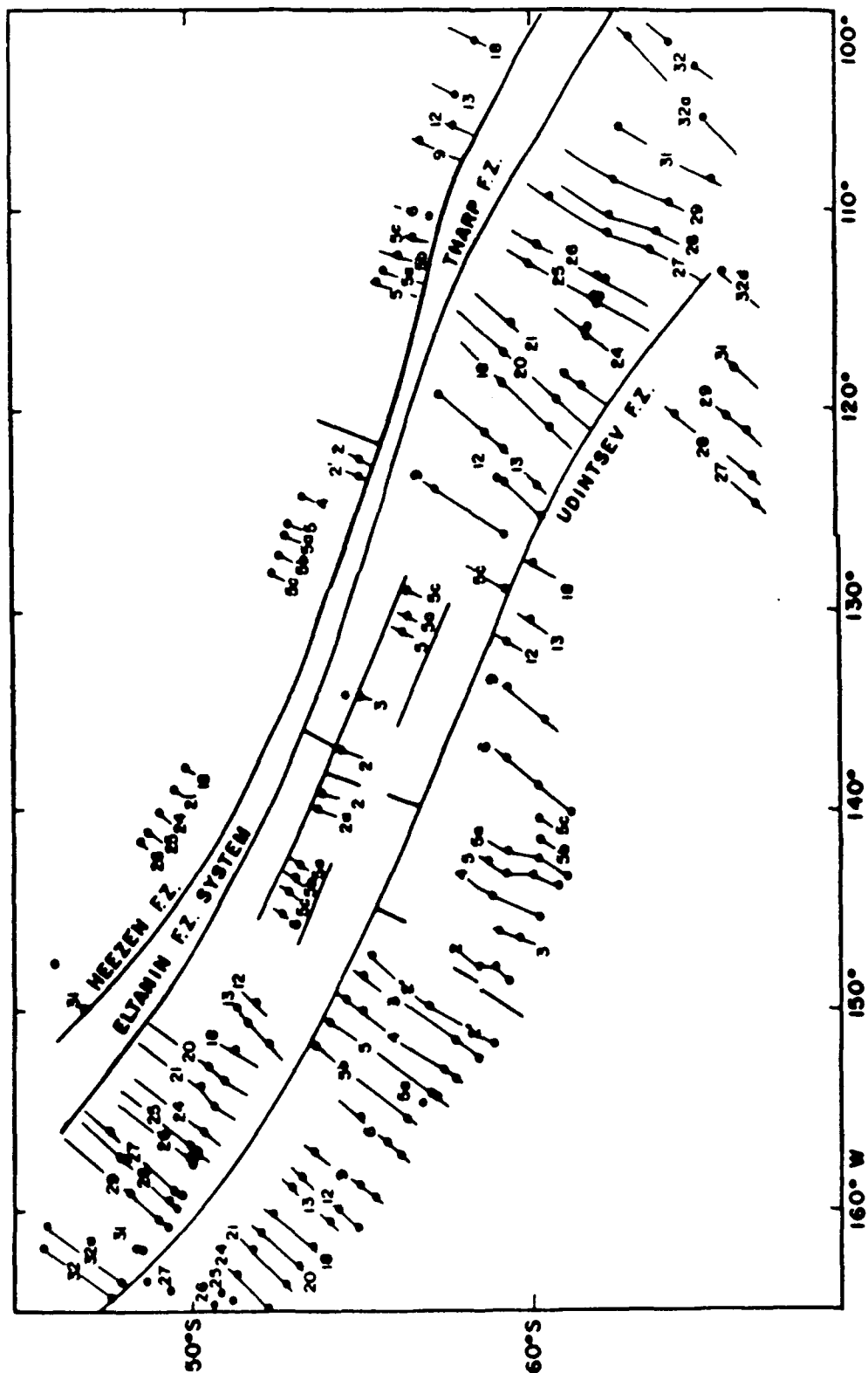


Figure 1 Magnetic anomalies and location of the Udintsev Fracture Zone and Eltanin Fracture Zone System in the South Pacific (from Molnar et al., 1975)

the fracture zones provide fairly complete magnetic anomaly identifications south of the Udintsev Fracture Zone. Magnetic anomaly locations are taken from Molnar et al. [9]. North of the Udintsev fracture zone the identified anomaly sequence is complete from anomalies 12 to 32. Only one track line contains identifications for anomalies 2 through 6 and these are located north of a presently inactive, small-offset fracture zone between the Udintsev and Eltanin fracture zones. The Eltanin Fracture Zone System is made up of the closely-spaced Heezen and Tharp fracture zones. North of the Eltanin System anomalies 5 to 18 are located on the eastern limb and the sequences 1 to 5c and 18 to 32 on the western limb. Ages for the magnetic anomalies were determined using the time scale of LaBreque et al. [10].

The age offset across the Eltanin Fracture Zone System is 30-34 m.y. at the present and has ranged from 24 m.y. to 39 m.y. in the past due to spreading rate variations. At the present time, the Udintsev fracture zone has an age offset of 9-11 m.y. and its age offset has ranged from 7 m.y. to 20 m.y. in the past. With these large age offsets the amplitudes of the geoid variations across the fracture zones are also quite large (1 m to 5 m at the ridge crest-transform intersections) and distinct in maps of sea-surface heights [e.g. 11].

#### Method:

Geoid height offsets were estimated by fitting a second-order polynomial and a step function to the observed profiles. This method was first introduced by Crough [12] to measure offsets on geoid profiles across the Mendocino Fracture Zone. The second-order polynomial is used to approximate the regional geoid, and the step-function weighted by a value  $\Delta N$  approximates the geoid offset at the fracture zone. The total geoid

height is given by  $N(x)$  where:

$$N(x) = a + bx + cx^2 + \Delta N \cdot H(x - x_f) ; x_f = \text{location of fracture zone} \quad (5)$$

Within 100-200 km of the fracture zone, the geoid is affected by lateral diffusion of heat across the fracture zone which smooths out the sharpness of the geoid offset [4]. Topographic effects created by lithospheric flexure [13] or by the action of bending moments on the free ends of the lithosphere [14] may also contribute important components to the observed geoid signal near the fracture zone. These thermal and mechanical effects are assumed to be localized near the fracture zone and to have little effect on the regional geoid offset due to the change in lithospheric age outside of this region. In order to avoid biasing the estimate of the regional geoid offset by these unmodeled effects, points within a certain distance of the fracture zone were excluded from the fitting process. The width of the zone excluded from the least-squares fitting process substantially affects the geoid step estimation. In this analysis we examined the effects of excluding widths between 0 and 200 km on each side of the fracture zone. Examples from each side of the two fracture zones (Figure 2) show an increase in the estimated geoid offset with the larger exclusion widths. On the west side of the Udintsev, the geoid offset on profile R0875 increases from 0.73 m when no exclusion width is used, to 1.90 m when a width of 200 km is used. Likewise, the estimated offsets on profile R0185 on the east limb of the Udintsev increases from 0.65 m to 2.55 m. On the Eltanin, the affect of changing the exclusion width is the same. Profile R0257 increases from 1.81 m to 2.82 m in going from a 0 to 200 km exclusion width and on the opposite limb, offsets on profile R0400 increase from 1.95 m to 3.66 m. Increasing the exclusion width to 100 km and 200 km can substantially increase, and in some cases, more than double



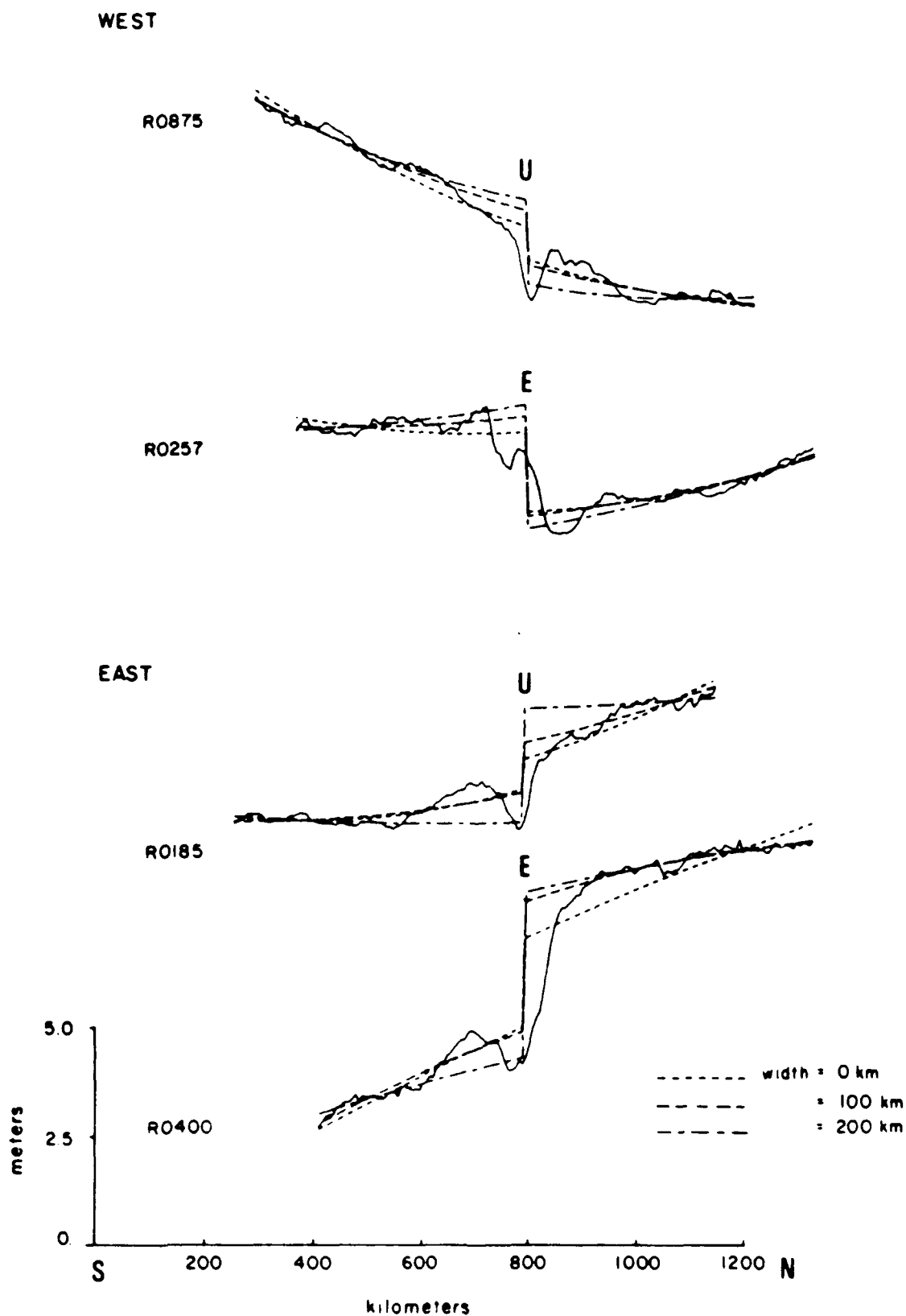


Figure 2 Geoid profiles across the Eltanin and Udintsev fracture zones. The regional field is approximated by a second-order polynomial for cases where data within 0, 100, and 200 km of the fracture zone is excluded in the least-squares fit to the observations.

the amplitude of the estimated geoid offset.

An increase in the geoid offset with increasing exclusion width is expected. Detrick [4], and Sandwell and Schubert [5] attributed one source of this increase to the effects of horizontal heat conduction across the fracture zone which tend to smooth out the abrupt geoid step. The sloping of the geoid towards the fracture zone biases the estimate of the regional polynomial and causes an underestimate of the offset. Although the sloping of the geoid towards the fracture zone is important, additional anomalies near the fracture zone can be seen to severely bias the regional polynomial estimates (Figure 2). Almost all profiles across the Udintsev fracture zone display an anomaly adjacent to the fracture zone on the older side which is 150-200 km wide and 0.5-1.0 m high. Parmentier and Haxby [14] modeled this anomaly as a displacement caused by bending moment stresses at the fracture zone. If the anomaly is included in the least-squares fit, the portion of the polynomial on the older side of the fracture zone slopes up towards the offset in order to accommodate the anomaly. This leads to an incorrect estimate of the form of the regional polynomial and to a reduced geoid offset. The effects of both horizontal heat conduction, and of anomalies adjacent to the fracture zone can be avoided by using an exclusion width of between 150 km and 200 km. There are limitations on the size of the exclusion width that can be used. The total length of the observed profile must be long enough to allow a large exclusion width while still retaining a sufficient number of endpoints to accurately estimate the regional field. On several of the Seasat profiles, the segment of usable profile between the Udintsev and Eltanin fracture zones is only 300-400 km long. In these cases, and in cases where neighboring tectonic features (e.g. other fracture zones, seamounts, etc.) limit the length of the geoid profiles, we have used a smaller exclusion width.

The geoid offset can be measured from profiles which contain signals at all wavelengths, or on profiles which have had a reference field removed. In both cases we assume that the computed polynomial approximates the regional geoid and the amplitude of the step function represents the regional offset. However, because the long wavelength geoid and the computed reference field cannot in detail be represented by second-order polynomials, the estimated geoid offsets are affected by the choice of profiles. In order to determine the magnitude of this effect, geoid offsets were estimated from both the full geoid profiles and from profiles which have had a reference field removed. The GEM 9 reference field with coefficients up to degree and order 10 was subtracted from the profiles which left anomalies having wavelengths less than approximately four thousand kilometers. For each profile across the Udintsev fracture zone, an exclusion width of 150 km was used. Across the Eltanin, a larger width of 200 km was used in order to span the closely-spaced Heezen and Tharp fracture zones.

The results of this analysis are shown in Figure 3. On the west limb of the Udintsev, the offsets estimated from profiles which have had the reference field removed are with a few exceptions larger than those estimated from the full profiles. For the youngest 12 profiles this difference averages 0.23 m whereas the remaining profiles vary by less than 0.12 m. On the east limb of the Udintsev the amplitude of the variations between the two sets of measurements are similar but in contrast to the western limb, the estimates from the full geoid profiles are larger than estimates from the profiles with the reference field removed. The differences in the youngest 8 profiles average 0.23 m and the remaining profiles except for the oldest vary by less than 0.14 m.

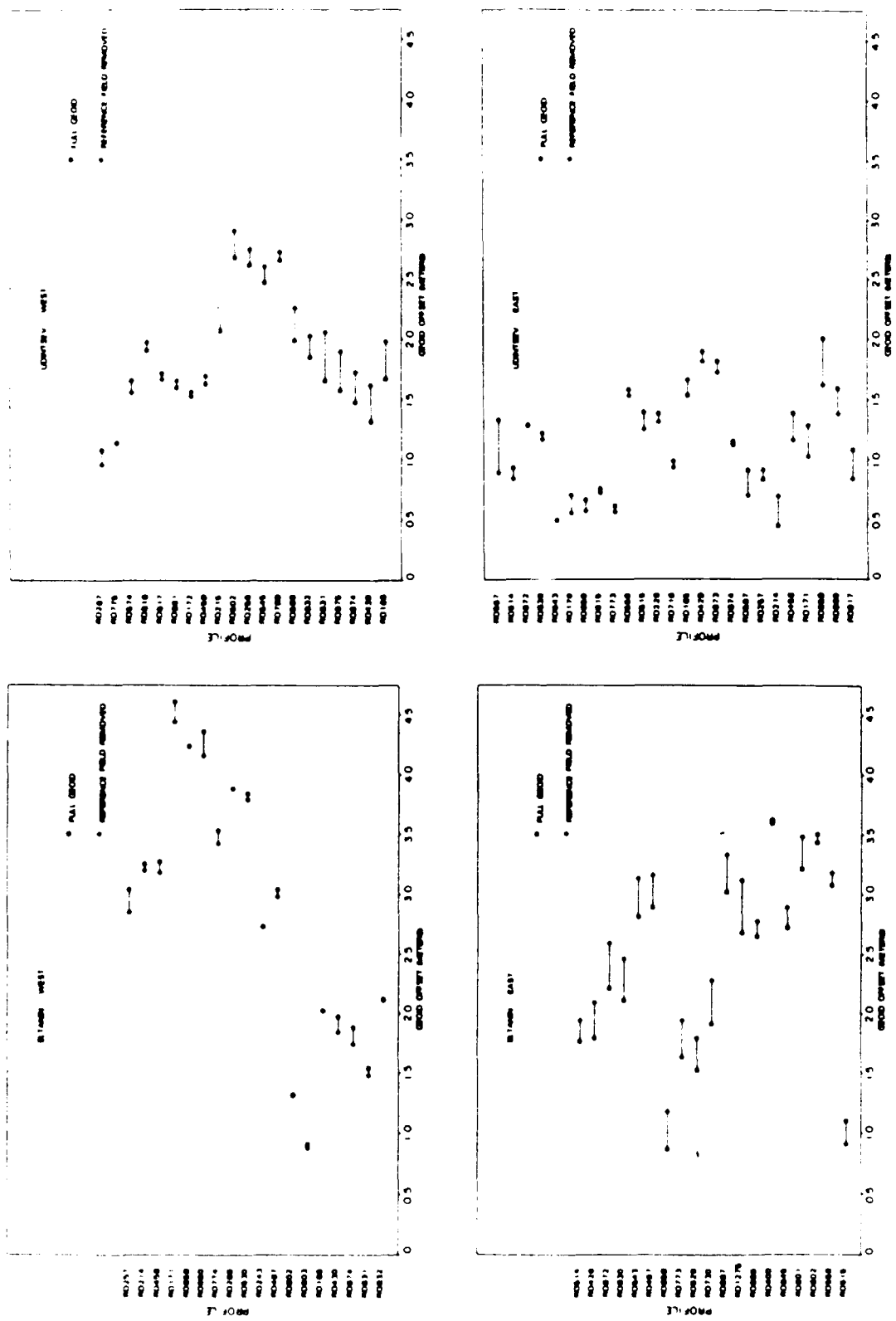


Figure 3 Geoid height offsets across the Eltanin and Udintsev fracture zones estimated from profiles with and without the GEM 9 reference field ( $l=m=10$ ) removed. An exclusion width of 150 km is used on all profiles across the Udintsev, and a width of 200 km across the Eltanin.

Offset determinations from the two sets of profiles across the western trace of the Eltanin are similar and vary on the average by only 0.07 m. In all cases, measurements from the full geoid profiles are slightly larger. In contrast, differences between the two sets of measurements across the eastern branch of the fracture zone are large. In all cases measurements from the profiles which have had the reference field removed are up to 0.38 m larger and on the average are 0.25 m larger than those estimated from the full geoid profiles.

The variations in geoid estimates obtained from the two sets of profiles are fairly consistent on each branch of the fracture zones but the magnitude of the deviations vary between the branches. On each limb of the fracture zones the deviations show up as a bias rather than as random errors. The effect of a variable magnitude bias on the measurements will change the observed trends of the geoid slope versus age curves slightly, but will significantly modify the overall amplitude, and hence, the plate thickness estimates. For these reasons, it is more useful to look at geoid slope estimates across each branch of the fracture zones separately in order to avoid scatter that may be caused by the observed biases and not by lithospheric thickness variations.

The choice of whether to use profiles with or without a reference field removed, therefore, appears arbitrary. Because the step arising from seafloor age variations is more prominent in profiles which have had a reference field removed and deviations from the estimated polynomial and observed geoid are easier to see, geoid offsets for this paper were computed from profiles with the reference field removed.

## Results:

The locations of Seasat track lines used in this analysis are shown in Figure 4. These profiles all show clear geoid offsets at the fracture zones without additional, unavoidable large anomalies elsewhere on the profiles. Conversely, profiles that were excluded contained additional anomalies which produced unreasonable estimates of the regional geoid. On each profile, exclusion widths of 0 km, 150 km and 200 km were investigated, and the largest exclusion width which gave a reasonable fit to the profiles was used. In many cases both the 150 km and 200 km widths gave reasonable estimates and the average of the two measurements was used as an estimate of the regional offset, and the variation between them as an estimate of the range of possible values. The error estimates in cases where only one exclusion width was chosen were determined visually. This visual estimate was in all cases equal to or larger than the calculated root-mean-square error between the observed and estimated profiles (calculated using only those segments of the profile used in the least-squares estimation). The calculated error in most cases was less than 10 cm whereas the difference in estimates of the regional offset based on different exclusion widths varied by as much as several tens of centimeters. The location of the profiles and the estimated regional offset and error is listed in Table 2.

Results from the Eltanin Fracture Zone System are shown in Figures 5a and 5b. The measurements from the east and west limbs of the fracture zone are presented separately in order to isolate any variations in the geoid slope-age relationship between the two sides. Also plotted are theoretical geoid slope-age curves for plate thicknesses of  $a=60$  km and 90 km, where geoid slopes are derived using the derivative of the long-wavelength

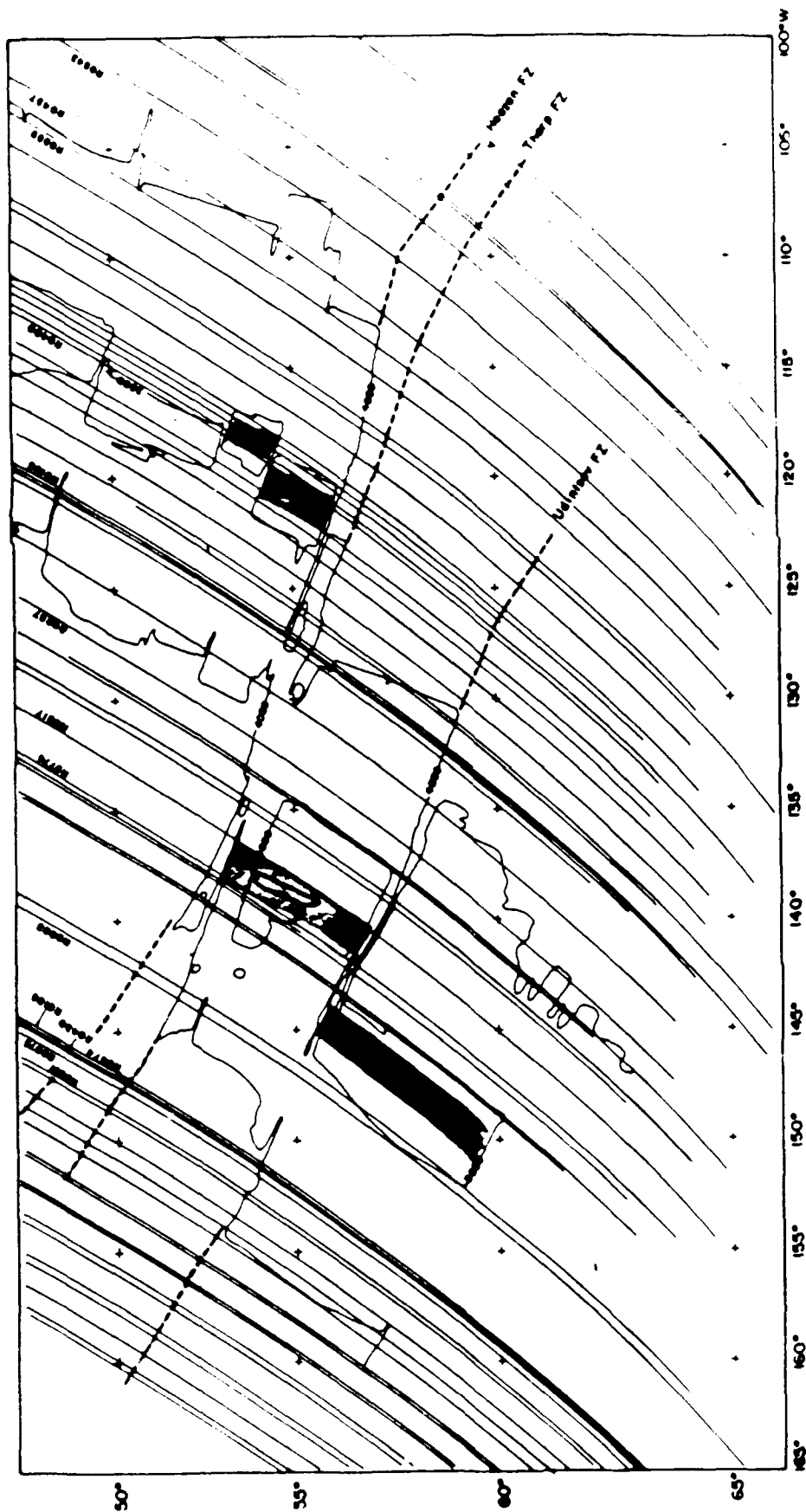


Figure 4 Location of Seasat tracks used in this paper. Identified tracks are profiles shown in Figures 2, 6, 7, 8 and 10.

isostatic approximation (equation 2) and are given by:

$$\frac{dN(t)}{dt} = \frac{4\pi G \rho_m \alpha T_m}{g} \left[ \sum_{n=1}^{\infty} (-1)^{n+1} \cdot \exp(-\beta_n u t/a) + 2w(t) \cdot \sum_{n=1}^{\infty} \exp(-\beta_{2n-1} u t/a) \right] \quad (6)$$

with  $\beta_n = [(-R^2 + n^2 \pi^2)^{1/2} - R]$ ,  $R = ua/2\kappa$ , and

$$w(t) = \frac{\alpha \rho_m T_m}{2(\rho_m - \rho_w)} \left[ 1 - 8/\pi^2 \sum_{n=1}^{\infty} 1/(2n-1)^2 \exp(-\beta_{2n-1} u t/a) \right] \quad (7)$$

Values for the thermal parameters used in the calculations are given in Table 1. The theoretical curves are used only as a reference to the expected decrease in geoid slope values for different plate thicknesses and are not intended to represent the best-fitting plate parameters.

It is clear that the observed geoid slope values do not follow a curve predicted by a single plate thickness. Instead, on the west side of the Eltanin there appears to be three separate segments that deviate from the theoretical curves; one for average ages less than 18 m.y., a second for ages between 18 and 40 m.y. and third for ages greater than 40 m.y. On the east side of the Eltanin two trends are seen, one for ages less than 40 m.y., and the other for ages greater than 40 m.y. It is useful to identify and compare profiles along critical segments of the fracture zone to see if the variations in the geoid slope-age plots are real or possibly caused by problems in the measurement technique. To do this comparison we have identified several profiles along the curves and plotted them together with their least-squares estimates of the regional geoid and the theoretical geoid based on a chosen plate thickness and the ages of the lithosphere across the fracture zone. The geoid profile across a fracture zone can be determined from a given temperature distribution and the long-wavelength, isostatic approximation to the geoid (equation 2). Using the temperature structure appropriate for the plate-cooling model



(equation 1) and placing the fracture zone at  $x=0$ , the geoid anomaly is given by:

$$N(t) = \frac{1}{2} [1 + \operatorname{erf}(\frac{x}{2\sqrt{\kappa t}})] \cdot \Theta(t) + \frac{1}{2} [1 - \operatorname{erf}(\frac{x}{2\sqrt{\kappa t}})] \cdot \Theta(t+t_0) \quad (8)$$

$$\text{with } \Theta(t) = \frac{4G\rho_m\alpha T_m a^2}{g\pi} \sum_{n=1}^{\infty} \frac{(-1)^{n+1}}{n^2} \cdot \exp\left(\frac{-n^2\pi^2\kappa t}{a^2}\right)$$

where  $t_0$  is the age offset of the fracture zone and  $t$  is the age of the younger seafloor. The functions  $\Theta(t)$  and  $\Theta(t+t_0)$  are the geoid relations far from the fracture zone and are 1-dimensional approximations to the full series solutions given in equations 6 and 7. At plate velocities appropriate to the Pacific-Antarctic Ridge there is little difference between the approximate and the full expressions. To compare the thermal plate estimate with the observed profile, the regional geoid calculated in the least-squares fitting routine is subtracted from the observed profile. In the figures where the theoretical and observed profiles are compared, the vertical position of the theoretical profile was adjusted so that the mean values of the geoid heights outside of the exclusion zone on both the observed and theoretical profiles coincided.

On the western side of the Eltanin, profiles R0817 and R0774 (Figure 5a) are located only 110 km apart but fall on different parts of the geoid slope-age curves. Profile R0817 lies more closely to the curve for a 110-120 km thick thermal plate whereas profile R0774 is more compatible with a 60-70 km thick plate. On comparing the estimated geoid offset and predicted geoid profiles based on the plate model with the observed geoid profiles (Figures 6a and 6b) it can be seen that the estimates of the regional geoid offset are reasonable and that the thermal plate thicknesses which can be used to fit these two profiles differ by 50-60 km. It is

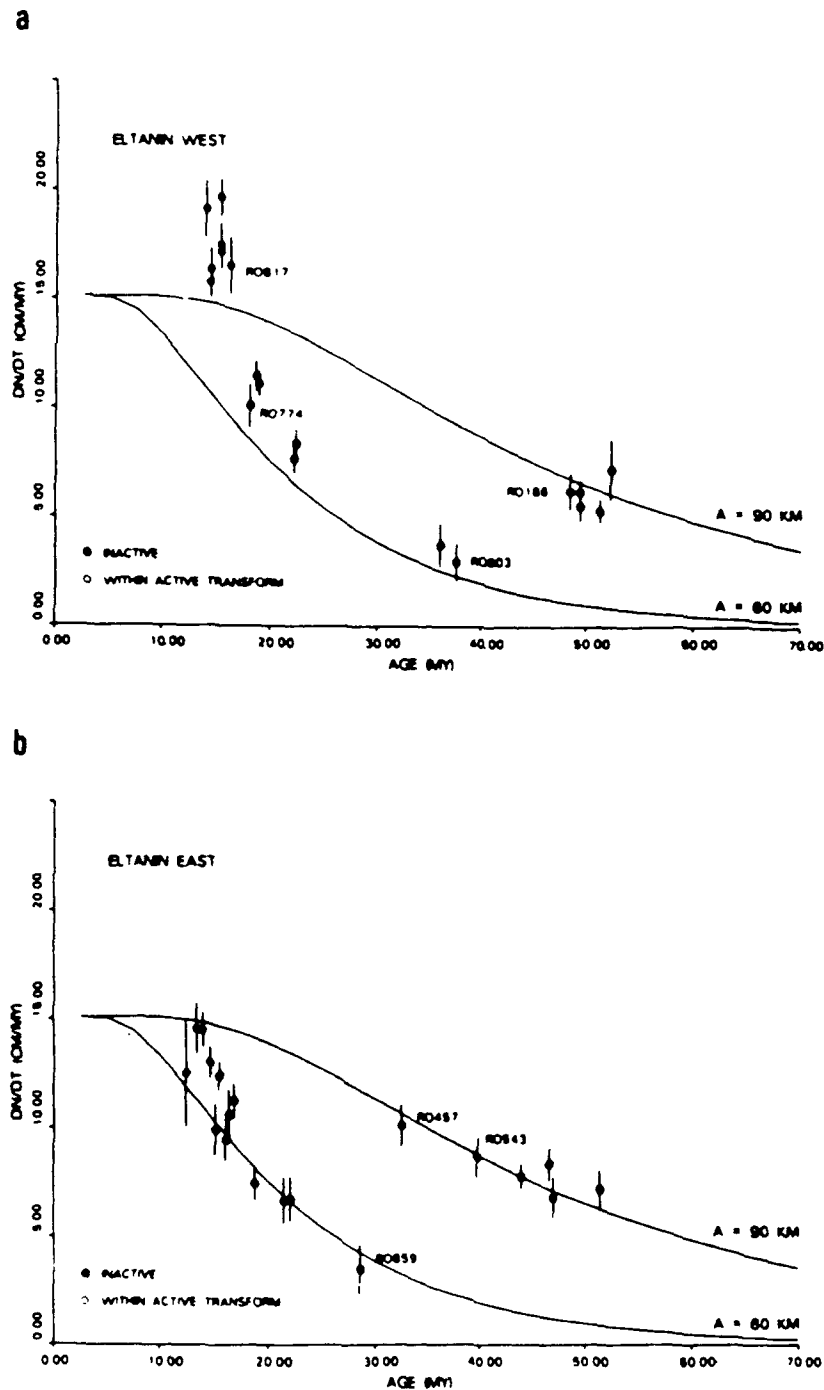


Figure 5 Geoid slope estimates across the Eltanin Fracture Zone System and theoretical geoid slopes calculated from a thermal plate cooling model with plate thicknesses of 60 km and 90 km.  
a) across the western (Antarctic) limb of the fracture zone b) across the eastern (Pacific) limb Figure 6 Geoid profiles across the Eltanin Fracture Zone System a) Geoid profiles with GEM9 reference field removed ( $l=m=10$ ), and estimated regional polynomial and offset. A 200 km exclusion width is used.  
b) Geoid profiles with the estimated regional polynomial removed, and theoretical geoid profiles for plate thicknesses of 120 km and 70 km.

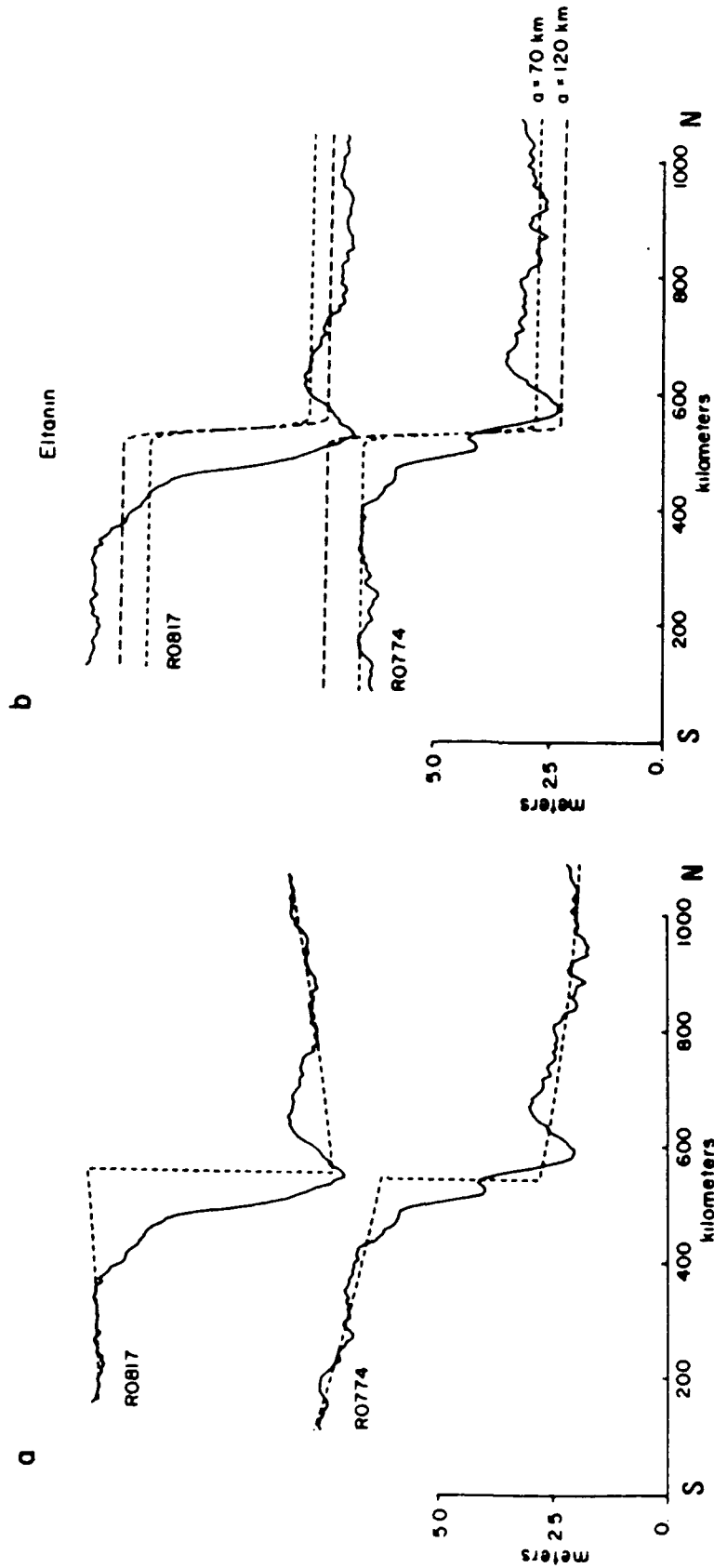


Figure 6 Geoid profiles across the Eltanin Fracture Zone System  
a) Geoid profiles with GEM9 reference field removed ( $l=m=10$ ), and estimated regional polynomial and offset. A 200 km exclusion width is used.  
b) Geoid profiles with the estimated regional polynomial removed, and theoretical geoid profiles for plate thicknesses of 120 km and 70 km.

interesting to note that profile R0774 is located slightly west of the active ridge crest segment between the Udintsev and Tharp fracture zones, and profile R0817 is slightly east of the ridge segment and crosses the active transform region. Within the active transform, the equation for geoid heights (equation 8) is not strictly valid. The initial conditions are set at the ridge-transform intersection and the lithosphere is assumed to be cooling at all other times. This criterion is not met within the transform zone. Far from the fracture zone, however, geoid heights calculated using equation 8 are valid.

Another two profiles which constrain the overall trends in the data are profiles R0803 and R0186 (Figure 5a) which are separated by 290 km. Profile R0803 lies at the older end of the segment of the geoid slope-age curve that is most compatible with the curve for a plate thickness of 60 km and profile R0186 is at the young end of the curve best-fit by a 90 km thick plate. The observed profiles and their least-squares estimates of the regional geoid and offset are shown in Figure 7a. As before, the observed minus the regional geoid, and the theoretical profiles for plate thicknesses of 60 and 90 km are shown in Figure 7b. Again, the least-squares estimates of the regional offset appear to be reasonable. Profile R0803 is very closely matched by the theoretical profile for a plate thickness of 60 km whereas profile R0186 is better fit by a profile calculated using a larger plate thickness of 90 km.

Finally, profiles R0859, R0457, and R0543 from the east side of the Eltanin are examined in the same manner. Profiles R0859 and R0457 are separated by only 80 km. The observed and calculated curves are shown in Figure 8 for plate thicknesses of 55 and 90 km. It is clear that profile R0859 displays an offset most compatible with a fairly thin plate thickness

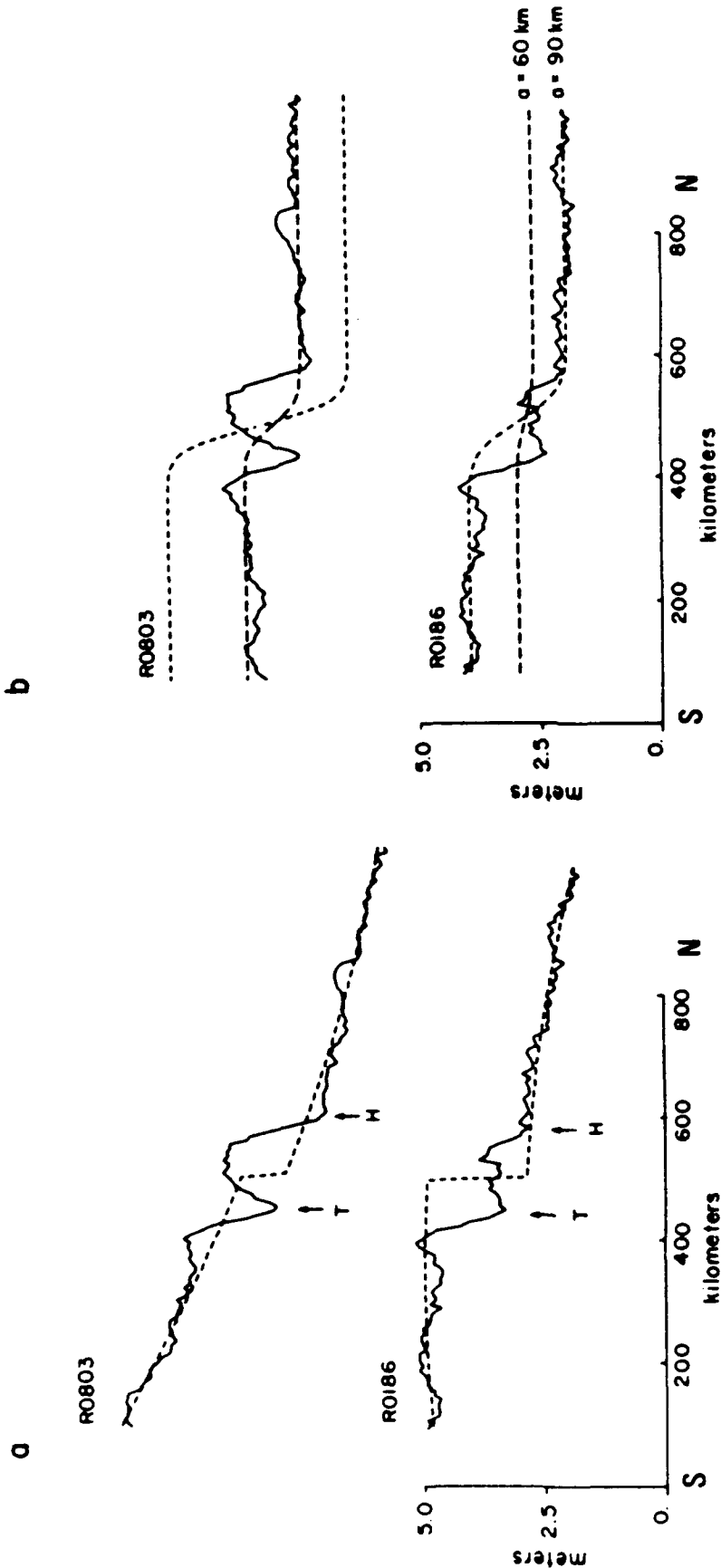


Figure 7 Geoid profiles across the Eltanin Fracture Zone System a) Geoid profiles with GEM9 reference field removed ( $l-m=10$ ), and estimated regional polynomial and offset. A 200 km exclusion width is used. T refers to the location of Thompson fracture zone, H to location of Heezen fracture zone. b) Geoid profiles with the estimated regional polynomial removed, and theoretical geoid profiles for plate thicknesses of 60 km and 90 km.

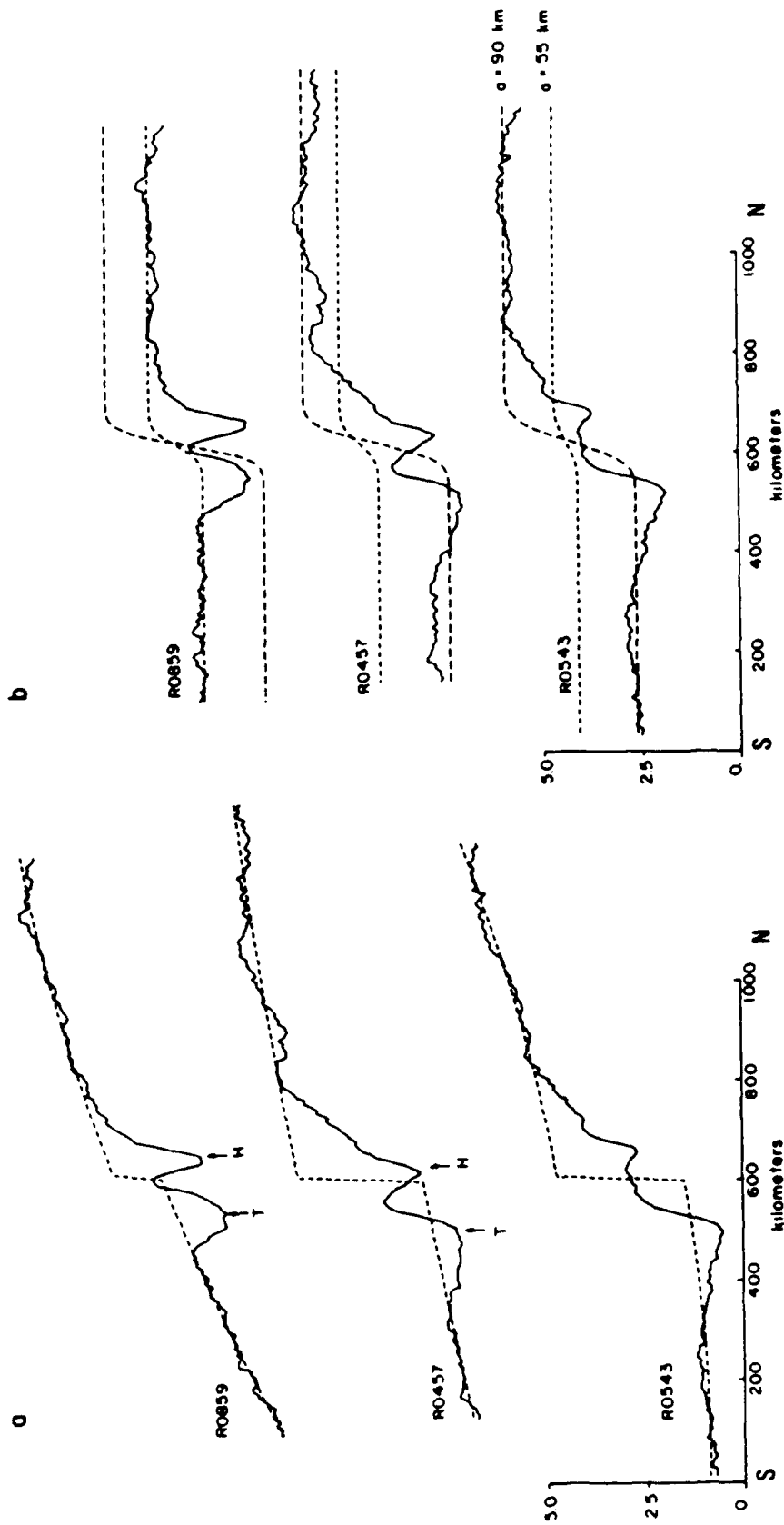


Figure 8 Geoid profiles across the Eltanin Fracture Zone System a) Geoid profiles with GEM9 reference field removed ( $l-m=10$ ), and estimated regional polynomial and offset. A 200 km exclusion width is used. b) Geoid profiles with the estimated regional polynomial removed, and theoretical geoid profiles for plate thicknesses of 55 km and 90 km.

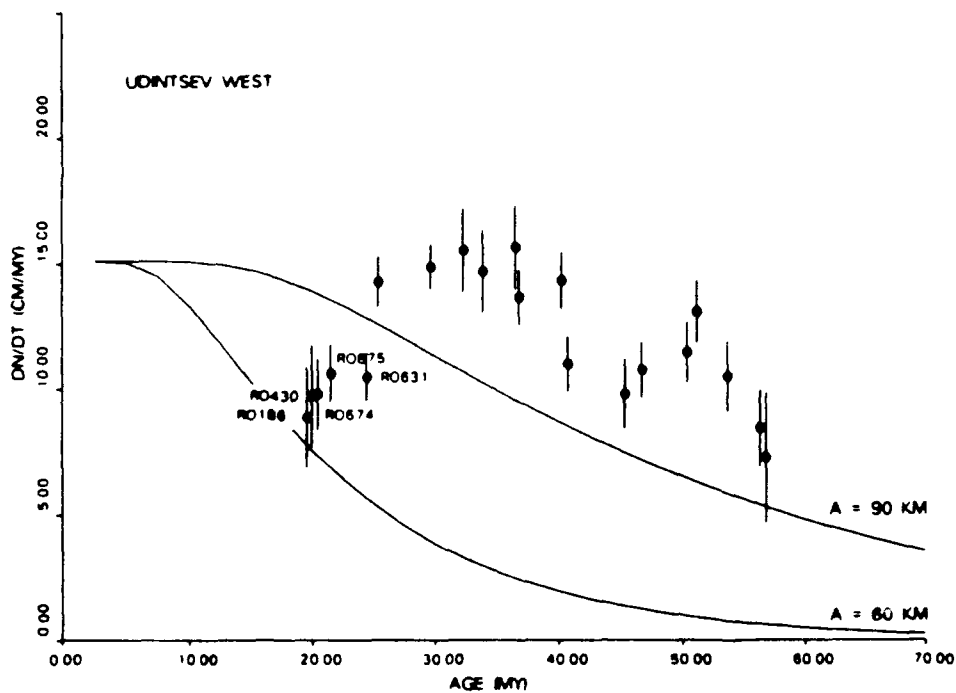
between 55-60 km. Profiles R0457 and R0543 on the other hand, are better matched by a larger plate thickness of around 90 km.

The large deviations in the estimated geoid slopes for profiles located very near each other on the Eltanin Fracture Zone system appear to be real and not a result of errors in the measurement technique. The geoid slope-age relationship on both sides of the fracture zone is similar although not identical (Figures 5a and 5b), with major differences occurring primarily at ages less than 15 m.y.

The geoid slope-age relationship is not as consistent across the two sides of the Udintsev fracture zone as it is across the Eltanin (Figures 9a, 9b). On the west side of the Udintsev, geoid profiles with average ages of less than 17 m.y. contain large anomalies near the fracture zone on the older seafloor, and the geoid offset also increases very gradually towards the younger side although for these young seafloor ages an abrupt increase would be expected. Geoid offset estimates from these profiles show no systematic increase as the exclusion width is increased and on most profiles the offset determinations change erratically as the exclusion width is varied. These profiles were not considered to be reliable and were not included in the geoid slope analysis. Between 20 and 35 m.y. an increase in the geoid slope values with age is apparent. For ages greater than 35 m.y., the geoid slope estimates decrease gradually, consistent with a plate thickness of 100-120 km.

The increase in geoid slopes for average ages between 20 and 35 m.y. on the west side appears to be real and not a result of errors in the estimation technique. Figure 10 shows the five profiles between 20 and 25 m.y. along with estimated regional offsets determined using exclusion widths of 100 and 200 km. Although the younger, southern side of the

a



b

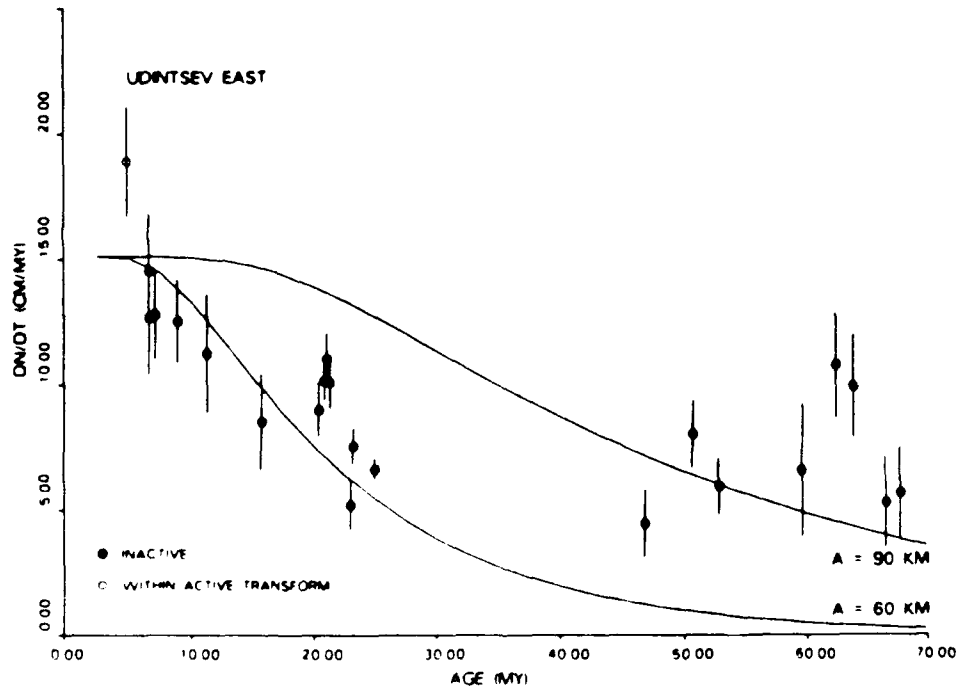


Figure 9 Geoid slope estimates across the Udintsev Fracture Zone and theoretical geoid slopes calculated from a thermal plate cooling model with plate thicknesses of 60 km and 90 km. a) across the western limb of the fracture zone b) across the eastern limb



profiles are adequately determined by the estimated polynomials, the regional field on the northern side is difficult to estimate because of the large anomaly adjacent to the fracture zone. The anomaly is up to 200 km wide and 1 m high. As before, the regional field has been removed and the offset compared with those predicted for theoretical plate thicknesses of 60 and 90 km. The 3 younger profiles, R0186, R0430 and R0674, are more closely fit by a theoretical plate thickness less than 90 km. The older profiles, R0275 and R0631, however, are better fit by a 90 km thick plate.

On the east side of the Udintsev there is a gap in the data between average ages of 30 and 45 m.y. (Figure 9b). Profiles within this region contain large anomalies on the older side of the Udintsev with amplitudes of approximately 1.0 m and widths up to 200 km. In addition, the northern baseline is extremely short because of a similar anomaly on the older side of the Eltanin. An exclusion width that is sufficiently large to avoid the anomaly adjacent to the Udintsev cannot be used because the northern side of the fracture zone then becomes unconstrained in the polynomial determination. For ages younger than 30 m.y. the geoid slope estimates follow the trend defined by a plate thickness between 50-70 km. For ages greater than 45 m.y. the scatter is large and it is difficult to ascertain the overall trend of the geoid slope values. For example, if the older two measurements were removed, geoid slope values would appear to increase with increasing age, contrary to what is theoretically expected. Likewise, if we disregard the two largest geoid estimates, then a decrease in geoid slopes would be perceived. Unfortunately, with the data available, little can be said about the general trend of geoid slope values at these older ages, although the continued presence of a geoid offset in the profiles strongly suggests that thermal and bathymetric affects persist across the

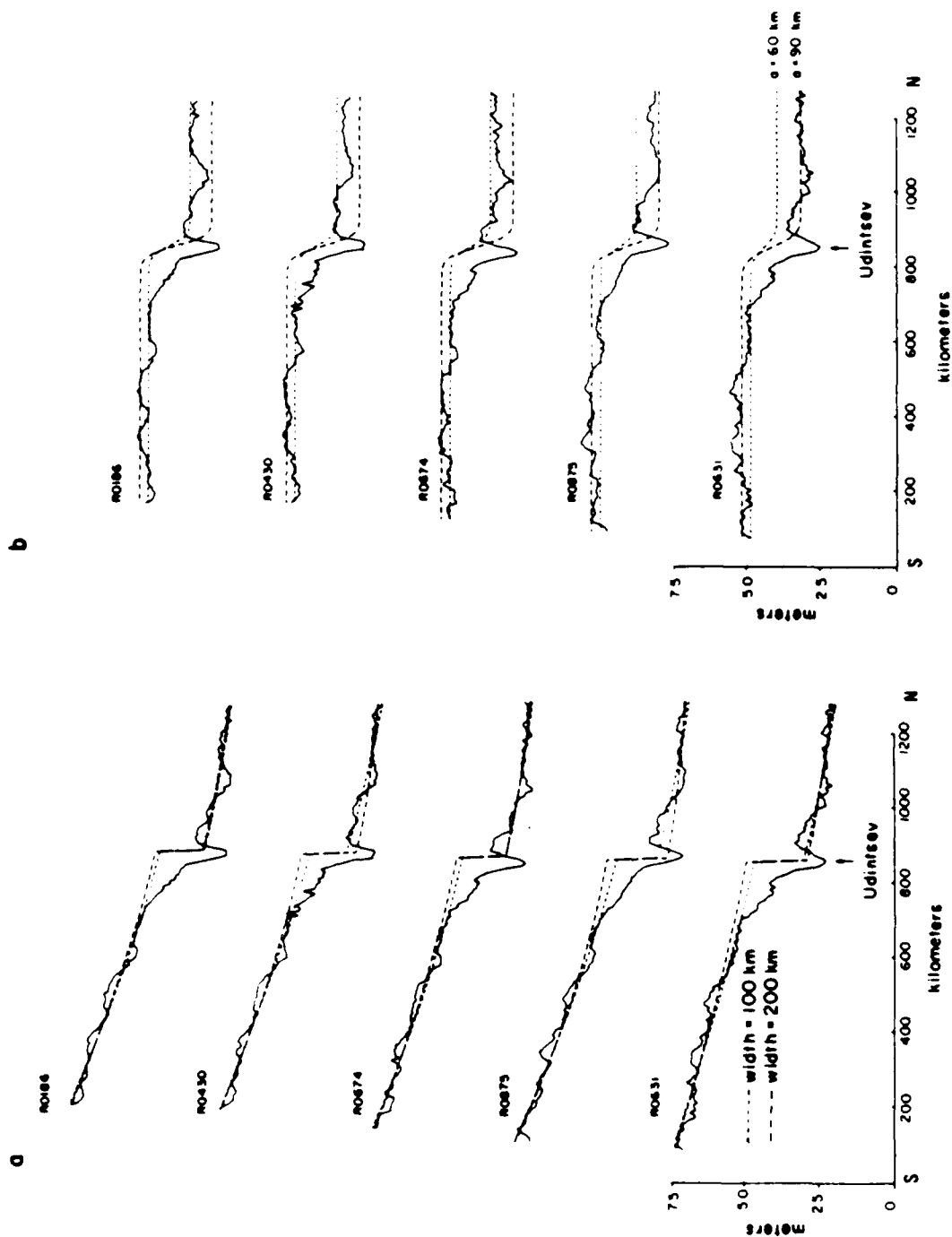


Figure 10 Geoid profiles across the Udintsev Fracture Zone a) Geoid profiles with GEM9 reference field removed ( $l-m=10$ ), and estimated regional polynomial and offsets determined using exclusion widths of 100 km and 200 km. b) Geoid profiles with the estimated regional polynomials removed compared to theoretical geoid profiles calculated for plate thicknesses of 60 km and 90 km.

fracture zone. For this to be true the plate thickness must be larger than 60 km. Geoid slope values for average ages greater than 50 m.y. all lie near or above the theoretical curves defining geoid slopes for a 90 km thick plate.

Across the east and west limbs of the Eltanin and across the east limb of the Udintsev, geoid slope estimates decrease rapidly for ages less than 35 m.y. and then increase over a relatively short time and distance interval. This is followed by a less rapid decrease as the age of the seafloor increases. By comparing the estimated geoid offsets and theoretical geoid offset profiles with selected geoid profiles that fall on critical sections of the geoid slope versus age plots we have shown that the observed trends are real and not caused by unreasonable estimates of the geoid offsets. The geoid slope versus age plot for the western limb of the Udintsev differs from the other plots and shows an increase in geoid slope estimates for ages between 20 and 35 m.y. followed by a gradual decrease for increasing average ages. North of the western limb of the Udintsev fracture zone, the Eltanin fracture zone system is replaced by the Louisville Ridge which is composed of discrete seamounts and ridges aligned along a trend similar to that of the Eltanin fracture zone system [15]. Although we have not crossed the summits of any seamounts with the northern baselines of our analyzed profiles, they may still affect the regional geoid offset because the excess mass of the seamount deflects the oceanic lithosphere and creates a surrounding moat. Both the flexed lithosphere and the excess mass of the seamount contribute to the regional geoid; the magnitude of the affect depending on the size and compensation of the seamount. Because of this variability, it is not simple to predict the affects of the Louisville Ridge on estimates of the regional geoid offsets, but it is likely that they are affected to some extent.

## Discussion:

The geoid slope measurements across the Udintsev Fracture Zone and the Eltanin Fracture Zone System are not consistent with the thermal plate cooling model. Segments of the observed geoid slope versus average age curves from the Eltanin closely follow theoretical curves for a 60 km plate cooling model (10-35 m.y.) and a 90 km thick plate (35 m.y.-60 m.y.) although a single plate thickness cannot account for the entire set of measurements. Similar results have been found in the South Atlantic across the Ascension fracture zone where geoid slopes also show two distinct trends [16]. For ages less than 30 m.y., the geoid slopes decrease rapidly, consistent with a thin, 50-75 km thermal plate. At older ages, they rapidly increase in magnitude and then decrease more slowly, consistent with a thicker plate (75-100 km).

Any proposed cooling model must satisfy both the geoid slope and seafloor depth observations. In the South Pacific the mean depth versus age curve for seafloor ages less than 80 m.y. is proportional to the square root of age and can be approximated by the empirical formula [2]:

$$w(t) = 2681 + 337/\sqrt{t} \quad (t \text{ in m.y.}) \quad (9)$$

At ages greater than 80 m.y. the depth versus age curve flattens out, consistent with a finite plate thickness [9]. The minimum plate thickness necessary to match the observed depths out to 80 m.y. would be 120 km. At 80 m.y. the depth predicted by a 120 km thick plate is shallower than the empirical curve by ~200 m which is within the scatter in the data. Plate thicknesses less than this will predict even shallower depths.

A 60 km thick plate for seafloor ages less than 35 m.y. (as derived from the geoid slope estimates), therefore, cannot accurately predict seafloor depths for these ages. Comparing calculated depths from the plate

cooling model to the empirical depth curve (from equation 9) shows that by 35 m.y., the plate model predicts depths up to 370 m shallower than the empirical depth curve (Figure 11). If a plate thickness of around 90 km is postulated for older seafloor, again based on the geoid-slope curves, the deviations between the predicted curve based on the plate model and the observed seafloor depths become increasingly larger with age. Comparing these results with the depth anomaly map for the South Pacific [2] does not reveal a progressive increase in the depth anomalies with distance from the ridge crest. A +600 m anomaly is seen over the western limb of the Eltanin, corresponding to the Louisville Ridge, but except for isolated +400 m depth anomalies near 90°W, 60°S, the eastern limb has only minor depth anomalies on the order of 0-200 m. Seafloor depths, then, do not support the existence of a thin plate (60-90 km) as an explanation for the observed geoid slope versus age relationship.

Seafloor depths north of the Eltanin subside at a slightly faster rate than depths south of the fracture zone [2, 9]. Geoid heights have also been observed to decrease at different rates north and south of the Eltanin [17] although these observations are difficult to interpret in the presence of long-wavelength anomalies and are thus less reliable evidence of a change in effective thermal plate thickness across the fracture zone. If, however, these differences in subsidence rate and geoid slopes are caused by such a change then the expected form of the geoid-slope versus age relationship measured across the Eltanin would also change. We can look at possible behaviours of the geoid offset by assuming a very simplistic model in which lithosphere north of the Eltanin is characterized by a 120 km thick thermal plate and by a 100 km thick plate south of the fracture zone.

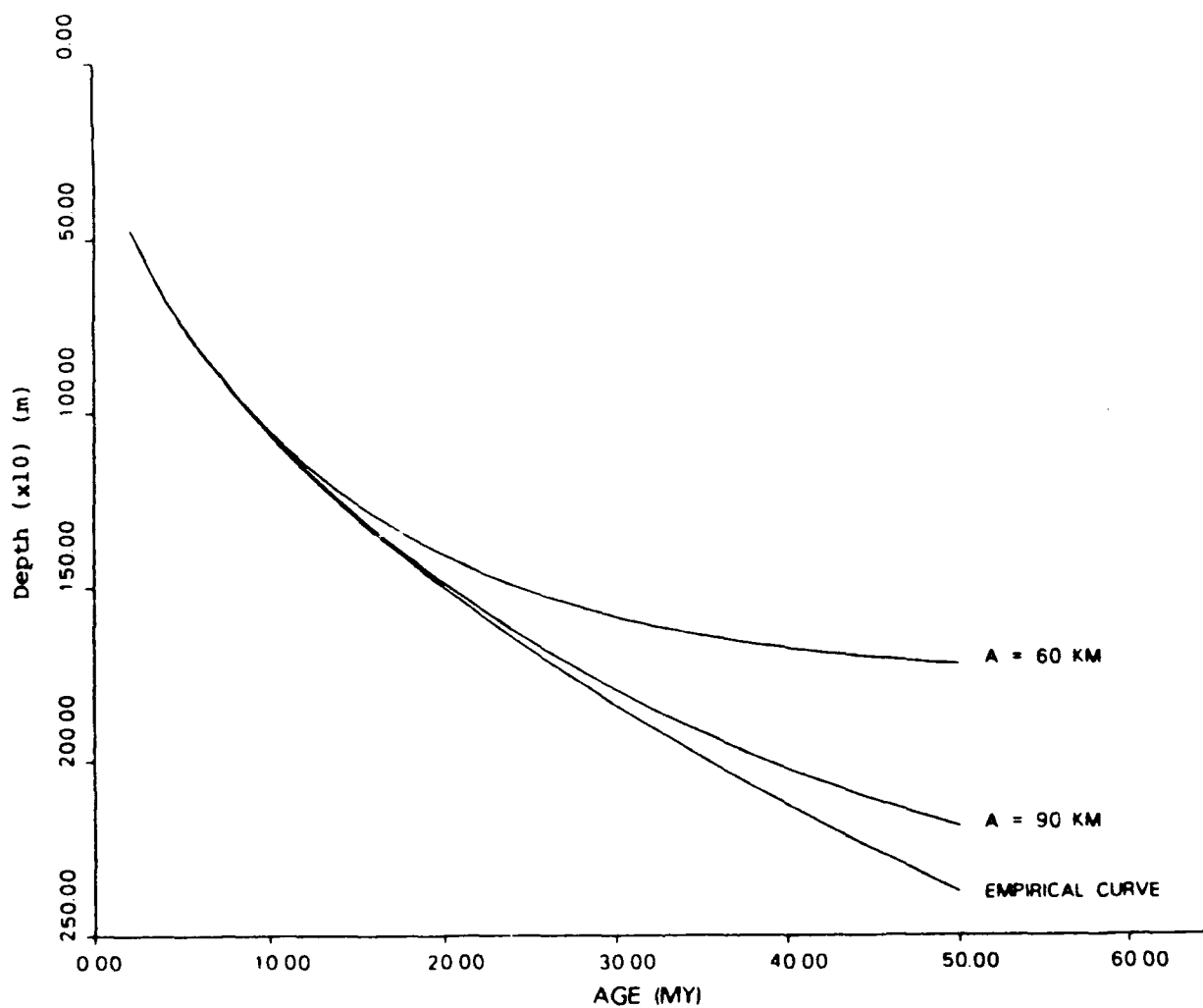


Figure 11 Depth curves calculated from the thermal plate cooling model assuming plate thicknesses of 60 km and 90 km, and the empirical depth curve for the South Pacific determined by Schroeder (2)

The initial height of the geoid at both ridges is assumed to be identical which generally will not be the case in the presence of long-wavelength noise (signals unrelated to conductive cooling). With these assumptions, the calculated geoid heights and geoid slopes are shown in Figures 12a and 12b. The geoid slope versus age relationship differs across the two limbs of the fracture zone and for different values of the age offset. Assuming a right-lateral offset, geoid slopes decrease quickly across the eastern limb of the fracture zone, then change sign at large enough ages. This occurs when geoid heights on the thinner plate reach their equilibrium value and the geoid heights associated with the thicker plate continue to decrease below this value. In contrast, geoid slopes across the western limb of the fracture zone initially decrease and then increase until reaching a constant value. At large enough ages the geoid heights across each limb of the fracture zone reach constant values and geoid slopes then remain constant through time. Although at large ages the magnitude of the geoid slopes will be the same across both limbs of the fracture zone, their signs will be opposite. These predicted geoid slopes are not observed across the Eltanin (Figures 5a and 5b) where both limbs of the fracture zone display trends which are remarkably similar. Deviations from the theoretical geoid slopes that are observed in the measurements across the Eltanin cannot be explained by a sudden discontinuity in plate thickness across the fracture zone. The model used in this comparison is extremely simplified, however, and changes in effective plate thickness across the Eltanin cannot be completely discounted.

An important contribution to the observed geoid anomalies which we have not considered in our analysis may come from small-scale convection. Such convection occurs beneath the rigid, cooling lithosphere on scales much

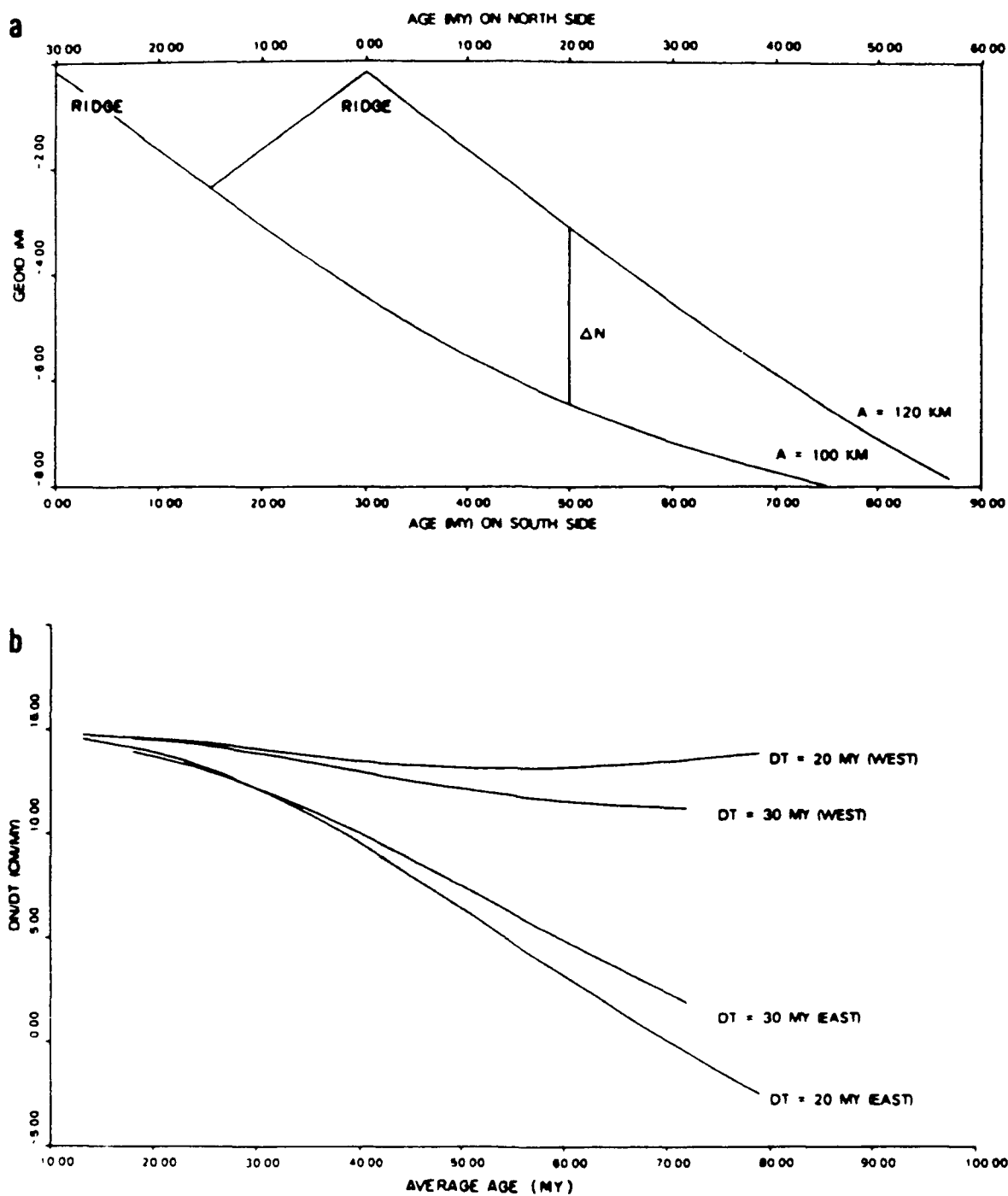


Figure 12 a) Theoretical geoid height values for plate thicknesses of 100 and 120 km. b) Geoid slope estimates across a fracture zone assuming a 120 km thick plate north of the fracture zone and a 100 km thick plate to the south. Geoid slope estimates for offsets of 20 m.y. and 30 m.y. are shown.



smaller than the dimensions of the oceanic plates. Numerical experiments on the onset time and development of small-scale convection beneath cooling oceanic lithosphere [18, 19] do not predict rapid changes in the geoid slope-age relationship and cannot explain the relatively rapid changes in geoid slope we observe on profiles separated by less than a few hundred kilometers. The type of convection modeled above is instigated by small instabilities in the temperature structure of the cooling lithosphere. At a fracture zone, however, a large, horizontal gradient exists between the older, thicker and cooler lithosphere and the younger, hotter lithosphere. This horizontal gradient drives a flow that eventually develops into a cold downwelling plume beneath the older lithosphere and an upwelling plume beneath the younger portion [20, 21]. Shear coupling then causes a series of convecting cells to develop to the sides of the circulation beneath the fracture zone. The normal stresses and temperature anomalies arising from the convection will produce short-wavelength geoid and depth anomalies at the fracture zone. Although it is not clear how convection at a fracture zone will affect the depth-age or geoid-age relations, the presence of the anomalies will significantly change the measured geoid offset at the fracture zone when the offsets are measured with the same method as used in this paper [21]. Robinson et al. [21] have shown that after the development of convection there are relatively rapid changes in the estimated geoid offsets. The magnitude of these changes and the estimated geoid-slope versus age curves vary with changes in the parameters of the convection models (e.g., viscosity structure, Rayleigh number, etc.). These results suggest that although the method used in this paper to estimate geoid offsets avoids anomalies within several hundred kilometers of the fracture zone, the measured geoid offsets may still be contaminated by anomalies unrelated to the mean, regional geoid offset.

At this point, additional studies on the geoid-slope versus age relationship are necessary in order to determine the exact form of this relationship. At fracture zones, anomalies caused by flexure, bending stresses, and possibly small-scale convection, and the limited length of the geoid profiles to each side of the fracture zones make it difficult to accurately determine the regional geoid offset. Likewise, we have already noted that measuring geoid heights directly as a function of age is extremely difficult because of the presence of large amplitude anomalies which are unrelated to the cooling of the lithosphere.

In conclusion we have determined the geoid-slope versus age relationship across the Eltanin and Udintsev fracture zones and have found consistent relationships across three of the four fracture zone limbs. Our results suggest that although the simple plate cooling model accurately predicts seafloor depths to ages at least as old as 80 m.y. B.P., the more sensitive geoid anomalies reveal inadequacies in the predictive ability of the cooling model. Additional, unmodeled affects such as small-scale convection may be affecting the observed geoid offsets.

#### Acknowledgements

Many thanks to E. M. Robinson for reviewing an early draft of this manuscript and A. P. Freedman for help in computer program development. This research was supported by ONR Contract N00014-86-k-0325 to MIT. M. L. Driscoll gratefully acknowledges the support provided by the M.I.T Department of Earth, Atmospheric, and Planetary Sciences during part of 1986.

## Bibliography

- 1 B. Parsons and J.G. Sclater, An analysis of the variation of ocean floor bathymetry and heat flow with age, J. Geophys. Res. 82 (1977) 803-827.
- 2 W. Schroeder, The empirical age-depth relation and depth anomalies in the Pacific Ocean basin, J. Geophys. Res. 89 (1984) 9873-9883.
- 3 B. Parsons and D. McKenzie, Mantle convection and the thermal structure of the plates, J. Geophys. Res. 83 (1978) 4485-4496. 4 R. S. Detrick, An analysis of geoid anomalies across the Mendocino fracture zone: Implications for thermal models of the lithosphere, J. Geophys. Res. 86 (1981) 11751-11762.
- 5 D. T. Sandwell and G. Schubert, Geoid height-age relation from Seasat altimeter profiles across the Mendocino fracture zone, J. Geophys. Res. 87 (1982) 3949-3958.
- 6 A. Cazenave, B. Lago and K. Dominh, Thermal parameters of the oceanic lithosphere estimated from geoid height data, J. Geophys. Res. 88 (1983) 1105-1118.
- 7 A. Cazenave, Thermal cooling of the oceanic lithosphere: New constraints from geoid height data, Earth Plan. Sci. Lett. 70 (1984) 395-406.
- 8 A. Cazenave, Two distinct trends for cooling of the oceanic lithosphere, Nature 310 (1984) 401-403.
- 9 P. Molnar, T. Atwater, J. Mammerrickx and S.M. Smith, Magnetic anomalies, bathymetry and the tectonic evolution of the South Pacific since the late Cretaceous, Geophys. J. R. astr. Soc. 40 (1975) 383-420.
- 10 J. L. LaBreque, D.V. Kent and S.C. Cande, Revised magnetic polarity time scale for Late Cretaceous and Cenozoic time, Geology 5 (1977) 330-335.
- 11 W. F. Haxby, Gravity field of the world's oceans (map) (Lamont-Doherty Geological Observatory, Palisades, N.Y.) U.S. Navy, Office of Naval Research, 1985.
- 12 S. T. Crough, Geoid anomalies across fracture zones and the thickness of the lithosphere, Earth Planet. Sci. Lett. 44 (1979) 224-230.
- 13 D. Sandwell, and G. Schubert, Lithospheric flexure at fracture zones, J. Geophys. Res. 87 (1982) 4657-4667.
- 14 E. M. Parmentier, and W.F. Haxby, Thermal stresses in the oceanic lithosphere: Evidence from geoid anomalies at fracture zones, J. Geophys. Res. 91 (1986) 7193-7204.

- 15 A. B. Watts, R. A. Duncan and R. L. Larson, The origin of the Louisville Ridge and its relationship to the Eltanin Fracture Zone System, J. Geophys. Res. (submitted 1986).
- 16 A. P. Freedman and B. Parsons, Geoid anomalies over two South Atlantic fracture zones, (in preparation, 1987).
- 17 J. A. Andrews, W.F. Haxby and W.R. Buck, Regional variations along ridge crests: Geoid height, depth to ridge crest, and geoid height-age relationship, Trans., Am. Geophys. Union 67 (1985), 356.
- 18 W. R. Buck, When does small-scale convection begin beneath oceanic lithosphere?, Nature 313 (1985) 775-777.
- 19 W. R. Buck, and E.M. Parmentier, Convection beneath young oceanic lithosphere: Implications for thermal structure and gravity, J. Geophys. Res. 91 (1986) 1961-1974.
- 20 C. H. Craig and D. McKenzie, The existence of a thin low-viscosity layer beneath the lithosphere, Earth Planet. Sci. Lett. 78 (1986) 420-426.
- 21 E. M. Robinson, B. Parsons and M. L. Driscoll, The effect of a shallow low viscosity zone on the mantle flow and geoid anomalies at fracture zones, submitted to Geophys. J. R. astr. Soc., 1987.

Table 1

Parameter	Definition	Value
$\alpha$	volume coefficient of thermal expansion	$3.1 \times 10^{-5} \text{ }^{\circ}\text{K}$
$g$	mean acceleration of gravity	$9.82 \text{ m s}^{-2}$
$G$	gravitational constant	$6.67 \times 10^{-11} \text{ m}^3\text{kg}^{-1}\text{s}^{-2}$
$\kappa$	thermal diffusivity	$8.0 \times 10^{-7} \text{ m}^2 \text{ s}^{-1}$
$\rho_m$	mantle density	$3330 \text{ kg m}^{-3}$
$\rho_w$	seawater density	$1025 \text{ kg m}^{-3}$
$T_m$	mantle temperature	$1365 \text{ }^{\circ}\text{C}$

## Chapter 5. Summary and Conclusions

## SUMMARY AND CONCLUSIONS:

### 5.1 Correlation between seafloor topography and the geoid

Altimeter data in combination with bathymetry and magnetic data have allowed us to study the tectonic fabric and thermal structure of oceanic lithosphere in the South Pacific and Southwest Indian Oceans. In the Southwest Indian Ocean, seafloor topography is shown to be highly correlated with short-wavelength geoid anomalies. At fracture zones, the thermal offset produces a geoid offset which is antisymmetric about the fracture zone valley. The maximum in the gradient of this geoid signal, however, is not coincident with the fracture zone valley because of the superposition of short-wavelength anomalies caused by the valley and linear ridges parallel to the fracture zone. Instead, maxima in the geoid gradient are offset 10-30 km from the deepest point of the valley but continue to follow the trends of the fracture zones. Thus, they can be used as indirect measures of the overall tectonic fabric. The fracture zone valley is correlated with a local minimum in the geoid that is approximately 30-50 km wide and 0.5-1.0 m deep. These minima are difficult to identify because of their small signal size, but are the most accurate means of locating fracture zone axes. Spreading ridge median valleys are also highly correlated with short- and intermediate-wavelength geoid anomalies and can be easily identified in the altimeter data. The median valley is located directly beneath a pronounced local minimum in the geoid that is superimposed on the broader geoid high caused by the occurrence of young, hot lithosphere at the ridge crest.

In the first study, an elastic plate model was used to match the observed, short-wavelength geoid anomalies. For fracture zone topography near the ridge crest-transform fault intersection, a plate thickness of around 10-20 km produces the most reasonable geoid estimates. This value is a very loose approximation because both the bathymetry profiles used to compute the geoid and the geoid profiles are interpolated from grids of bathymetry or geoid heights which are also interpolated data. This was necessary because Seasat tracks and bathymetry along ship-tracks do not coincide unless the research goal of the expedition was to follow a satellite path. Improvements on this study would require new data and could follow either of two approaches. Scientific cruises could be undertaken to gather bathymetry beneath satellite tracks. Concurrent gravity profiles could also be collected for their short-wavelength content, with the geoid profiles used for the longer wavelengths. Alternatively, if extremely dense coverage of the ocean surface elevation by another satellite were available, this could be interpolated onto profiles coincident with existing bathymetric lines. This second alternative is more attractive because of the huge amount of ship time and human effort necessary to collect individual bathymetric tracks. Although not yet available to the public, the Geosat satellite coverage may be sufficiently dense for this second alternative to be used.

## 5.2 Plate reconstructions using Seasat altimetry

Using the information on correlations between topography and the geoid derived from the first study, fracture zone and ridge crest crossings were identified, where possible, and used to delineate the



present-day plate boundary and theoretically, the configuration of past plate boundaries. This information is used in conjunction with magnetic anomaly locations to derive instantaneous and finite poles of rotation and rotation angles. The poles derived here for present-day plate motions and for anomaly 6 are similar to previously published poles based on smaller data sets and/or different methods for calculating pole positions. This indicates that the previous poles were well-located and the addition of fracture zone information does not significantly improve the results. The pole for anomaly 13 is significantly different from a previous pole determination (Fisher and Sclater, 1983) and matches the observed trends of most fracture zones more closely. A few fracture zone trends are not closely matched, however, and it is not conclusive that the pole derived here cannot be determined more precisely given additional magnetic anomaly lineations. The pole for anomaly 20 is interesting in that it is very close to a published pole location based solely on magnetic data (Royer et al., 1987), some of which were not used in this study, and does not match another pole position that was based on a combination of magnetic and fracture zone lineations (Fisher and Sclater, 1983). The question of confidence limits for these poles remains unanswered in this study and makes comparisons with previously published poles difficult. To the extent that flowlines determined from the poles match observed fracture zone trends, the poles determined in this study predict these trends more accurately. This is only true where the differences are large; for many of the eastern fracture zones differences in the alternative models are minor. A comprehensive study of the errors in the computed pole positions is necessary in order to determine the validity of these poles.

A major realization in this study is the difficulty in locating fracture zone crossings during a particular time period for a single fracture zone on both sides of the spreading ridge. For many reasons, the fracture zone geoid signal is often apparent only on one of the two plates. For the method used in this study, identifications from both plates are necessary, and information where available on only one plate is not used. As discussed more fully in Chapter 3, a method such as that developed by Shaw (1987) utilizes the Seasat data more fully and is not dependent on visual identifications of fracture zone crossings. The Southwest Indian Ridge appears to be an ideal area in which to apply such an inverse technique and the results would be extremely valuable. In such a study, confidence limits on pole positions would again be necessary in order to discriminate objectively between alternative hypotheses for African/Antarctic plate motion.

### 5.3 Thermal evolution of oceanic lithosphere

The geoid slope measurements across the Udintsev and Eltanin fracture zones are found to be inconsistent with the thermal plate cooling model. Segments of the observed geoid slope versus average age curves from the Eltanin closely follow theoretical curves for a 60 km plate cooling model (10-35 my) and a 90 km thick plate (35-60 my) although a single plate thickness cannot account for the entire set of measurements. For ages less than 30 my, the geoid slopes decrease rapidly, consistent with a 50-75 km thick thermal plate. At older ages, they rapidly increase in magnitude and then decrease more slowly, consistent with a thicker plate (75-100 km). The inconsistencies between the observed relationships and proposed cooling models indicates

the need for more accurate descriptions of lithospheric cooling, and a better understanding of the thermal structure at fracture zones.

This study succeeds in characterizing the geoid offset versus age relationship at two fracture zones in the South Pacific. Although the sampling of the fracture zones by altimeter profiles is fairly uniform, improvements could be made by filling in some of the more critical areas with additional altimeter profiles when they become available. More critical are similar analyses on other fracture zones to verify the existence of this pattern on a larger scale and to determine whether the pattern is representative of oceanic lithosphere in general, or particular to the South Pacific

One problem that surfaced was the differences in estimated offsets when profiles with or without a reference field removed were used. The observed discrepancies are most likely a result of the assumption that the regional field is well-approximated by a second-order polynomial. A resolution of these discrepancies could shed light on better techniques for measuring geoid offsets.

The results from this section may be related to the presence of small-scale convection at fracture zones. This type of convection is initiated by the horizontal temperature gradient perpendicular to the fracture zone and would substantially alter the temperature structure from that predicted by purely conductive cooling. Theoretical modeling of this convection and analysis of the resulting geoid anomalies indicates that rapid fluctuations in the measured geoid offset can be produced using particular combinations of layer thicknesses and viscosities (Robinson et al., 1987,. At this time, however, the viscosity of the mantle is poorly known and the applicability of these

models remains to be proven. Obviously, the cooling of the oceanic lithosphere is complicated and the analysis of geoid anomalies may provide answers to the many questions that remain.

#### 5.4 References

- Fisher, R. L., and J.G. Sclater, 1983, Tectonic evolution of the Southwest Indian Ocean since the Mid-Cretaceous: Plate motions and stability of the pole of Antarctica/ Africa for at least 80 Myr, *Geophys. J. R. astr. Soc.*, 73, 553-576.
- Robinson, E. M., B. Parsons and M. L. Driscoll, The effect of a shallow low viscosity zone on the mantle flow and geoid anomalies at fracture zones, submitted to *Geophys. J. R. astr. Soc.*, 1987.
- Royer, J-Y, P. Patriat, H. W. Bergh, C. Scotese, Evolution of the Southwest Indian Ridge from the Late Cretaceous (anomaly 34) to the Middle Eocene (anomaly 20), submitted to *Tectonophysics*, 1987.
- Shaw, P. R., 1987, Investigations of relative plate motions in the South Atlantic using Seasat altimeter data, *J. Geophys. Res.*, in press.

## Acknowledgements

Many thanks to all the students and staff in the Earth, Atmospheric and Planetary Sciences Department at M.I.T. --the Green Building will always bring back good memories of my years here. This thesis could not have been done without the guidance and support of my advisor, Barry Parsons, who suggested research topics and gave me the opportunity to work with the Seasat data (a geophysical treasure chest). Barry, Robert Fisher, Marcia McNutt and Sean Solomon all reviewed my papers over the years and gave invaluable comments and advice. Linda Meinke and Steve Daly solved many of my computer problems --thank you both for your patience and for sharing your expertise. Tina Freudenberger and Paul Scharr typed large parts of this thesis, usually when time was tightest. My officemates Maggie Goud, Cindy Ebinger, Adam Freedman, Bernard Celierer and Paul Filmer were always my first, and usually the best source for help with scientific or computing problems, or for advice on how to get through the tougher days. Cindy Ebinger helped me put this thesis together and accompanied me on numerous and essential coffee breaks. Speaking of coffee, many thanks to Paul Okubo for the LSR (Long Scenic Route) trips to the coffee shop. And a special thanks to Peter Wilcock and his family for sharing their lives with my husband and myself.

I cannot thank my parents enough for giving me the desire to pursue an education, for their encouragement, and for the plane tickets home to California. I needed them all. The best parts of these years have been with my husband Paul Scharr, and son Matthew who shared many late nights with me to finish this thesis, and who shared many more nights with each other so I could work. I couldn't have done it without their love.

## Biography

The author was born in Petaluma, California in 1959 to Setsuko and Merrill Driscoll. After graduating at the top of her highschool class she attended the University of California at Berkeley. At Berkeley, Walter Alvarez's enthusiasm for the Earth inspired her to pursue graduate work in marine geophysics at the Massachusetts Institute of Technology and Woods Hole Oceanographic Institution. On May 14, 1987 she successfully defended her doctoral thesis, culminating six years of graduate work.

## Publications:

Driscoll, M. L., B. E. Tucholke and I. N. McCave, 1985, Seafloor zonation in sediment texture on the Nova Scotian lower continental rise, *Marine Geology*, 66, 25-41.

Driscoll, M. L., R. L. Fisher and B. Parsons, 1987, Fracture zone trends and structure at the Southwest Indian Ridge: An investigation using Seasat altimetry and surface-ship bathymetry, *Geophys. J. R. astr. Soc.*, (submitted).

Driscoll, M. L. and B. Parsons, 1987, Cooling of the Oceanic lithosphere -- Evidence from geoid anomalies across the Udintsev and Eltanin Fracture Zones, *Earth. Planet. Sci. Lett.*, (submitted).

Robinson, E. M., B. Parsons and M. Driscoll, 1987, Effects of a low viscosity zone in the mantle and geoid anomalies at fracture zones, *Geophys. J. R. astr. Soc.*, (submitted).

## DOCUMENT LIBRARY

August 21, 1987

### *Distribution List for Technical Report Exchange*

Attn: Stella Sanchez-Wade  
Documents Section  
Scripps Institution of Oceanography  
Library, Mail Code C-075C  
La Jolla, CA 92093

Hancock Library of Biology &  
Oceanography  
Alan Hancock Laboratory  
University of Southern California  
University Park  
Los Angeles, CA 90089-0371

Gifts & Exchanges  
Library  
Bedford Institute of Oceanography  
P.O. Box 1006  
Dartmouth, NS, B2Y 4A2, CANADA

Office of the International  
Ice Patrol  
c/o Coast Guard R & D Center  
Avery Point  
Groton, CT 06340

Library  
Physical Oceanographic Laboratory  
Nova University  
8000 N. Ocean Drive  
Dania, FL 33304

NOAA/EDIS Miami Library Center  
4301 Rickenbacker Causeway  
Miami, FL 33149

Library  
Skidaway Institute of Oceanography  
P.O. Box 13687  
Savannah, GA 31416

Institute of Geophysics  
University of Hawaii  
Library Room 252  
2525 Correa Road  
Honolulu, HI 96822

Library  
Chesapeake Bay Institute  
4800 Atwell Road  
Shady Side, MD 20876

MIT Libraries  
Serial Journal Room 14E-210  
Cambridge, MA 02139

Director, Ralph M. Parsons Laboratory  
Room 48-311  
MIT  
Cambridge, MA 02139

Marine Resources Information Center  
Building E38-320  
MIT  
Cambridge, MA 02139

Library  
Lamont-Doherty Geological  
Observatory  
Colombia University  
Palisades, NY 10964

Library  
Serials Department  
Oregon State University  
Corvallis, OR 97331

Pell Marine Science Library  
University of Rhode Island  
Narragansett Bay Campus  
Narragansett, RI 02882

Working Collection  
Texas A&M University  
Dept. of Oceanography  
College Station, TX 77843

Library  
Virginia Institute of Marine Science  
Gloucester Point, VA 23062

Fisheries-Oceanography Library  
151 Oceanography Teaching Bldg.  
University of Washington  
Seattle, WA 98195

Library  
R.S.M.A.S.  
University of Miami  
4600 Rickenbacker Causeway  
Miami, FL 33149

Maury Oceanographic Library  
Naval Oceanographic Office  
Bay St. Louis  
NSTL, MS 39522-5001



<b>REPORT DOCUMENTATION PAGE</b>		1. REPORT NO. <b>WHOI-87-23</b>	2.	3. Recipient's Accession No.
4. Title and Subtitle <b>Application of Seasat Altimetry to Tectonic Studies of Fracture Zones in the Southern Oceans</b>		5. Report Date <b>June 1987</b>		
7. Author(s) <b>Mavis Lynn Driscoll</b>		6.		
9. Performing Organization Name and Address <b>Woods Hole Oceanographic Institution Woods Hole, Massachusetts 02543 and The Massachusetts Institute of Technology Cambridge, Massachusetts</b>		8. Performing Organization Rept. No. <b>WHOI-87-23</b>		
12. Sponsoring Organization Name and Address <b>Office of Naval Research and National Science Foundation</b>		10. Project/Task/Work Unit No.		
15. Supplementary Notes		11. Contract(C) or Grant(G) No. (C)N00014-80-C-0273 (G)N00014-86-K-0325 DPP-8405968		
This thesis should be cited as: Mavis Lynn Driscoll, 1987. Application of Seasat Altimetry to Tectonic Studies of Fracture Zones in the Southern Oceans. Ph.D. Thesis. MIT/WHOI, WHOI-87-23.		13. Type of Report & Period Covered <b>Ph.D. Thesis</b>		
16. Abstract (Limit: 200 words) <p>Gravity derived from Seasat altimetry has provided a means of estimating seafloor topography and its compensation, which in turn can be used to understand the evolution of oceanic lithosphere. In the first study of this thesis, the correlation between the geoid, and seafloor topography is investigated along a section of the Southwest Indian Ridge. Geoid anomalies computed from a simple thermal model fairly accurately predict the intermediate-wavelength anomalies across the fracture zones. The shorter wavelength anomalies are consistent with those calculated from topography using elastic plate compensation. In the second study, fracture zones along the Southwest Indian Ridge are identified using altimeter profiles and bathymetry. Finite poles of rotation are determined from both the fracture zone locations and magnetic anomaly lineations for anomalies 6, 13, and 20. A present-day pole of rotation calculated from transform fault azimuths determined primarily from their geoid anomalies, agrees with published poles based on bathymetric data. In the third study, the rate of change of the geoid with age has been estimated as a function of age from geoid offsets across the Eltanin and Udintsev fracture zones and used to constrain thermal models of lithospheric cooling. Although the thermal plate cooling model is successful in predicting both seafloor depths and heat flow values out to ages of at least 80 m.y. B.P., it cannot explain the observed geoid slope values for these two fracture zones.</p>		14.		
17. Document Analysis a. Descriptors				
1. gravity				
2. tectonics				
3. Fracture Zones				
b. Identifiers/Open-Ended Terms				
c. COSATI Field/Group				
18. Availability Statement: <b>Approved for publication; distribution unlimited.</b>		19. Security Class (This Report) <b>UNCLASSIFIED</b>		21. No. of Pages <b>165</b>
		20. Security Class (This Page)		22. Price